THE UNIVERSITY OF CHICAGO

CIRCUIT QUANTUM ELECTRODYNAMICS WITH ELECTRONS ON CONDENSED NOBLE GAS SUBSTRATES

A DISSERTATION SUBMITTED TO
THE FACULTY OF THE DIVISION OF THE PHYSICAL SCIENCES
IN CANDIDACY FOR THE DEGREE OF
DOCTOR OF PHILOSOPHY

DEPARTMENT OF PHYSICS

BY
BRENNAN DIZDAR

CHICAGO, ILLINOIS
DECEMBER 2026

© 2026 by Brennan Dizdar

ORCID iD: https://orcid.org/0000-0001-8425-9914

ABSTRACT

Electrons levitating on condensed noble gas substrates form the basis for a promising platform for quantum information science. The electrons can be trapped electrostatically in a pristine dielectric environment, far from the impurities and defects of the underlying device substrate. The orbital motion, vertical Rydberg states, and spin states of these electrons have all been postulated as strong candidates for qubits. Circuit quantum electrodynamics presents a versatile toolbox for interacting with these electrons.

In this thesis, we study isolated levitated electrons coupled to a nearby superconducting resonator with microwave-range spectroscopy, focusing on superfluid helium substrates with an accompanying chapter featuring solid neon. The interaction of the transition dipole moment of the electron orbital states and the microwave electric field from the resonator produces an electron-state-dependent frequency shift of the resonator. We use microwave spectroscopy to study how electron clusters respond to local electrostatic fields, finding distinct profiles of the cluster translational motion states in the space spanned by orthogonal electric field lever arms, reflecting a configuration-dependent electron linewidth and interaction energy. We then indirectly interrogate the orbital ladder of states of a single trapped electron by studying the AC Stark shift of the coupled resonator, which inherits some characteristics of the electron's nonlinearity, inferring significant tunability of the ladder nonlinearity. Models of the system dynamics and electron response to applied electric fields agree well with the experimental results. We also study the coherence and noise properties of electrons trapped on solid neon surfaces, which are exceptional charge qubits, and utilize a high-temperature superconductor microwave resonator to study the growth of solid neon near the triple point in real time. We conclude with a discussion of future directions for the platform, including spin-orbit interaction schemes and the use of thinner helium films.

To my parents, Kadina and Ivan

"I have only 3 left, but you can have one! Choose!"

— Professor Oak, Pokémon Red & Blue,

and my advisor when I was selecting a project at the beginning of my PhD journey

TABLE OF CONTENTS

LIST OF FIGURES viii

LIST OF TABLES x

ACKNOWLEDGMENTS xi

1 INTRODUCTION 1
1.1 Levitating Electrons 2
1.2 From Condensed Matter Physics to Quantum Science 3
1.3 Floating Electrons Today 6

2 CIRCUIT QED WITH ELECTRONS ON HELIUM 7
2.1 Desirable Qubits for Quantum Information Science 7
2.2 The Quantum Harmonic Oscillator in Circuits 10
2.3 The Jaynes–Cummings Hamiltonian 13
2.4 Integrating an Electron Oscillator into Circuit QED 18

3 ORBITAL STATES OF AN ELECTRON ON HELIUM 21
3.1 Modeling the Electron as an Anharmonic Oscillator 21
3.2 Dephasing due to Ripplons 27
3.3 Decay due to Phonons 33
3.4 Johnson Noise 36
3.5 Charge Noise 37
3.6 Radiation and Purcell Loss 38
3.7 Summary of Design Goals 39

4 EXPERIMENT DESIGN 40
4.1 Cryostat and Liquid Helium Filling Setup 40
4.2 RF Spectroscopy and DC Bias Setup 43
4.3 Devices for Trapping Single Electrons 49
4.4 Finite Element Modeling and Device Design Philosophy 57

5 SINGLE-ELECTRON ISOLATION 60
5.1 Electron Counting 60
5.2 Spectral Signatures of Electron Clusters 64
5.3 Properties of Single Electrons 65
5.4 Trapping Potential Asymmetry and Stability 67

6 THE ELECTRON ORBITAL STATE LADDER 71
6.1 Studying Electron Ladder Nonlinearity with a Resonator 71
6.2 Nonlinearity of a Single Electron 73
6.3 Implications for Future Studies 77

7 ELECTRONS ON NEON 80
7.1 Neon Growth 81
7.2 Dielectric Loss Experiments with Tunable Dielectric Thickness 86
7.3 Towards Electron Ensemble Detection on Neon 90
7.4 Electron-on-Neon Charge Qubits 90
7.5 Qubit Models 96

8 FUTURE DIRECTIONS AND CONCLUSION 98
8.1 Spin-Orbit Interaction 98
8.2 Quantum Computing with Multiple Electrons 100
8.3 Electron Manipulation on van der Waals Helium Thin Films 102
8.4 Conclusion 105

APPENDIX A MODEL FOR COUNTING ELECTRONS 106

APPENDIX B DEVICE GALLERY 107
B.1 Devices 108
B.2 On-Chip Filters 112

APPENDIX C DEVICE FABRICATION RECIPES 114
C.1 Full Device Recipe 114
C.2 Additional Recipes 117

APPENDIX D EQUIPMENT CATALOGUE 118

REFERENCES 120

LIST OF FIGURES

1.1 States of a levitating electron 4

2.1 Jaynes–Cummings Hamiltonian ladder of states 15
2.2 Coupling to an electron on helium with a microwave resonator 20

3.1 Simulation of orbital state properties 23
3.2 Contribution of helium surface curvature to the electron trap 24
3.3 The electron wavefunction on a curved ripplon surface 28
3.4 Anderson–Kubo criterion for electrons on helium 32
3.5 Phonon-induced orbital state decay 34
3.6 Simulated single-phonon limited decay lifetime of orbital states 36

4.1 Helium filling apparatus 43
4.2 Spectroscopy and bias equipment 45
4.3 Single-tone spectroscopy of a readout resonator 46
4.4 DC filtering approach 49
4.5 Optimal resonator for coupling to an electron 51
4.6 Helium capillary action in microchannels 52
4.7 Electron ensemble response: resonator 53
4.8 Electron ensemble response: Sommer–Tanner 54
4.9 Channel depth and inter-electron interactions 55
4.10 Typical electron trap design 58

5.1 Electron unloading 60
5.2 Simulation of multi-electron motion 61
5.3 Single-electron counting 62
5.4 Native TLS signal in two dimensions 63
5.5 Two-dimensional profiles of multiple electrons in experiment 64
5.6 Single-electron anticrossing 67
5.7 Simulated effects of trap asymmetry 68
5.8 Electron in an asymmetric trap 69
5.9 Stability in time of the electron trap curvature 70

6.1 Experiment schematic for measuring a resonator with Kerr 73
6.2 Nonlinear-resonator Kerr raw traces 74
6.3 Comparison of model to data in Kerr experiments 76
6.4 Experimental evidence of anharmonicity tunability of orbital states 77
6.5 Simulated electron lifetime dependence on trap structure 79

7.1 Experiment setup for monitoring neon growth 83
7.2 Sensitivity of the device to neon growth 84
7.3 Liquid neon deposition and dynamics 85
7.4 Solid neon growth through a quasi-static phase transition 86

7.5 Dielectric loss model from participation ratios 88
7.6 Electron-on-neon charge qubits 92
7.7 Lifetime and coherence of an electron-on-neon charge qubit 93
7.8 Characterization of qubit noise with dynamic decoupling 95
7.9 Bump-model for a trapped electron 96

8.1 Spin-orbit coupling schematic 99
8.2 Mølmer–Sørensen gate scheme for electrons on helium 101
8.3 Electron control on helium thin films 103
8.4 Narrower-linewidth charge states of electrons on helium 104

A.1 Simulation of electron unloading 106

B.1 Early devices: sacrificing trap-flattening for field and ripplon insensitivity 108
B.2 Change in direction: inspiration by previous works with some compromise . . . 109
B.3 More successful: maximize the knobs 110
B.4 Collaborator (EeroQ Quantum Hardware) device 111
B.5 Sensitivity Improvements 111
B.6 Filter 1: low-pass with inductive spiral and finger capacitors using Nb/Al 112
B.7 Filter 2: stepped-impedance waveguide filter using TiN 112
B.8 Filter 3: lumped low-pass using TiN 113
B.9 Filter 4: compact lumped low-pass using TiN 113

LIST OF TABLES

D.1 Equipment catalogue 118

ACKNOWLEDGMENTS

My time with physics so far has been a story of people who have gone out of their way and above and beyond time and again to support me and help me grow even though they had no particular reason to do so. Here, I would like to celebrate these amazing people and what they have done for me and many others.

A PhD begins with a mentor and I have been lucky enough to work with both an incredible advisor in Dave Schuster and another mentor I did not expect to have but who made all the difference in the end. I knew I wanted to work with Dave from the moment I first visited his lab and met his students. Dave's enthusiasm for physics is infectious and his broad optimism and confidence in his students make it feel like anything that is not obviously impossible is absolutely within reach for us. Every graduate student can only hope they have an advisor who is willing to make anything possible for them, which for me included staying at the University of Chicago rather than moving to California. He has a gift for bringing together great people who want to study science in the best, most collaborative ways possible. Without his support, first at the University of Chicago and later from Stanford, I would not have grown so much as a physicist.

Just as important as Dave was my postdoc, Chris Lang. I could tell Chris would be amazing to work with the moment I met him and I was and still am convinced that this project would not have been possible without him. The physics world is saturated with odd ducks; we quack and waddle together and make ripples in whatever ponds we can find. Chris is one of those special scientists who have ascended to being an odd goose: sophisticated, highly personable, and strikingly tall, both literally and figuratively. Being a physicist and being a scientist are different skills and if Dave taught me how to be a physicist, then Chris taught me to be a scientist. Chris has been like a second advisor to me, a tall ask for a fresh postdoc, and for that I will be forever grateful.

While Dave and Chris have been the most instrumental to my development, I have been

fortunate enough to have enjoyed the support of many other scientists as well. Gerwin Koolstra, my project predecessor in the lab, supported my early efforts despite having already graduated, and conversations with him throughout my PhD gave me confidence and invaluable guidance. He is, in my opinion, the original electrons-on-helium master and I once spoke of him with such reverence that my poor wife associated him with past physicists like Feynman and Fermi and was shocked to learn some years ago that he is still alive. Continuing research in Chicago after my lab moved to Stanford would not have been possible without the help of the people I met at Argonne National Laboratory. Dafei Jin, Xu Han, Xinhao Li, Yizhong Huang, Xianjing Zhao, and Dan Rosenmann among others jumped through hoops time and again to make sure we felt welcome and productive. I also have to thank the people I met at EeroQ Quantum Hardware, particularly Elena Glen, Niyaz Beysengulov, David Rees, Heejun Byeon, and Johannes Pollanen, for making some of the central results of this dissertation possible. It is challenging to work in a niche subdiscipline of a booming research field and I learned much by collaborating with them. Finally, I have to thank the first physicists who took me under their wings: Eric Majzoub at UMSL, Philip Kim at Harvard, and then-postdocs Yuval Ronen and Önder Gül. I actually had to search far and wide for research labs willing to include me during college and without the efforts and willingness of these four it is unlikely that I would have gone to graduate school for physics.

Braving graduate school is a tough task made doable by great friends and peers doing the same. I was surrounded by kind, competent, and incredible people both within and outside of the lab. First, I'd like to thank the members of Schuster Lab who kept it a consistently wonderful research environment. It has been my privilege to work with Yueheng Shi at Stanford these past few years. Without his talent, dedication, and selflessness, our projects likely would not have survived the transition to Stanford, much less have been productive, and I look forward to seeing where he takes them. Kan-Heng Lee, Andrew Oriani, Sasha Anferov, and Andrei Vrajitoarea freely served as in-lab mentors for me even though our

projects had little in common and I would have been utterly lost without their support. Gabrielle Roberts, Meg Panetta, and Kevin He kept the lab alive even during the pandemic and were pillars of our lab culture at the University of Chicago. Helin Zhang kept the office lively even in the twilight and ensured that there would always be someone else in the office. Fang Zhu, Brendan Saxberg, Tanay Roy, Ankur Agrawal, Riju Bannerjee, Vatsan Chakram, and Akash Dixit were wonderful to work with and without caveat offered their assistance whenever I needed it. Morgan Lynn and Ziqian Li jumped into the lab simultaneously with me while Chunyang Ding and Connie Miao joined soon after and watching their impressive progress in the face of their own adversities fueled my personal drive. Finally, I have to thank the labmates I met at Stanford. While we were thousands of miles apart most of the time, because of them I always felt like a part of the lab goings-on; thank you Shannon, Wendy, Eesh, Matt, Kaushal, Paul, Kaveh, Victor, Jiayi, Nikitha, Seb, Sunada, Chuyao, Guan, Mihir, and Hwanchul.

Outside of the lab, I had the support of a wonderful cohort. It made enduring the pandemic more fun than it should have been and those late nights on the third floor of KPTC before the lockdown were some of the most entertaining of my life. I need to especially acknowledge a handful of individuals who became a part of my day-to-day routine for the entirety of graduate school: Cheyne Weis, Alec Hryciuk, Sergei Shmakov, Desiree Schippers, and Morgan Lynn. You are incredible friends and it is because of you that I can look back on the first few years of graduate school with an unyielding smile. We may not be able to play board games on Drexel anymore, but I will hold on to the collection for whenever we get the chance again. And, of course, I have to thank our physics intramural soccer team: the Quantum Ball Effect. I looked forward to every one of our games like it was a holiday; I missed a game to attend my own wedding and I am both proud and ashamed to admit that for a brief moment I felt a pang of disappointment. I shudder to think of what my physical condition would have been like at the end of graduate school without you. I would also

like to acknowledge the administrators I have interacted with regularly: Brenda Thomas, Putri Kusumo, and Michelle Dessinger at the University of Chicago and Nyein Su Mon at Stanford. Thank you for maintaining order among all the odd bureaucratic tasks we present you with against our best, though unintentional, efforts to sow chaos.

Finally, I have to thank my family for their immense support over these seven years. A PhD is challenging for the scholar and for their loved ones. The work can be intense with an odd rhythm over the year and anxieties about the repair status of cleanroom lithography tools can be difficult to convey to most people. I am fortunate to have collected individuals in my life who tolerate my idiosyncrasies and occasional disappearance from reality while offering me love in return. When my parents, Kadina and Ivan, arrived in the United States, I am sure that being a physicist was not on their radar for their son's future. They encouraged me to always walk on my own two feet while staying close behind to catch me whenever I fell. Their intelligence, compassion, and appreciation for the world have always been everything I strive for, and I would walk to the ends of the Earth if they believed I could. My brother Benjamin has been my closest friend and confidant throughout graduate school. He helped me face every new challenge with courage, and despite his being six years younger, I look up to him and how he navigates this confusing world maybe more so than anyone else. I also have to thank the special animal friends in my life: canine Marley and felines Richard Parker and Bagheera. We like to say that our cats have PhDs in kitty-nomics from Purdue and Richard Parker in particular heard more about my graduate school research than perhaps even my advisor and closest collaborators. Those little eyes and ears listen to us ruminate on the mysteries of the universe and the challenges of our lives more attentively than we deserve. Finally, I am deeply grateful to my wife Acadia, who was there for every moment of this journey. She has been the best part of many days and has supported me traveling thousands of miles around the world, spending thousands of hours in the cleanroom, and staying up late countless nights all in the name of my electrons on helium. I can only hope

that I can one day be as happy and as good a physicist as she is a teacher. She is the image charge that binds me to the helium.

CHAPTER 1

INTRODUCTION

Modern quantum information science is largely the child of the marriage between experimental condensed matter physics and the theory of quantum optics. As is typical of many offspring, the degree of resemblance to either parent varies between more advanced platforms, such as superconducting circuits, trapped ions, or quantum dots, and still early-life platforms like micromechanical oscillators. In most cases, there is an ironic growth pattern: leveraging the condensed matter aspect to create a platform and then improving it by stripping away unnecessary condensed matter dependencies and interactions. Rare is a system born wholly out of confidence in the underlying condensed matter. An electron levitating on superfluid helium exists in perhaps the most pristine electromagnetic environment imaginable short of true vacuum [1, 2]. Interactions with the helium are simpler to model than interactions with solid substrates and a single electron in a potential well is an archetypal toy model of physics. While electrons on helium or other condensed noble gases hold great promise as a quantum information platform, they face unique challenges posed by these novel substrates. This dissertation provides scientific and historical context for electrons on helium as a quantum information science platform and describes experiments studying their orbital motion states before discussing future trajectories for the field. The first three chapters contextualize the system in quantum information science more broadly and outline embedding these electron oscillators in the framework of circuit quantum electrodynamics. The following three chapters describe experiments studying the quantized ladder of states of the electron orbital motion. Finally, the dissertation closes with a discussion of a similar platform, electrons on solid neon, and future experimental goals for levitating electrons. By the end, an interested reader should have an appreciation for the strengths of the system at present and its longer-term objectives and associated challenges.

1.1 Levitating Electrons

Naturally, we begin with a discussion of why these electrons levitate. An electron near a dielectric interface experiences two forces orthogonal to the boundary: interaction with its virtual image charge on the opposite side of the boundary and the insertion cost associated with the electron entering the opposite dielectric. An image charge of opposite sign, scaled by $(\epsilon - 1)/(\epsilon + 1)$, accounts for the polarization charge at the boundary and keeps the electric potential continuous across it. The electron is attracted to the boundary if the opposite dielectric constant is greater. For condensed matter systems, each side of the boundary also has an electronic chemical potential to consider, implying that the system energy is minimized with the free electron on a particular side of the boundary. For a system with an electron insertion penalty but attraction to the boundary, the electron is bound to the surface with hydrogen-like energy levels, each associated with a mean distance from the boundary [3, 4]. If the electron is in vacuum, the first requirement is automatically satisfied and many dielectrics satisfy the second in order to make a levitating electron possible. For an electron above a dielectric with permittivity ϵ (1.057 for liquid helium), the image potential and the resulting energy levels are

$$V(z) = -\frac{\Lambda e^2}{4\pi\epsilon_0 z}, \qquad \Lambda = \frac{\epsilon - 1}{4(\epsilon + 1)}, \qquad E_n = -\frac{R}{n^2}, \qquad R = \frac{m_e \Lambda^2 e^4}{2\hbar^2 (4\pi\epsilon_0)^2}$$

with a mean height $\langle z \rangle \approx 11$ nm in the ground state. However, superfluid helium is a particularly appealing choice.

The purity of liquid helium-4, which also has one of the lowest known static permittivity constants, arguably makes it the most natural choice of dielectric for a levitating electron system [5]. A floating electron is well separated from both the helium surface and any underlying substrates independently of the helium depth [6]. An electron also floats on solid hydrogen and some noble gases like neon, but its distance to the surface is nearly an

order of magnitude smaller in all cases, and is even smaller for higher-dielectric-constant solids with a negative electron affinity [7–10]. Furthermore, the liquid helium surface is self-healing and atomically smooth, which is not true of most solids. The liquid is charge- and spin-neutral and the bulk nuclear-spin impurity density for commercial isotopically purified helium-4 is several orders of magnitude lower than in many highly purified solids. Because the helium binds the electron in its Rydberg ground state to a particular height orthogonal to the surface, the electron can be bound laterally with only electrostatic forces, unlike charged particles in vacuum [11]. This makes it possible to separate spatial control of the electron with electrostatics from manipulation of the electron's quantum states with pulsed spectroscopy.

1.2 From Condensed Matter Physics to Quantum Science

The intrinsic cleanliness of the system is what first propelled research in electrons on helium as a platform for studying classical many-body physics. Electron ensembles on bulk helium were studied alongside electron baths in semiconductors throughout the 1970s as classical, two-dimensional electron gases [12]. Unlike in semiconductors, the effective electron mass is simply the bare mass and the inter-electron interactions on helium are long-range and unscreened. An ensemble on helium is largely disorder-free and its scattering by helium vapor at temperatures above several hundred millikelvin or by helium excitations at lower temperatures is straightforward to model relative to disorder in semiconductors [13, 14]. The platform was, therefore, ideal for studying highly correlated electron gases, and Wigner crystallization of an electron ensemble at low temperatures was first observed in levitating electrons [15, 16]. Here, the study of electron gases in semiconductors and on helium diverged. Semiconductors could reach the quantum, degenerate regime owing to significantly higher electron densities and lower effective electron mass and could leverage rapid industrial development [12, 17]. Hydrodynamic instability limits the electron density on bulk helium

to $\approx 10^9$ cm^{-2} [18]. The density can be made one to two orders of magnitude higher on van der Waals thin films of helium, but the electron mobility generally suffers due to pinning by roughness of underlying solid substrates [19]. While semiconductor physics began exploring quantum-mechanical effects, research in electron ensembles on helium focused on electron transport and the study of superfluid helium properties [2].

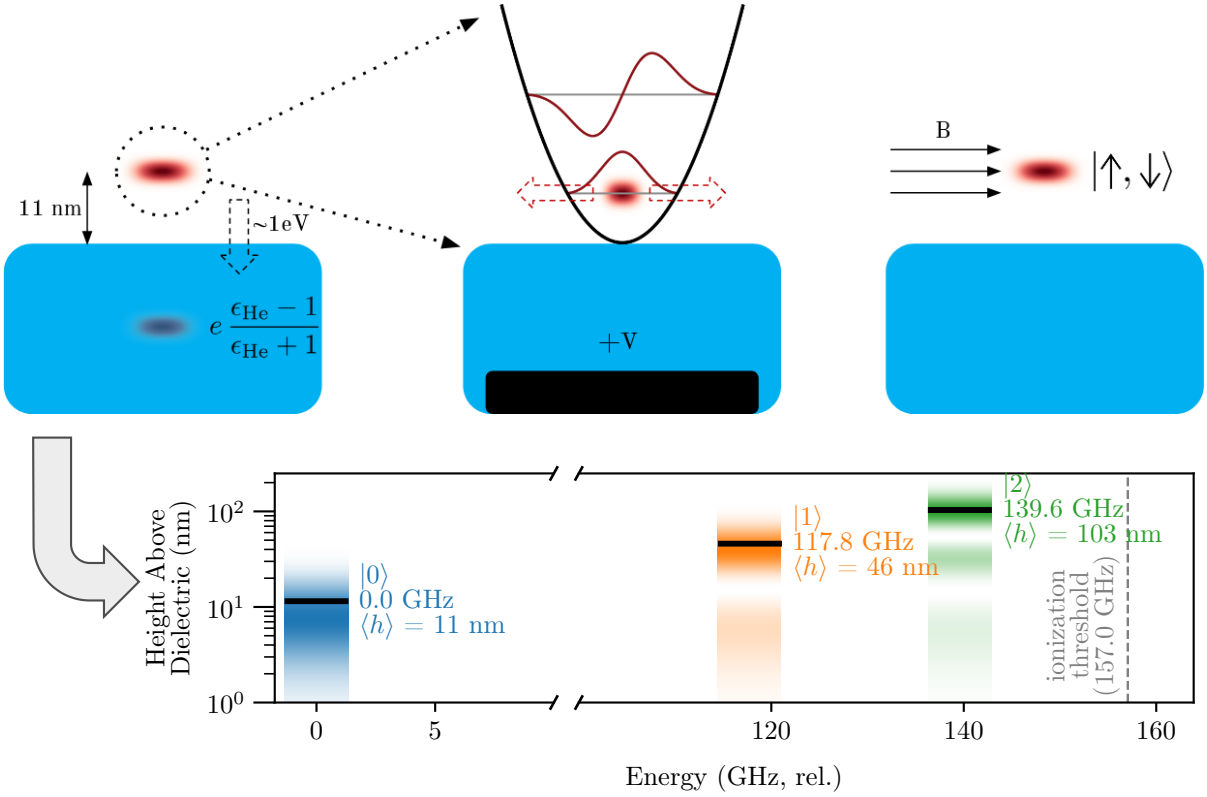


Figure 1.1: States of a levitating electron
The vertical distance of the electron from the helium surface is quantized in 'Rydberg' states. If the electron is then confined laterally in an electrostatic trap, the lateral motion of the electron is also quantized in 'orbital' states. The addition of an external magnetic field establishes a quantization axis for the electron spin.

In the past few decades, several properties of an electron on helium have been proposed as foundations for a condensed matter qubit [1, 20–22]. In the same year that coherent control of a Cooper-pair box was famously achieved, the vertical Rydberg states of an electron on helium were proposed as a qubit [1, 23]. Individual electrons were counted and isolated

with the aid of single-electron transistors [24, 25]. Proposals for electron orbital motion qubits and electron spin qubits also emerged, marking the system as a versatile platform for quantum information science [21, 22, 26]. Relative to other platforms like semiconductors and superconducting qubits, which achieved single-shot readout of the qubit state relatively quickly after beginning development, even coherent control of a floating electron on neon and strong coupling to a superconducting resonator in the helium case were not demonstrated until recently [27, 28]. There is no ohmic contact to the floating electron, and it must reside relatively far from device conductors to maintain high mobility and independence from device surface imperfections. Because interacting with the electron is ironically challenging and the helium itself introduces unique decoherence channels, the platform has had to gradually borrow techniques from other systems to overcome these challenges. However, quantum information science with levitating electrons is finally possible!

1.3 Floating Electrons Today

The past decade has seen exciting developments for electrons on helium and similar platforms. Coherent control of the orbital states of an electron on helium is now in reach after the integration of the system with circuit quantum electrodynamics [28, 29]. The experiments in this dissertation focus on this approach. Similarly, research in the Rydberg states continues with progress towards manipulating individual electrons [30]. The field has also expanded to electrons on solid neon; the solid-state dielectric negates many of the challenges introduced by the liquid helium surface, and trapped electrons on neon have been shown to be exceptional charge qubits [27, 31, 32]. All of these systems are poised to explore the electron spin state soon as well [33–35]. Electrons in Penning traps, which once developed alongside trapped ions, are regaining research interest because many of the challenges they once faced have been solved [36–38]. Control of electrons on helium with surface acoustic waves and exploration of many-electron plasmon modes have seen exciting developments, and shuttling of single electrons on helium thin films can now be facilitated by atomically smooth, amorphous metal electrodes [39–41]. Although optimistic, it is not unreasonable to hope that electrons on helium will soon enjoy the rapid growth as a quantum information platform that other platforms experienced shortly after first manipulating qubits, especially with the aid of these recent experimental developments.

CHAPTER 2

CIRCUIT QED WITH ELECTRONS ON HELIUM

Over the past several years, development in quantum information platforms has exploded. The field of superconducting circuits in particular has made astonishing progress in developing the building blocks for a quantum computer [42, 43]. Anecdotally, several years ago, the community was abuzz with excitement at the introduction of tantalum as an alternative base metal layer for transmon qubits because it resulted in consistently state-of-the-art lifetimes in the hundreds of microseconds [44, 45]. Quantum computers still seemed a distant future. Today, state-of-the-art superconducting qubits have lifetimes of milliseconds, the surface-code error correction threshold has been passed, and the United States government has taken direct equity stakes in companies focused on quantum information technologies [46–48]. In this chapter, we discuss fundamentals of controlling addressable quantum states from the perspective of circuit quantum electrodynamics (cQED) [49, 50]. We begin by describing some strong points that cQED would like to leverage towards designing and manipulating qubits. Starting from the quantum harmonic oscillator, we add nonlinearity to arrive at the familiar Jaynes–Cummings Hamiltonian and its limits. We close by describing the strategy for integrating an electron on helium into the platform and why one might be interested in quantum information science with a still-developing platform when other systems are already progressing nicely.

2.1 Desirable Qubits for Quantum Information Science

Putting aside the more general interesting science made possible by observation and control of quantum phenomena, it is worth considering the requirements for perhaps the most challenging end of quantum information science: building a quantum computer. The DiVincenzo criteria, a common starting point for the discussion, articulate some broad prerequisites [51]:

- A scalable physical system with well-characterized qubits
- The ability to initialize to a simple fiducial state
- Long coherence times relative to gate times
- A universal set of gates
- Qubit-specific measurement

Over time, the interpretation of the criteria in the field of quantum information science has changed, largely owing to the fact that while the error rate of classical transistors is practically negligible, gate errors in state-of-the-art devices reach only 10^{-3} per cycle, requiring framing of the criteria within the context of error correction [52]. For example, 'well-characterized qubits' may now imply noise characterization through randomized benchmarking and gate set tomography since most error correction schemes assume errors are local and weakly correlated between qubits [53–55]. 'Long coherence' now means long compared with a full error-correction cycle, including the repeated initialization of ancilla qubits for error detection [56]. This dissertation focuses on a still early-life platform for quantum information science, however, so we will frame this discussion around a laxer interpretation of the criteria at the single-qubit level and eventually how electrons on helium would satisfy more complex requirements in the future.

While there are many approaches to building a quantum computer, we can loosely strategize broadly satisfying the DiVincenzo criteria, albeit in a biased way, to see how one arrives at cavity and circuit quantum electrodynamics as promising platforms [50]. A defining characteristic of both is the physical separation of the readout architecture, the 'cavity,' from the qubits. In vacuum, information leaked from a qubit is lost to the environment. By placing the qubit in a cavity, a structured, low-loss microwave environment, the information can be preserved for much longer while still permitting interrogation of the qubit [57–59]. In a sense, this converts an irreversible process into a partially reversible one [60]. In the case

of superconducting circuits, the cavity is made planar and relatively small (millimeters or less) in the form of a superconducting microwave resonator. Not only is this amenable to scalability, but the interaction energy between the qubit and the cavity can be engineered to be high, making for gate speeds on the order of 10 ns. The coupling strength and exceptional cavity coherence also make it possible to address individual qubits when the cavity is detuned from the qubit spectral lines. Since interactions can be engineered through device geometry modifications, there is great flexibility when designing gates and measurement protocols. When focusing on more advanced criteria for building a quantum computer from the perspective of error correction, there is of course more nuance, but these strengths have allowed the field to create systems with hundreds of physical qubits today [48].

Hybrid quantum systems integrating circuit quantum electrodynamics with other systems have the potential to be even more successful [61, 62]. A quantum computer need not be constructed from only a single platform of many, especially when their strengths are often complementary. The Josephson junction is the archetypal nonlinear circuit element which forms the basis for the usual qubit of choice for cQED: the transmon. While transmon lifetimes can now be quoted in milliseconds [46, 47], the coherence might ultimately be limited by dissipation from the normal fluid fraction in the superconducting material of choice. Single spins and trapped ions can already exhibit significantly longer coherence times [63, 64]. Furthermore, while modern nanofabrication allows for an armory of on-device architectures, it is not so versatile as to allow for mobile transmons; qubit-to-qubit coupling is largely fixed during device fabrication. While these weaknesses have by no means proven insurmountable, there is room for our condensed matter system of choice, electrons levitated on superfluid helium, to fill the gaps.

Electrons on helium integrate remarkably well with superconducting circuits. The electron exists in perhaps the most pristine dielectric environment short of true vacuum. This largely frees an electron-on-helium qubit from decoherence mechanisms sourced through ma-

terial properties and defects. The electron spin lifetime is postulated to be extraordinarily long in levitated electron platforms [21, 33, 34]. Furthermore, single electrons are identical to one another, can be transported across a device, and can be generated on demand in arbitrary quantities [41]. Of course, manipulating an electron on helium presents its own significant challenges; while popularity is always a factor, it is not by chance that cQED developed at the pace it did while strong coupling between a microwave photon in a superconducting resonator and an electron on helium was only recently achieved [28, 29]. Regardless, it is exciting how complementary the platforms are with one another.

2.2 The Quantum Harmonic Oscillator in Circuits

When focusing on quantum mechanics formulated in position and momentum space, perhaps the most intuitive system to consider is the quantum harmonic oscillator. Only depending on two canonically conjugate variables added in quadrature, this model is a useful approximation for a particle trapped in a potential well. It is a natural starting point for describing systems such as trapped floating electrons, quantized electrical circuits, electromagnetic fields, and more.

$$H = \frac{\hat{p}^2}{2m} + \frac{1}{2}m\omega^2\hat{x}^2 \tag{2.1}$$

Drawing inspiration from the classical model of a mass on a spring, we can promote the classical variables to operators. Using the commutation relation $[\hat{x}, \hat{p}] = i\hbar$, the new operators $\hat{a}$ and $\hat{a}^\dagger$ can be defined with the useful property that the commutation relation is now unity, $[\hat{a}, \hat{a}^\dagger] = 1$. We can rewrite the Hamiltonian in terms of a single operator, $\hat{n}$.

$$\hat{x} = \sqrt{\frac{\hbar}{2m\omega}}(\hat{a} + \hat{a}^\dagger),\ \hat{p} = i\sqrt{\frac{m\hbar\omega}{2}}(\hat{a}^\dagger - \hat{a})$$
$$\hat{H} = \hbar\omega(\hat{n} + \frac{1}{2}),\ \hat{n} = \hat{a}^\dagger\hat{a}$$

In the basis of number states $\hat{n}$, the QHO Hamiltonian consists of evenly spaced energy levels offset by a minimum energy stemming from the uncertainty relation for the system, $\frac{1}{2}\hbar\omega$. The operators $\hat{a}$ and $\hat{a}^\dagger$, known as annihilation and creation (or ladder) operators, change an eigenket $|n\rangle$ by one, allowing the construction of all eigenstates for the Hamiltonian, often referred to as Fock states, starting from only the ground state $|0\rangle$ and the ladder operators. Under a constant external excitation, a cavity with finite loss settles into a coherent state, whose photon-number distribution is Poissonian and which minimally satisfies the uncertainty relation while also featuring entirely classical dynamics [65]. Beginning with a classical mass on a spring, we arrived at a field theory of massless excitations, a representation of electromagnetic fields and interactions mediated by photons. However, at this point, all of the interactions we have alluded to so far have been electromagnetic, but we have yet to introduce a single circuit term!

A lossless LC circuit can be represented as a quantum harmonic oscillator [66, 67]. We can choose different canonical conjugates: the charge across the capacitor and the flux through the inductor in a lumped-element LC circuit.

$$\hat{H} = \frac{\hat{Q}^2}{2C} + \frac{\hat{\Phi}^2}{2L}$$
$$\hat{Q} = i\sqrt{\frac{C\hbar\omega}{2}}(\hat{a}^\dagger - \hat{a}),\ \hat{\Phi} = \sqrt{\frac{\hbar}{2C\omega}}(\hat{a} + \hat{a}^\dagger)$$

Superconducting circuits has become one of the most thoroughly studied and successful platforms for exploring quantum mechanics on a macroscopic scale over the past few decades, offering a versatile toolbox for exploring quantum phenomena and strong coherence and interaction strengths relative to other experimental approaches [42]. Splitting the zero-point energy of the oscillator equally into its capacitance and its inductance, we recover voltage and current fluctuations which produce electric and magnetic fields that can be used to

couple to other systems.

$$\frac{1}{4}\hbar\omega = \frac{1}{2}CV_{RMS}^2,\ \frac{1}{2}LI_{RMS}^2$$
$$V_{RMS} = \omega\sqrt{\frac{\hbar Z}{2}},\ I_{RMS} = \omega\sqrt{\frac{\hbar}{2Z}}$$

In the quantum-mechanical ground state, the characteristic impedance Z of the circuit satisfies the familiar relation $V_{RMS} = I_{RMS}Z$. Writing out the most general interaction Hamiltonian with these values yields a striking observation: for circuits, coupling through the electric field is significantly easier than through the magnetic field.

$$g_V \approx e\vec{E}_{RMS}\cdot\vec{d},\ g_I = \vec{\mu_B}\cdot\vec{B}_{RMS}$$
$$\frac{g_V}{g_I} = \frac{eZd}{\mu_0\mu_B}$$

The characteristic impedance of the simplest model of a cavity or transmission line (which can be represented as an infinite series of oscillators [68]), a vacuum-filled cylinder, is

$$\frac{1}{2\pi}\sqrt{\frac{\mu_0}{\epsilon}}\ln\left(r_{outer}/r_{inner}\right) \approx \frac{1}{2\pi}Z_{vac} \approx 60\,\Omega$$

Optimizing the circuit geometry for lower or higher impedance can only shift the value to within an order of magnitude or so. Generally, leveraging material and dielectric properties to increase the impedance beyond this range is more straightforward than building ultralow-impedance circuits. For typical impedances and length scales of hundreds to thousands of nanometers, coupling through the electric field is orders of magnitude more efficient than through the magnetic field.

The exploration of quantum-mechanical effects with only this one tool, however, is limited. The simplest experiment possible is sending photons of a fixed energy towards the resonator while monitoring for photons emitted from the resonator. Because the energy

levels are evenly spaced, the resonator will indefinitely absorb and emit photons near its resonant frequency with a spectral linewidth determined by losses internal to the resonator and the coupling to our external measurement equipment. While resonators have been utilized to a remarkable degree in the study of superconducting materials, radiative environments, dielectrics, and more [69], the richness of our experimental landscape is more apparent when we add nonlinearity to our system. That is to say, we would like a qubit!

2.3 The Jaynes–Cummings Hamiltonian

To observe dynamics originating from quantum-mechanical effects rather than classical evolution like that of a coherent state, we need to add photon-number-dependent interactions. While there are different ways to supply this nonlinearity, typically the nonlinear object of interest in cQED is a qubit. Ideally, the qubit is a true two-state system, so its response to stimulus is of course dependent on its state. Since some of the pioneering experiments in cavity quantum electrodynamics studied the spectral lines of atomic species in three-dimensional cavities [57], a two-state system interacting with a bosonic field is often referred to as an 'artificial atom.' Unlike a cavity, however, which continuously emits and absorbs photons, there is at most a single photon's worth of signal intensity from a qubit emitting in vacuum. The strategy of cavity QED is to integrate the two to enhance interactions with the qubit. Often, the only spectral signature probed directly is that of the cavity. We can write the joint Hamiltonian as

$$\hat{H} = \hbar\omega_c(\hat{n} + \frac{1}{2}) + \frac{\hbar\omega_q}{2}\sigma_z + \hbar g\sigma_x(\hat{a} + \hat{a}^\dagger)$$

In a reference frame rotating at the cavity's transition frequency, if the cavity and qubit transition frequencies are somewhat comparable, we can discard the faster-rotating terms

$\omega_c + \omega_q$ to arrive at the famous Jaynes–Cummings Hamiltonian:

$$\hat{H} = \hbar\omega_c(\hat{n} + \frac{1}{2}) + \frac{\hbar\omega_q}{2}\sigma_z + \hbar g(\hat{a}\sigma^+ + \hat{a}^\dagger\sigma^-)$$

We immediately see the 'reversibility' of spontaneous photon emission of the qubit; the interaction term shuffles photons between the cavity and the qubit at rate g. However, we also retain the benefits of a continuous excitation of the cavity looking largely classical. While this representation lacks dissipation and drive, we can still intuit the regimes of interest. First, we diagonalize the Hamiltonian in the basis of the number states $|n\rangle$ in the subspace of single-photon transitions ($|g, n+1\rangle, |e, n\rangle$).

$$\hat{H}/\hbar = \begin{pmatrix} (n+1)\omega_c - \omega_q/2 & g\sqrt{n+1} \\ g\sqrt{n+1} & n\omega_c + \omega_q/2 \end{pmatrix}$$

$$E_n^\pm/\hbar = (n + \frac{1}{2})\omega_c \pm \frac{1}{2}\sqrt{(\omega_c - \omega_q)^2 + (2g\sqrt{n+1})^2}$$

$$|+, n\rangle = \sin\theta\,|n+1, g\rangle + \cos\theta\,|n, e\rangle$$

$$|-, n\rangle = \cos\theta\,|n+1, g\rangle - \sin\theta\,|n, e\rangle$$

Hybridization of the bare cavity and qubit Hamiltonians leads to a coherent mixture of cavity and qubit states near resonance, with mixing angle $2\theta = \arctan\frac{2g\sqrt{n+1}}{\omega_c - \omega_q}$. If the interaction rate between the cavity and qubit exceeds their linewidths κ and γ, on resonance, it is possible to resolve the splitting of the cavity resonance into two distinct peaks corresponding to the two states of the qubit. This 'vacuum Rabi splitting' makes direct measurement of the coupling strength possible [70].

In this so-called 'strong-coupling' regime, the interaction rate exceeds the system losses, making observation of discrete photon interactions possible. However, coupling to the cavity

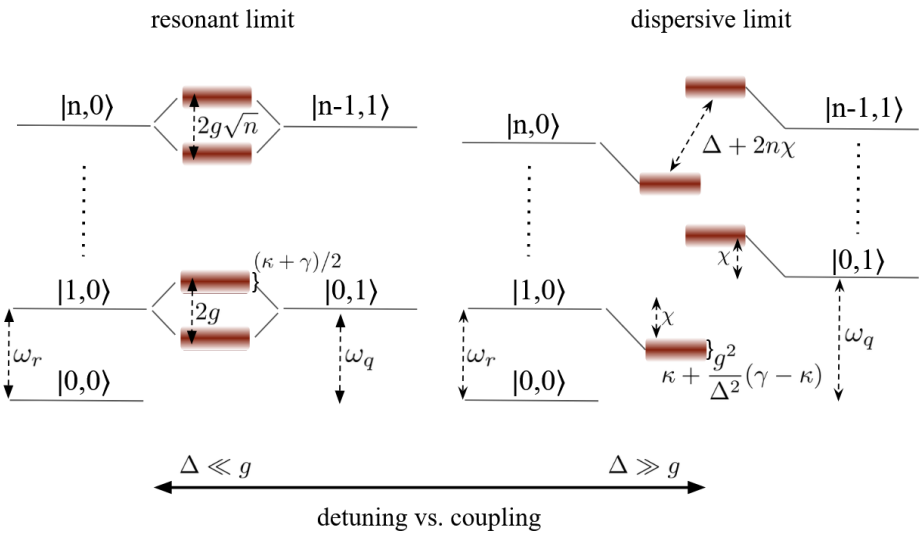


Figure 2.1: Jaynes–Cummings Hamiltonian ladder of states
In the case of small cavity-qubit detuning $\Delta = \omega_q - \omega_r$, the ladder of states is modeled with degenerate perturbation theory. The cavity and qubit are strongly hybridized, and on resonance, the driven cavity spectral line splits into two branches associated with single-excitation differences between the qubit and cavity, with one branch being 'resonator-like' and the other 'qubit-like.' The spectral linewidths are an equal mixture of the bare lines. When the detuning significantly exceeds the bare spectral linewidths κ and γ and the coupling rate g, the system enters the dispersive regime. The cavity inherits some of the qubit linewidth and a dispersive shift $\chi = \frac{g^2}{\Delta}$ dependent on the qubit state. While the cavity can be driven strongly, the qubit remains largely in its ground state due to the detuning between the two, and must be excited by a second, resonant pulse.

can also enhance the decay of the qubit, often referred to as Purcell decay with dispersive-limit rate [57, 59]

$$\gamma_q = (\frac{g}{\Delta})^2 \kappa_c$$

By detuning the qubit from the cavity, we enter the dispersive regime, where the weaker hybridization results in distinct 'cavity-like' and 'qubit-like' modes. The Schrieffer–Wolff transformation, in this case a unitary transformation of the Hamiltonian

$$\hat{U} = \exp\Big\{ \frac{g}{\Delta}(\hat{a}\sigma^+ - \hat{a}^\dagger\sigma^-) \Big\}$$

yields the dispersive Hamiltonian [71]

$$\hat{H}/\hbar = \frac{\omega_c}{2} + (\omega_c + \frac{g^2}{\Delta}\sigma_z)\hat{n} + \frac{\sigma_z}{2}(\omega_q + \frac{g^2}{\Delta})$$

The cavity transition frequency shifts according to the qubit state. We now have photon-number-dependent behavior of the cavity frequency from which the state of the qubit can be inferred. In this limit, we can probe the state of the qubit with only the spectral line of the cavity. In the dispersive regime, the mixing angle is small, so each eigenstate has single-photon excitation participation in mostly the qubit or mostly the resonator. Measuring the cavity state projects the qubit into the state measured since σ_z commutes with the interaction term. The state of the qubit can therefore be measured multiple times without leakage of information from the qubit, affording a significant increase in measurement contrast. This 'quantum non-demolition' measurement is one of the hallmark techniques of circuit quantum electrodynamics [72, 73].

Maintaining the coherence of the qubit and cavity together is key to observing quantum-mechanical dynamics in the system. With only a cavity, a continuous external excitation simply produces a coherent state of intracavity photon numbers. Adding a continuous drive to the cavity (or qubit: they are identical up to a rescaling of the drive strength $\epsilon_d \rightarrow \frac{2g}{\omega_c - \omega_d}\epsilon_d$) when it is coupled to the qubit adds a drive term to the dispersive Hamiltonian.

$$\hat{H}/\hbar = \hat{H}_0 + \epsilon_{drive}(t)\cos(\omega_{drive}t + \phi)(\hat{a} + \hat{a}^\dagger)$$

We can perform another Schrieffer–Wolff transformation to again absorb the leading-order interaction into the bare Hamiltonian. Isolating the qubit contribution, we find a Hamiltonian whose energy varies as a function of the accumulated phase of the applied excitation.

$$2\tilde{H}/\hbar = (\omega_d - \omega_q)\sigma_z + \frac{2g\epsilon(t)}{\omega_c - \omega_d}(\sigma_x \cos\phi + \sigma_y \sin\phi)$$

For driving the cavity, the drive strength ϵ_d is proportional to $\sqrt{\frac{\kappa_c P_{in}}{\hbar\omega_d}}$. By varying the pulse time and detuning while measuring the response of the cavity in the dispersive coupling regime, a 'chevron' pattern appears. Continuous pulses rotate the expectation value of the qubit's population in time, leading to Rabi oscillations with half-periodicity corresponding to what is typically referred to as a 'π-pulse.' The shape of the pattern off-resonance is sensitive to the shape of the pulse [74].

$$2\tilde{E}^{\pm}/\hbar = \pm\sqrt{(\frac{2g\epsilon_d}{\omega_c - \omega_d})^2 + (\omega_d - \omega_q)^2}$$

On resonance, the propagator of the Hamiltonian is a rotation $U = \exp\Big(-\frac{i\theta}{2}\hat{n}\cdot\hat{\sigma}\Big)$, where θ is the accumulated phase due to the drive.

Finally, we complete our discussion of the basic physics of the Jaynes–Cummings Hamiltonian by adding information leakage and making the drives finite in time rather than continuous. With dissipation, the system evolution is no longer unitary, but we can model the dynamics with the Lindblad master equation [75]

$$\dot{\rho} = -\frac{i}{\hbar}[H,\rho] + \kappa_c\mathcal{D}[a]\rho + \gamma_{1,q}\mathcal{D}[\sigma^-]\rho + \frac{\gamma_{\phi,q}}{2}\mathcal{D}[\sigma_z]\rho$$
$$\mathcal{D}[L] = L\rho L^\dagger - \frac{1}{2}\Big\{L^\dagger L, \rho\Big\}$$

Diagonal terms $\rho_{nm}, n = m$ represent decay of the qubit from its excited state back to its ground state, characterized by a relaxation time T_1 or decay rate $\gamma_{1,q}$. Off-diagonal terms represent relative rotations between the ground and excited states with a dephasing rate $\gamma_\phi + \gamma_1/2$. If we exclude the term which includes leakage of the cavity κ_c, the resulting

density matrix evolution is given by

$$\dot{\rho} = \begin{pmatrix} -\gamma_1\rho_{11} & (-i\omega_q - \gamma_1/2 - \gamma_\phi)\rho_{12} \\ (i\omega_q - \gamma_1/2 - \gamma_\phi)\rho_{21} & \gamma_1\rho_{11} \end{pmatrix}$$

Since experiments typically take place at temperatures ≈ 10 mK, the thermal population of the qubit is nearly entirely in the ground state. Therefore, rotating the qubit by π excites it from the ground state. By pulsing for a finite time and varying the wait time between pulses, we study the population decay statistics of the qubit, revealing the characteristic lifetime. In order to measure the dephasing or coherence, we instead apply a $\pi/2$-pulse to move the system evolution to the time it is maximally sensitive to phase fluctuations between the ground and excited states. By varying the time it is allowed to evolve in this configuration and then applying another $\pi/2$-pulse, one recovers fringes at the detuning between the drive and the qubit, much like Rabi flopping, which decay in time (Ramsey decay) towards equal population expectation in the ground and excited states, characterizing the total dephasing time of the qubit. It is even possible to interrogate this measurement sequence further to recover the spectral density of the noise responsible for the dephasing by interrupting the sequence with refocusing π-pulses, which apply a filter to the noise sensitivity of the phase.

2.4 Integrating an Electron Oscillator into Circuit QED

Finally, we arrive at the subject of integrating an electron on helium with superconducting circuits. What would an electron on helium look like as the qubit in such a system? Much like a transmon, an electron oscillator is not a two-state system. Rather, it is an anharmonic oscillator. When the anharmonicity is adequately large and the detuning is chosen appropriately, then for sufficiently weak cavity drives, the electron behaves largely as a two-state system [74, 76]. While higher-order states are utilized in cQED in some cases, unintended excitation of the qubit to higher-order states without correction generally constitutes leak-

age of information out of the computational subspace [77]. Driving strongly enough creates nonzero population density in these states.

$$\hat{H}/\hbar = \frac{\omega_c}{2} + (\omega_c + \chi\sigma_z)\,\hat{n} + \frac{K}{2}\hat{n}\,(\hat{n}-1) + \frac{\sigma_z}{2}\left(\omega_q + \chi\right)$$
$$\chi = \frac{g^2}{\Delta}\frac{\alpha}{\Delta+\alpha}, \qquad K = \frac{\chi^2}{\alpha}$$

For a ladder of constant anharmonicity, to leading order, the dispersive Hamiltonian shows the cavity now responding quadratically to the intracavity photon number. Furthermore, we see that for an oscillator of finite anharmonicity like a transmon qubit, the cavity Stark shift and the qubit's Lamb shift are suppressed in comparison with our original dispersive Hamiltonian. In addition to setting limits on gate speed or drive strength, the anharmonicity affects dispersive readout since the cavity has inherited its own nonlinearity. We discuss this more in-depth with experimental results in Chapter 6. It is worth mentioning that for trapped electrons on helium, harmonic confinement is also of great interest for potentially increasing spin-orbit interaction strengths in magnetic field gradients.

An electron oscillator is suitable for integration with superconducting circuits as a charge qubit [22, 29]. The transition dipole moment of its orbital states can be fairly large ($\approx e \times$ 50 nm) and is approximated by the zero-point fluctuations of a trapped harmonic oscillator:

$$x_{zpf} \approx \sqrt{\frac{\hbar}{2m\omega_q}}$$
$$\hbar g = -\vec{d}\cdot\vec{E} = eE_{RF}x_{zpf}$$

Like a transmon, the electron orbital states couple to a superconducting resonator via a transition dipole interaction with the electric field resulting from the zero-point voltage fluctuations of the resonator. While an electron cannot be brought arbitrarily close to a resonator like a transmon can, the transition dipole moment is still relatively large since the

electron mass is small. The major contrast between the two is that while the qualitative shape of the cosine potential of a transmon is constant with transition frequency tuning, the confining potential of an electron levitating on helium can in principle be shaped to an arbitrary curvature. This distinction is the primary focus of the experiments in this dissertation.

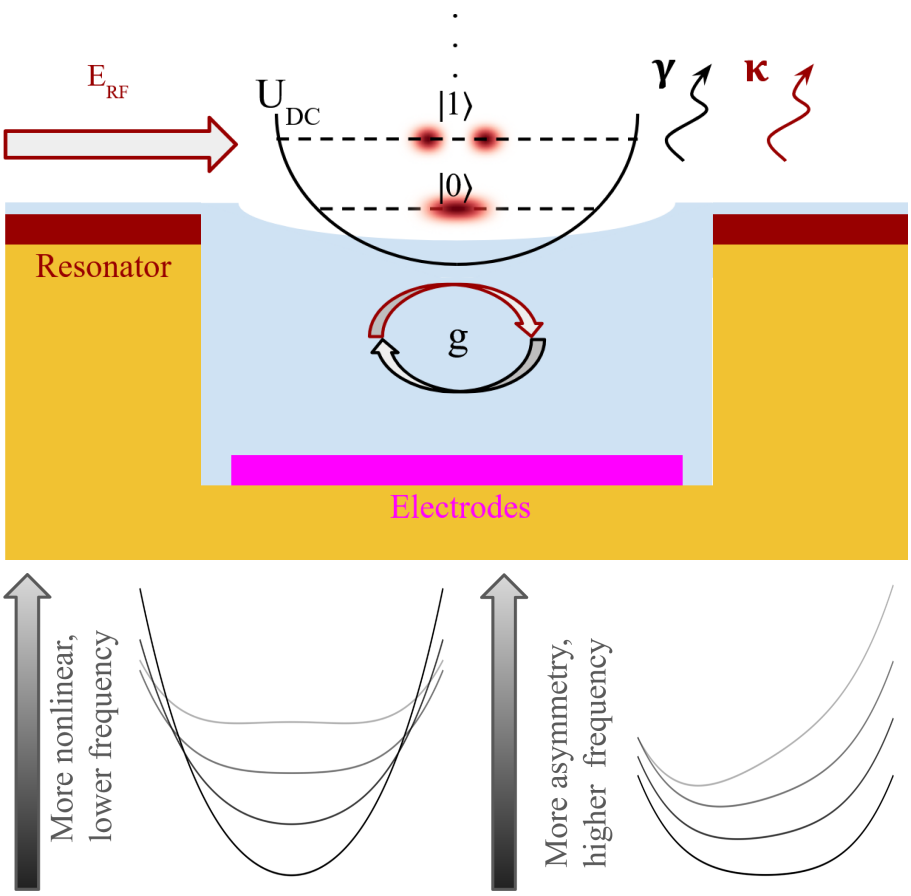


Figure 2.2: Coupling to an electron on helium with a microwave resonator
A superconducting microwave resonator produces a dynamic electric field proportional to its excitation number. An electron near this 'cavity' interacts with its photon field through an electric dipole interaction. The transition dipole moment and transition frequencies of the electron motion lateral to the helium surface are determined by shaping a confining electrostatic potential with nearby electrodes. 'Flattening' the trap amounts to increasing the higher-order coefficients of the trapping potential relative to the quadratic coefficient, lowering the frequency while increasing the nonlinearity of the oscillator. Asymmetry generally increases the frequency and softens the nonlinearity.

CHAPTER 3

ORBITAL STATES OF AN ELECTRON ON HELIUM

While it is clear that an electron in an anharmonic potential could serve as a qubit, it is naturally valuable to inspect the actual system at hand, an electron on helium trapped above a semiconducting substrate with superconducting electrodes. In practice with such a device, the applied electrostatic potentials are often neither symmetric nor the only confining potentials present. This chapter discusses the computational methods used to approximate the state transition frequencies of the electron oscillator. Considering typical system parameters such as local field asymmetry, the helium surface curvature, and trap depth, we discuss bounds on reasonable electron parameters, including decay and dephasing mechanisms for the electron oscillator; after all, we are of course concerned with the feasibility of an electron-on-helium qubit.

3.1 Modeling the Electron as an Anharmonic Oscillator

Assuming for the moment that the only relevant trapping potential is the one deliberately created via the device electrodes, the transition frequencies of the electron oscillator can be estimated in several ways [22, 29]. Perhaps the most obvious is to numerically solve the Schrödinger equation for the trapped electron. The eigenvalues of the system yield the electron energies while the transition dipole elements can be calculated from the overlap of the relevant eigenmodes. The vertical and lateral solutions, χ and φ, are generally separable in the regime that we are interested in since their energy scales differ by over an order of magnitude. The first transition dipole moment for the lateral states is of the order $\sqrt{\frac{\hbar}{2m_e\omega_e}}$, or about 50 nm for a 6 GHz transition, so the mesh over which the potential is generated for the simulation must sample an order of magnitude finer for solutions to be spatially

convergent in three dimensions.

$$\Psi = \varphi(x,y)\chi(z)e^{-iEt/\hbar}$$
$$\left[-\frac{\hbar^2}{2m_e}\left(\partial_x^2+\partial_y^2\right)+V_{\text{lat}}(x,y)\right]\varphi = E_{\text{lat}}\varphi$$
$$\left[-\frac{\hbar^2}{2m_e}\frac{d^2}{dz^2}-\frac{\Lambda e^2}{z}+eE_z z\right]\chi(z) = E_z\chi(z)$$
$$d = -e\int \varphi_n^*(x,y)\, x\, \varphi_m(x,y)\, dx\, dy$$

A useful approximation that avoids the computational time associated with solving the Schrödinger equation for many system parameters is to lean into the assumption of the electron as a perfect oscillator. Fitting a symmetric trapping potential to a form $V = \sum_i a_i x^i$ to quartic order immediately yields the first transition energy $\omega_e = \sqrt{2ea_2/m_e}+\alpha$, analogous to solving for the oscillation frequencies of a mass on a spring. The anharmonicity of a symmetric trap can be approximated by taking the expectation value of the quartic moment, $\langle n|\,\hat{x}^4\,|n\rangle$, evaluating to $\alpha = \frac{3\hbar a_4}{2m_e a_2}$ [78].

Ideally, the properties of the orbital states would depend solely on the electric field generated by the trapping electrodes. Significant corrections can be observed in experiments, however, and can be reasonably modeled by adjusting the model of the anharmonic oscillator. Most visibly, the trapping potential at the electron location is typically axially asymmetric, possibly due to device fabrication imperfections, nearby stray electrons, or substrate charge impurities. In our earlier model, an external lateral electric field contributes a potential term xE_x and shifts the electron position away from the symmetric well minimum by approximately $x_0 = E_x/(2a_2)$. At the new location of the electron, this adds a cubic moment to the potential which corrects the anharmonicity. The new first transition frequency and

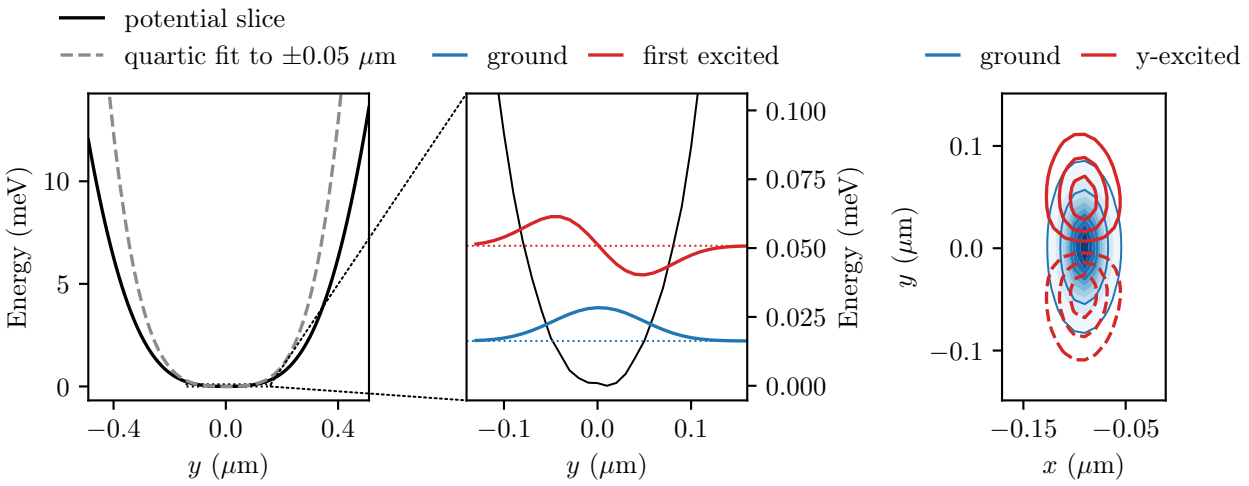


Figure 3.1: Simulation of orbital state properties

The simplest method for obtaining the electron orbital state ladder properties from a simulated confining potential is to fit a polynomial to the trap. The electron only feels the potential to the extent of its ground-state wavefunction and its motion can be modeled effectively classically. A better method, especially when contributions of higher-order or asymmetric polynomial terms are significant, is to solve the Schrödinger equation for an electron in the simulated potential. In two dimensions, dipole mixing for asymmetric or rotated traps can be modeled.

anharmonicity are given as

$$\alpha = \frac{3\hbar a_4}{2m a_2'}\left[1 - \frac{20 a_4 x_0^2}{a_2'}\right], \qquad a_2' = a_2 + 6a_4 x_0^2, \qquad \omega_{01} = \omega + \alpha$$

The most pronounced symptom of this correction is an observed minimum frequency for the electron that is much higher than a symmetric trapping potential model would suggest. Even for modest asymmetries on the order of 1 mV/μm, the minimum trapping frequency is already a few GHz! The state ladder becomes more harmonic as well, owing to the fact that the potential well cannot 'flatten' into a regime where the quartic moment is comparable to the quadratic.

$$\omega_{min}^2 = \frac{12e\, a_4^{1/3}}{m_e}\left(\frac{E_x}{4}\right)^{2/3}$$

Another correction to the orbital frequency comes from the helium surface itself. In a microchannel geometry, the shape of the helium is set by the capillary tension of the liquid in the channel. The radius of curvature of the helium in the microchannel can be approximated from the sample cell dimensions as $R_c = \frac{\sigma}{\rho g h}$, where h is the distance between the top of the microchannel and the surface of the helium bath sitting at the lowest point in the device, ρ is the helium density, and σ is the surface tension of superfluid helium-4 [79]. Since the mobility

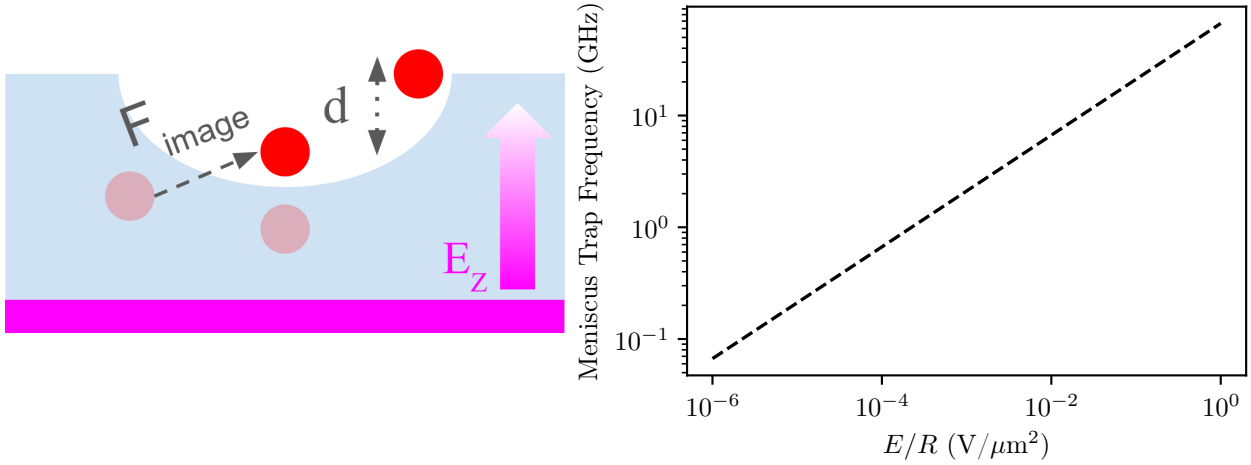


Figure 3.2: Contribution of helium surface curvature to the electron trap
In a microchannel geometry, the capillary forces which fill the channel result in a curved helium surface. The radius of curvature is determined by the channel geometry and the vertical distance to the bulk helium bath which sits at the bottom of the sample cell. The electron image charge and the vertical potential energy due to confining electrodes beneath the helium surface result in a curvature- and pressing-field-dependent contribution to the orbital state transition frequency. With typical device parameters, this results in an effective minimum frequency of up to 2 GHz.

of the electron is high, it will minimize its potential energy in the microchannel, fluctuating about the extremum of the channel curvature, with the depth of the potential set by the magnitude of the image charge attraction and pressing field. For helium microchannels with nanometers of variation in vertical displacement over several microns of width, this typically

evaluates to several hundred MHz for vertical electric fields in the range of 100 mV/μm.

$$U_{curv}(x) \approx U_0(x) + \frac{eE_z}{2R_c}x^2$$
$$\omega_{min} \approx \sqrt{\frac{eE_z}{m_e R_c}}$$

Even in an experiment on a van der Waals film that does not rely on microchannels, the helium itself still provides a similar correction to the orbital transition frequencies. For a level helium surface, the electrostatic pressure of the electron deforms the helium beneath it. The curvature of this 'dimple' distorts the image charge, forming a weak self-trapping potential, though the electron is still free to move about the helium surface in this case. This correction is much smaller than the previous two since the dimple depth is typically on the angstrom scale.

At this point, it is also worth considering the effect of the electron mobility on the helium surface, if only to clarify how the high mobility is not only a measure for system 'cleanliness' that suggests low decoherence, but that it also plays an important role in measurement of the electron orbital states. The mobility of an electron gas on the helium surface can exceed 10^7 cm^2/(V s) in microchannel geometries, limited by fluctuations of the helium surface below 700 mK [80]. The electron is well separated from the rough dielectric and metal surfaces, and the vapor pressure of helium-4 is negligible. Damping of the electron oscillator is usually ignored in this case. Even over a van der Waals thin film where the mobility declines by several orders of magnitude due to electron pinning by surface roughness, the mobility remains as high as some of the best semiconductor systems [81, 82]. Treating the electron as a damped oscillator where the surface mobility is analogous to the damping rate, it is clear that a low mobility overdamps the system, preventing efficient driving of the motion at microwave frequencies. This is one reason why microchannel geometries have been particularly successful for studying electrons on helium while electrons on solid gases

such as neon and hydrogen, systems with significantly less mobility and even higher electron areal densities, can be difficult to study in the microwave regime [8, 83].

$$m\ddot{x} = -m\omega_0^2 x - m\gamma\dot{x}$$
$$\gamma = \frac{e}{m\mu}$$
$$\omega_d = \sqrt{\omega_0^2 - \frac{\gamma^2}{4}}$$

For a test potential, the solution methods agree well for the lowest transition frequencies of the electron in the well, with some exceptions. When the quartic well bisects, the electron localizes to one side of the well, leading to a non-monotonic dependence of the frequency on the moments of the well. The tunneling length scale of the electron $\sqrt{\frac{\hbar^2}{2m_e U_{barrier}}} \lesssim 5$ nm is far below the micron length scale of the electron traps, so the tunneling time $\frac{2\pi}{\omega_e} e^{2l_{barr}/l_{tunn}} \gtrsim$ 1 year for a 100 nm barrier is too long to be of importance except for a narrow range of parameters right as the potential splits. Near this regime, there is some disagreement between the numerical solution methods since fitting the potential does not consider it. Similarly, the anharmonicities between transitions agree less well between the numerical methods than the frequencies since the dimensionality of the model plays a larger role as the wavefunction expands to higher modes.

Evidently, electron orbital states are highly compatible with cQED. Trapping frequencies in the microwave frequency range are naturally achieved at the micron length scale for the electron trap for some tens to hundreds of millivolts of electrode bias. At higher biases, experiments might contend with leakage current between electrodes through the substrate. At lower biases, the length scale of the trap must be reduced so that the well remains deep enough to house the first few energy levels and tolerate higher-power drives without ejecting the electron; this brings the electron closer to the substrate, which is not nearly as clean as the helium surface. Recent interest in the upper-microwave and lower-millimeter-wave

regime is also exciting for the platform since these frequencies are just as accessible and pair well with the use of high-kinetic-inductance materials, though the state ladders tend to be significantly more harmonic [84].

3.2 Dephasing due to Ripplons

Uniquely, the substrate nearest an electron on helium is, of course, a liquid. This presents some challenges for the system. In this section, we analyze electron dephasing and discuss requirements for implementing charge qubit gates with electrons on helium imposed by the ripplonic bath [20, 33, 35]. Excitations of the helium surface, otherwise known as ripplons, follow a two-dimensional dispersion relation $\omega_{rip} \approx \sqrt{\frac{\sigma_{he}}{\rho l_x^3}}$ for thicker helium films and $\omega_{rip} \approx q\sqrt{\frac{A_H}{2\pi\rho d_{he}^3}}$ for thinner films in the van der Waals limit (with A_H being the Hamaker constant, d_{he} the film thickness, and q the ripplon wavevector). Unlike the three-dimensional phonons near the electron transition frequency, the ripplons interacting most strongly with the electron have frequencies of tens of MHz, well below $k_B T/h$ even at 10 mK, so they remain thermally populated ($\bar{n} \approx k_B T/\hbar\omega_{rip}$) and their influence falls only linearly with temperature rather than freezing out. Since the electron is bound to the surface of the helium, the height variation from ripplonic excitations couples the electron to the thermal bath in two ways: variation of the electrostatic potential energy with height and distortion of the dielectric image charge. Decay due to ripplons is minuscule because the length scales of an electron and a ripplon of similar energies are too disparate, so their interaction rapidly averages away, and multi-ripplon processes still do not contribute on a relevant timescale. However, ripplons do introduce significant dephasing [20, 22, 33].

Ripplonic excitations perturb each energy level differently, leading to dephasing. Ripplons on the length scale of a single electron have a thermal mean frequency $\bar{\omega} \approx \sqrt{\frac{\sigma_{he}}{\rho x_{zpf}^3}}$, which is in the tens of MHz for microwave-range electron transition frequencies. Therefore, the perturbation of the electron energy levels is entirely dispersive. Since the ripplon is a curved

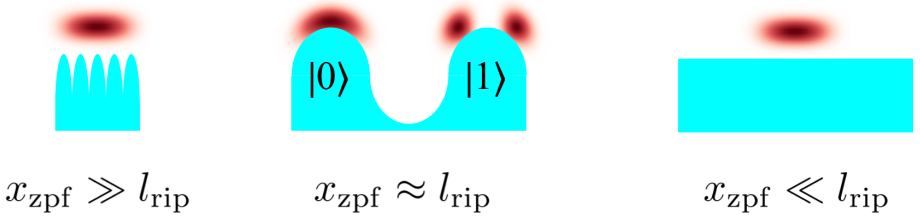


Figure 3.3: The electron wavefunction on a curved ripplon surface
The electron wavefunction is bound to the helium surface at a constant distance. Surface excitations of the helium, ripplons, morph the helium surface and its image charge potential. When the ripplon wavelength is significantly smaller than the extent of the electron wavefunction, the coupling to the ripplon field largely averages away. When the ripplon wavelength is relatively large, the electron feels no curvature but can feel height variation of the electrostatic trap curvature $\partial\omega/\partial z$. When the two have comparable length scales, the curvature of the ripplon causes the electron to sample the total confining potential energy differently in its ground and excited orbital states, modulating the transition frequency and resulting in dephasing of the orbital state.

surface and the electron wavefunction's spatial extent increases with excitation number, each electron energy level samples the interaction differently, leading to nonuniform shifts. This introduces transition frequency noise on the characteristic timescale of the ripplons. For the generic electron trapping geometries described in this thesis, the electron interacts with the ripplons in primarily three fashions: distortion of the dielectric image charge immediately below the helium surface, modulation of the electron potential energy from vertical separation of biased electrodes beneath the helium, and a non-constant electrostatic trap curvature as the electron height changes due to utilization of multiple electrodes. To analyze these interactions, we write the bare electron Hamiltonian as

$$\hat{H}_{el} = \frac{\hat{p}_z^2}{2m_e} - (\frac{\Lambda e^2}{\hat{z}} - U_{He}(\hat{z})) + eE_z\hat{z} + \frac{1}{2}m_e\omega_x^2\hat{x}^2 + U_{el}(\hat{x},\hat{z})$$

The first term represents excitations in the vertical direction (the Rydberg states), which are effectively frozen to the ground state since the typical transition frequency is 100 GHz $\gg k_BT/h$ and also far exceeds the typical motional transition frequency. The second term represents the potential energy due to the binding of the electron to the helium surface by

its image charge and the repulsive energy of the insertion cost into the helium. The third is the Stark shift of the Rydberg energy levels associated with the external pressing electric field E_z perpendicular to the helium surface; for typical device geometries, this term is not small at 100–10 000 V/cm, so it has been promoted to an operator in z. Finally, the lateral motion of the electron squeezed to one dimension and made harmonic for simplicity and the potential energy due to the electrodes' bias are described by the final two terms.

We proceed by calculating the interaction energy of each term considering the ripplonic Hamiltonian. The ripplons that couple most strongly to the electron have wavevectors $q \sim 1/l_x$, where l_x is the harmonic oscillator length of the electron, and the earlier dispersion relation sets their frequency ω_{rip}.

$$\xi_q^{\text{zpf}} = \left(\frac{\hbar q}{2\rho_{\text{He}} \omega_q S_{\text{He}}} \right)^{1/2}$$

$$\hat{\xi}(\mathbf{r}) = \sum_{\mathbf{q}} \xi_q^{\text{zpf}} \left[b_{\mathbf{q}} e^{i\mathbf{q}\cdot\mathbf{r}} + b_{\mathbf{q}}^\dagger e^{-i\mathbf{q}\cdot\mathbf{r}} \right]$$

$$H_r = \sum_{\mathbf{q}} \hbar\omega_q b_{\mathbf{q}}^\dagger b_{\mathbf{q}}$$

The interaction Hamiltonian, with $\hat{v}$ representing the interaction energy per unit vertical displacement, is

$$\delta\hat{H} = \sum_{\mathbf{q}} \xi_q^{\text{zpf}} \left[\hat{v}\, e^{i\mathbf{q}\cdot\mathbf{r}} b_{\mathbf{q}} + \hat{v}^\dagger e^{-i\mathbf{q}\cdot\mathbf{r}} b_{\mathbf{q}}^\dagger \right]$$

We obtain the interaction energy by evaluating $v(\mathbf{r}) = \left\langle \frac{\partial U}{\partial z}(\mathbf{r}, \hat{z}) \right\rangle_z$ for each term in the bare electron Hamiltonian in the comoving frame, where the unperturbed electron coordinate is static in the z direction and we instead introduce the curvature of the ripplon surface as a radial dependence. In this frame, the Stark shift interaction per ripplon amplitude is simply $V^{Stark} = eE$. The image charge interaction, often referred to as the polaronic term, follows the curvature of the ripplon. To first order in the comoving frame, there is no surface

variation, but to second order, the perturbation is of the form $\nabla^2\xi = -q^2\xi$. Therefore, the interaction evaluates to $V_{\mathbf{q}}^{(\mathrm{pol})} \simeq -\frac{\Lambda e^2 q^2}{2}\left[1 + \ln\frac{qr_B}{4}\right]$, where $r_B \approx 7.6$ nm is the effective Bohr radius of the vertical ground state. These interactions are not possible to engineer beyond changing the pressing field on the electron, and the image charge interaction can, of course, never vanish. The more controllable interaction is the curvature of the deliberate trapping potential for the electron. For an approximately harmonic trap, the perturbation in the energy also follows the curvature of the ripplon surface as $\frac{\partial}{\partial\xi}\left[\frac{\partial^2 U_{\mathrm{eff}}}{\partial r_i^2}\right] \approx \left\langle \frac{\partial^3 U_{\mathrm{el}}}{\partial r_i^2 \partial z}\right\rangle_z = \frac{\partial\omega_i}{\partial z}\hat{x}^2$. We can also add a term representing the coordinate minima of the electron potential changing with z-direction perturbations, $\frac{\partial x_{min}}{\partial z}$, but for the typical ripplon amplitude this term is small. Altogether, the perturbation is

$$\hat{v_q} = eE - \frac{\Lambda e^2 q^2}{2}\left[1 + \ln\frac{qr_B}{4}\right] + \frac{\hbar}{2}\frac{\partial\omega_i}{\partial z}\hat{x}^2$$

Since the ripplon bath is continuous and interacts dispersively with the electron, we can take the adiabatic approximation. There are no resonant interactions, and we only evaluate the diagonal terms of the Hamiltonian which commute with the bare electron Hamiltonian. The noise in the first transition energy is then

$$\hat{\Lambda}_{\mathbf{q}} \equiv \left[\hat{v}\, e^{i\mathbf{q}\cdot\mathbf{r}}\right]_{\mathrm{diag}}$$
$$\delta\hat{H} = \sum_{\mathbf{q}} \xi_q^{\mathrm{zpf}}\left[\hat{\Lambda}_{\mathbf{q}} b_{\mathbf{q}} + \hat{\Lambda}_{\mathbf{q}}^\dagger b_{\mathbf{q}}^\dagger\right]$$

Now, integrations across the trap curvature and ripplon density of states are separable. Integrating over the ripplon density of states, with $u = (ql_x)^2$, we finally arrive at the expression

$$\delta H_{\mathbf{q}} = \xi_q^{\mathrm{zpf}} e^{-u_x/2}\left[\hbar\frac{\partial\omega_x}{\partial z}\left(1 - \frac{5}{2}u_x + \frac{1}{2}u_x^2\right) - eEu_x - V_{\mathbf{q}}^{(\mathrm{pol})}u_x\right]$$

The off-diagonal elements of the reduced density matrix evolve as

$$\rho_{01}(t) = \rho_{01}(0)\, e^{-i\omega_{01}t}\, e^{-W(t)}$$

with the coherence function

$$W(t) = \sum_{\mathbf{q}} \left| \frac{\delta H_{\mathbf{q}}^{(1)} - \delta H_{\mathbf{q}}^{(0)}}{\hbar\omega_q} \right|^2 \Big[(2\bar{n}_q + 1)(1 - \cos\omega_q t) + i \sin\omega_q t \Big]$$

Therefore, the thermally weighted ripplon sideband density of states, the Debye–Waller factor $\bar{W}$, and the coupling strength between the ripplons and the electron are given as

$$\aleph(\Omega) \equiv \sum_{\mathbf{q}} \left| \frac{\delta V_{\mathbf{q}}}{\hbar\omega_q} \right|^2 \delta(\Omega - \omega_q)\, [2\bar{n}(\Omega) + 1]$$

$$\bar{W} = \int_0^\infty \aleph(\Omega)\, d\Omega,$$

$$\gamma_{\mathrm{rip}}^2 = \int_0^\infty \Omega^2 \aleph(\Omega)\, d\Omega$$

We immediately infer some design philosophies about improving the electron coherence. At pressing fields in excess of 1 kV/cm, which approximately amounts to biasing an electrode 1 μm away to 0.1–1 V, the transition frequency noise is easily dominated by the Stark shift of the Rydberg states. Below this, it is necessary to establish a lateral curvature insensitivity to height fluctuations of the electron, representing a frequency 'sweet spot' for the electron as a function of helium level in a microchannel geometry. Unfortunately, it is impossible to decouple the electron from modulation of its dielectric image charge by the curved ripplon surface, leaving it with a minimum coupling strength to the ripplonic bath of approximately 10 MHz for microwave-frequency lateral motion states.

While the coherence analysis looks similar to that of other platforms coupled to bosonic

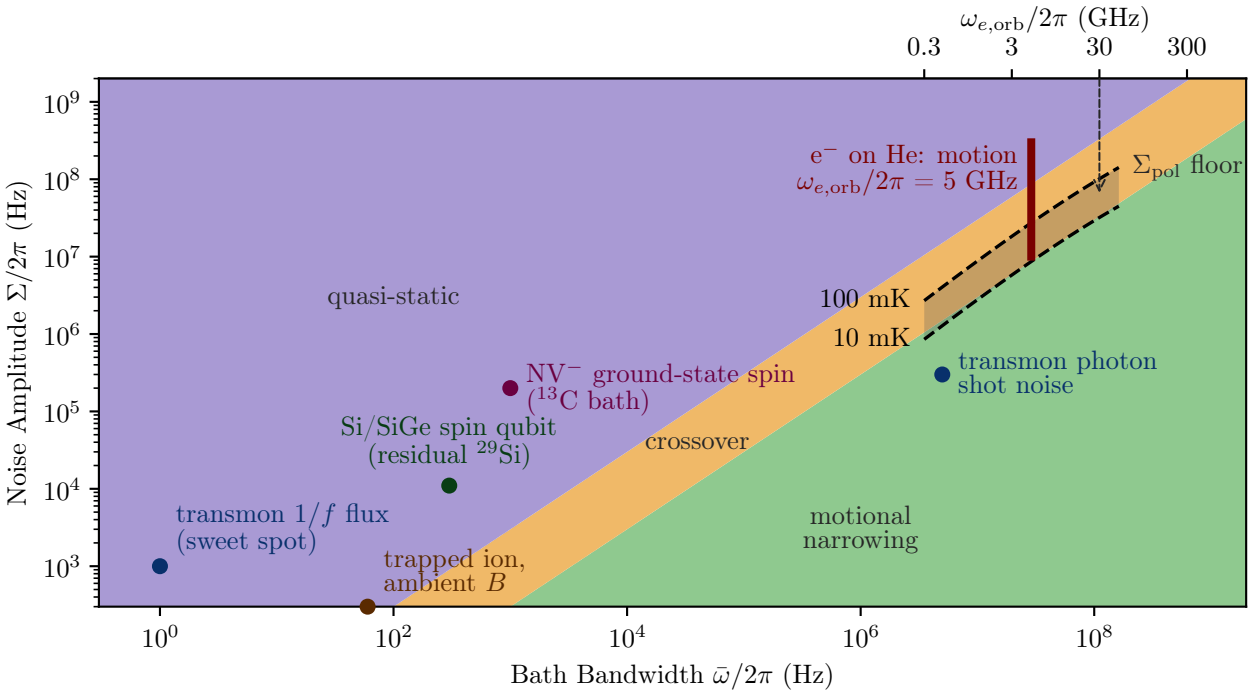


Figure 3.4: Anderson–Kubo criterion for electrons on helium
The Anderson–Kubo criterion [85, 86] characterizes how a qubit dephases in response to a noise source with known statistical properties. The noise causes fluctuations in the spacing between energy levels of the qubit. When the noise bandwidth is small relative to its amplitude, the noisy bath is slow enough that phase excursions of the qubit can be refocused; the noise is quasi-static and the phase coherence has a Gaussian decay profile. In the fast-bath limit, the fluctuations are fast and can average out, resulting in motional narrowing of the spectral line and an exponential or memoryless decay of the phase coherence. The ripplon bath bandwidth and amplitude grow with largely the same parameters, making them comparable for the orbital states of an electron on helium, straddling the two regimes.

baths, such as quantum dots or color centers to solid-state substrate phonons, the liquid film introduces some critical subtleties. Unlike in these other cases, the Debye–Waller factor $\bar{W}$ can span several orders of magnitude. $\bar{W}$ essentially places a flat penalty on the phase coherence of the charge state, caused by instantaneous scrambling of the electron phase by the bath at short timescales. For large $\bar{W}$, there is therefore never phase coherence of the charge state. The ratio $\gamma_{rip}/\bar{\omega}_{rip}$, the Anderson–Kubo criterion, illustrates why improving the phase coherence is particularly challenging in this case. The ripplon bath is slow compared with solid-state phonons but not slow compared with a measurement bandwidth or gate speed;

$\gamma_{rip}/\bar{\omega}_{rip}$ is of order unity for typical system configurations. For $\gamma_{rip}/\bar{\omega}_{rip} \ll 1$, motional narrowing is possible because the bath is fast, while for $\gamma_{rip}/\bar{\omega}_{rip} \gg 1$ refocusing the phase is possible, but neither is easily accessible to the system. Furthermore, noise at $\bar{\omega}_{rip}$ cannot be filtered away as in solid-state systems where the bath speed is usually orders of magnitude separated from the measurement bandwidth.

Luckily, while this makes for challenging experiments at present, the development of the platform should not be inhibited by these constraints. The noise induced by the bath is super-ohmic (vanishes at DC) except for the fluctuation of the trap curvature with height, so in the limit of weak coupling to ripplons, the memoryless or uncorrelated coherence which progresses as $e^{-\gamma_\phi t}$ is unaffected. For future efforts targeting the electron spin, as long as the detuning between the spin and the charge transitions is sufficiently large, one can trade coupling strength to the spin and gate speed for suppressing decoherence inherited from the charge's coupling to ripplons. Towards that purpose, it may not even be necessary to reach the weak ripplon coupling limit.

3.3 Decay due to Phonons

Unlike the ripplons, the phonons can be near-resonant with the electron, making the primary concern decay rather than dephasing. One-phonon decay is allowed, while one-ripplon decay is not since the phonon dispersion is three-dimensional. The additional degree of freedom reduces the constraints on the transverse momentum of the phonon. When most of the momentum is in the perpendicular direction to the helium surface, the density of states for near-resonant bath excitations increases significantly. We focus on single-phonon decay processes since two-phonon processes are higher order and contribute less decoherence [22].

Much like in our preceding calculation with ripplons, the strategy will be to first identify the coupling constants for each decay channel in the phonon interaction Hamiltonian: surface displacement associated with the pressing field term and the polarization term from

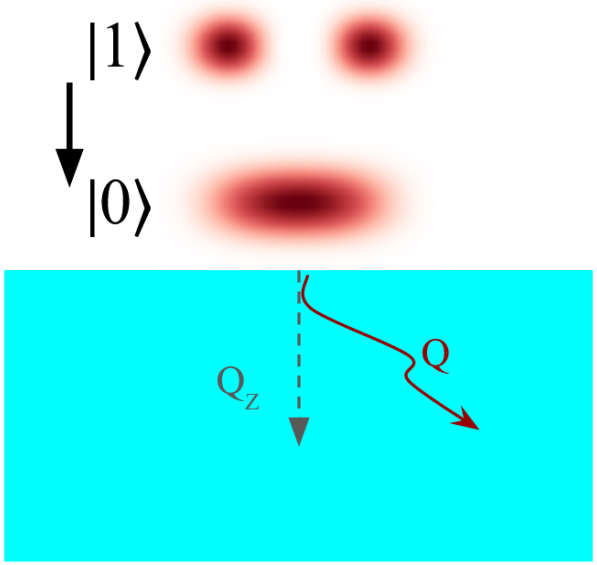


Figure 3.5: Phonon-induced orbital state decay
The orbital state decay lifetime for electrons on helium is most limited by single-phonon emission into the helium phonon bath. The bath of bulk helium excitations is three-dimensional, making single-phonon decay processes possible by adjusting the momentum of the phonon until a resonant coupling fraction exists, whereas resonant planar ripplons are too small to couple to the electron.

distortion of the image charge potential. Only the vertical component of the phonon momentum evaluated at the helium surface interacts with the electron, giving the phonon bath Hamiltonian:

$$\xi(\mathbf{r}) = \sum_{\mathbf{q}, Q_z>0} \xi_{\mathbf{Q}} \left[b_{\mathbf{Q}} e^{i\mathbf{q}\cdot\mathbf{r}} + b_{\mathbf{Q}}^{\dagger} e^{-i\mathbf{q}\cdot\mathbf{r}} \right]$$

$$\xi_{\mathbf{Q}} = \sqrt{2}\,\frac{Q_z}{Q}\sqrt{\frac{\hbar}{2\rho\,\omega_Q \mathcal{V}}}$$

The coupling to the curvature of the trapping potential is quadratic, so single-phonon decay is suppressed. We evaluate Fermi's golden rule, integrating over the density of states of the phonon bath. The interaction Hamiltonian contributions $\hat{v}$ are similar to the ripplon case, but the evaluation of the integral is slightly different since the nonzero matrix elements of

interest are those of single-phonon transitions.

$$\Gamma = \frac{2\pi}{\hbar} \sum_f |\langle f|H_{\text{int}}|i\rangle|^2 \, \delta(E_f - E_i)$$

$$\Gamma = \frac{2\pi}{\hbar} \sum_{\mathbf{Q}, Q_z>0} \left|\xi_{\mathbf{Q}}\right|^2 \left|\langle 0|\hat{v}\, e^{i\mathbf{q}\cdot\mathbf{r}}|1\rangle\right|^2 \delta(\hbar\omega_x - \hbar s Q)$$

This results in decay rates

$$\Gamma_{1,press} = \frac{(eE)^2 m_e}{2\pi\rho\hbar^2 s}$$

$$\Gamma_{1,pol} = \frac{3m_e\Lambda^2 e^4 (1 + \ln\frac{qr_B}{4})^2}{4\pi\rho\hbar^2 s\, l_x^4}$$

$$\Gamma_{1,x} \propto \frac{(Q_z/Q)^2}{8\pi^2\rho\hbar s\omega_x} \left(\frac{\hbar}{2}\frac{\partial\omega_x}{\partial z}\right)^2$$

While the electron lifetime can be relatively long for a charge qubit, the slowness of the excitations in liquid helium relative to solid dielectrics, notably solid neon, makes for surprisingly fast decay.

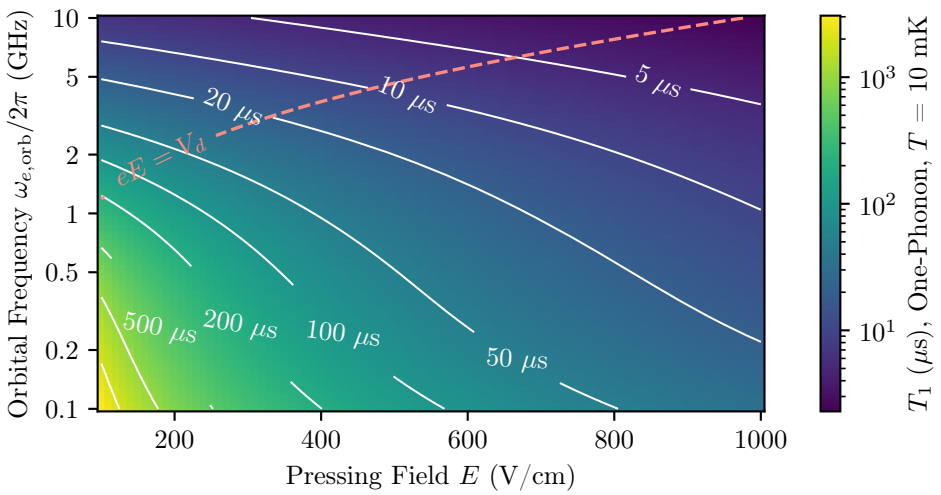


Figure 3.6: Simulated single-phonon limited decay lifetime of orbital states
The orbital transition frequency, pressing electric field which pulls the electron orthogonal to the helium surface, and system temperature determine the single-phonon process decay rate. Lower frequencies and weaker pressing fields generally result in longer lifetimes. With common experimental parameters, a 1–10 μs lifetime is expected, in line with some quantum dot systems. With relatively weak pressing field binding to the helium surface, frequencies on the lower end of the accessible range, and an electron temperature below 10 mK, the charge lifetime can reach 100 μs, which is exceptional for a charge qubit. Since the helium is a fluid, resonant phonons are slower than in other condensed matter systems, meaning they couple more effectively to the electron.

3.4 Johnson Noise

The electrodes of the electron trap are connected to the lossy circuits of equipment at room temperature. The electrode experiences fluctuations in its bias potential with a spectral density

$$S_V(\omega) = 2\hbar\omega \operatorname{Re} Z(\omega) \coth\left(\frac{\hbar\omega}{2k_B T}\right)$$

At low temperatures $\hbar\omega \gg k_B T$, this reduces to zero-point fluctuations of a transmission line of known impedance, allowing for spontaneous decay of the electron state into the lead impedance, otherwise known as Johnson relaxation or Johnson–Nyquist noise [87–89]. We compute the decay rate according to Fermi's golden rule for the force on the electron due to

the electric field produced by the voltage fluctuations.

$$\hat{H} = e\hat{x}(\frac{\partial E_x}{\partial V})\hat{V}$$
$$\Gamma_1 = \frac{e^2|x_{01}|^2}{\hbar^2}(\frac{\partial E_x}{\partial V})^2 S_V(\omega_x)$$
$$\Gamma_1 = \frac{e^2 \operatorname{Re} Z}{m_e}(\frac{\partial E_x}{\partial V})^2 \coth\left(\frac{\hbar\omega_x}{2k_B T}\right)$$

In the opposite limit, the effective frequency of the noise is 0, contributing to dephasing rather than decay.

$$\Gamma_\phi = \left(\frac{\partial \omega_x}{\partial V}\right)^2 k_B T \operatorname{Re} Z$$

Unlike in the case of bosonic bath noise, the spectral density is a constant at low frequency: white noise. The contribution to the electron emission spectra lineshape is therefore Lorentzian. In this case, motional narrowing is possible. Specifically, in the case of symmetric gates around the electron, the relaxation samples the impedance at ω_x while the dephasing samples at low frequencies.

3.5 Charge Noise

As a charge qubit, the electron is sensitive to fluctuations caused by nearby mobile charges. In comparison to quantum dots, the electron is well separated from two-level systems and impurities in the device substrate, making it largely insensitive to charge redistribution and fluctuations near the device surface. However, the motion of nearby charges, such as electrons outside of the trap, introduces charge noise to the trapped electron. Charge noise is generally quoted as an equivalent fluctuation of the bias gate charge at a given frequency [31, 90]. We

can write the spectral density of the voltage fluctuations on an electrode as

$$S_V(f) = \left(\frac{\sigma_q e}{C_g}\right)^2 \frac{f_1}{f}$$
$$S_{\delta\omega}(f) = \delta\omega_1^2 \frac{f_1}{f}$$

We integrate the noise spectral density with a free-induction filter to find a coherence function that is approximately Gaussian in time. Unlike in the case of ripplons, the characteristic frequency of the noise is typically low, making it somewhat amenable to refocusing techniques, which is typical of $1/f$ noise [91].

$$\langle \varphi^2(t) \rangle = t^2 \int_{f_0}^{\infty} df\, S_{\delta\omega}(f) \left[\frac{\sin \pi f t}{\pi f t}\right]^2$$
$$\left|\langle e^{i\varphi} \rangle\right|_{\text{FID}} = \exp\left\{-\frac{\delta\omega_1^2 f_1 t^2}{2}\left[\ln \frac{1}{2\pi f_{\text{lo}} t} + \frac{3}{2} - \gamma_E\right]\right\}$$

3.6 Radiation and Purcell Loss

The vacuum impedance for an electromagnetic wave is finite, so an excited electron can spontaneously emit a photon into vacuum. This occurs with rate

$$\Gamma_1^{(\text{v})} = \frac{4}{3}\frac{e^2}{\hbar c}\left(\frac{2\pi a_x}{\lambda}\right)^2 \omega_x$$

While this rate is small, the radiative emission can be enhanced in our experimental setup of interest. The electron can spontaneously emit into a lossy cavity coupled to it. The Purcell loss rate in the dispersive limit is:

$$\Gamma_1^{(\text{P})} = \frac{g^2 \kappa}{(\omega_x - \omega_c)^2}$$

3.7 Summary of Design Goals

For convenience, I have listed the design goals for a trapped electron charge on helium as takeaways from this chapter. Not all of these guidelines were determined before most of the data for this dissertation was collected and may also conflict with design philosophies that make early-stage experiments much more forgiving.

1. The pressing field should be minimized to reduce the coupling strength to ripplons. Above $\sim$300 mV/μm of applied bias for a microwave-frequency electron at a temperature of 10 mK in a typical device geometry, there is no phase coherence of the charge even if Rabi splitting is resolvable.

2. The sensitivity of the electrostatic trap curvature to helium fluctuations should be tunable to an extremum. This is typically possible with at least three approximately independent lever arms which tune the quadratic and non-quadratic moments of the trap curvature and the trap depth. Sensitivities of hundreds of MHz/nm are typical without such an extremum, making for strong coupling to ripplons.

3. Generally speaking, higher electron transition frequencies result in weaker coupling to ripplons. The tradeoff is that traps look more harmonic and the electron lifetime is shorter. Furthermore, if the ultimate goal is to couple to the spin through the charge, higher frequencies necessitate stronger external magnetic fields, which are generally incompatible with planar superconducting resonators.

CHAPTER 4

EXPERIMENT DESIGN

This chapter details the experimental apparatus used to acquire the data presented in this dissertation and the considerations which guided the design of the devices which made the experiments possible. Most experiments in circuit quantum electrodynamics necessitate the use of a dilution refrigerator to facilitate temperatures in the millikelvin range, at which point quantum-mechanical effects set the energy scale of system observables rather than thermal physics [92]. In the case of levitating electrons, the low temperatures also make strongly correlated electron physics possible [16, 25]. A hermetic sample cell houses the devices at the lowest temperature stage of the dilution refrigerator and is filled with liquid helium from room temperature via a capillary tube. A high-stability voltage source connected to well-filtered conducting lines is used to control the sample electrodes to manipulate electrons spatially, while pulse spectroscopy is used to probe the microwave properties of the trapped electrons. Although some of the guiding design principles for samples changed between experiments, this chapter details common strategies for maximizing the coupling to the electrons and designing a sample that aims to alleviate many of the potential challenges associated with performing cQED techniques with electrons on helium. Finally, I detail some valuable techniques for sample diagnostics that made experiments more feasible across many different samples.

4.1 Cryostat and Liquid Helium Filling Setup

Below its lambda point at 2.17 K, liquid helium-4 experiences a phase transition to a superfluid state [93, 94]. At temperatures less than approximately 700 mK, its vapor pressure becomes negligible, establishing an upper limit on the temperature range in which one might optimally explore the physics of few-electron Wigner crystals [5]. Above this temperature,

scattering with helium vapor atoms needs to be considered, depending on which electron state's energy spectrum is being probed [13]. The superfluid experiences a van der Waals attraction to proximal substrates that, up to a certain film thickness, exceeds its gravitational potential energy. In the process of minimizing its own potential energy, the superfluid helium naturally coats its container in a van der Waals layer of approximately 30 nm thickness at saturation [95]. Balancing the van der Waals attraction to the substrate against gravity gives a film thickness $d(h) = (\alpha_{\mathrm{vdW}}/gh)^{1/3}$ at a height h above the bulk liquid, where α_{vdW} characterizes the strength of the van der Waals potential, so the film thins slowly with height [96]. While this guarantees a pristine liquid helium surface everywhere in the sample container, it also introduces some inconveniences for electrons-on-helium experiments in dilution refrigerators.

The introduction of liquid helium necessitates a sample cell that is hermetic at cryogenic temperatures. By the same effects that form the desired superfluid helium surface on the experimental samples, the superfluid will find its way out of a leaky sample container and will climb the cryostat internals (a Rollin film) [95]. As an exceptional thermal conductor, the helium will create thermal shorts between the temperature stages of the refrigerator and rapidly soften the vacuum within the cryostat when it ultimately vaporizes after contact with a hot stage. The experiments detailed in this thesis make use of a superfluid-tight sample cell outfitted with indium-sealed hermetic connectors and a large, primary indium seal that is remade with every sample exchange. In practice, these connectors and seals can bear several bar of pressure before popping, allowing the removal of helium from the cell via thermal cycling without destroying the seals.

Liquid helium is inserted into and removed from the sample cell via a hermetic fill line descending the cryostat from a room-temperature control manifold. The fill line also serves as thermalization for the helium as it descends from room temperature to millikelvin temperatures. The large interfacial Kapitza resistance of the liquid helium [97] encourages the use

of capillary tubing to reduce the thermal load of the liquid helium on the cryostat, though tubing that is too narrow can make evacuation of the sample cell slow and risk damaging the indium seals since the pressure in the cell rapidly increases when the helium vaporizes during evacuation. While the steel fill line thermalizes the helium, it does not thermally short the refrigerator stages since steel is a poor thermal conductor at cryogenic temperatures. Tubing sections coiled around and brazed to copper posts bolted to each stage thermalize the helium and alleviate the thermal load that the helium column itself brings to the lower stages. Before each cooldown, this fill line is thoroughly evacuated to a pressure in the sub-nanobar range, preventing contamination of the sample surface with frozen atmospheric gases. Though not featured in this dissertation, powdered sinter filters could be particularly effective at thermalizing the helium at colder stages since their large surface area pairs well with the van der Waals properties of superfluid helium [92].

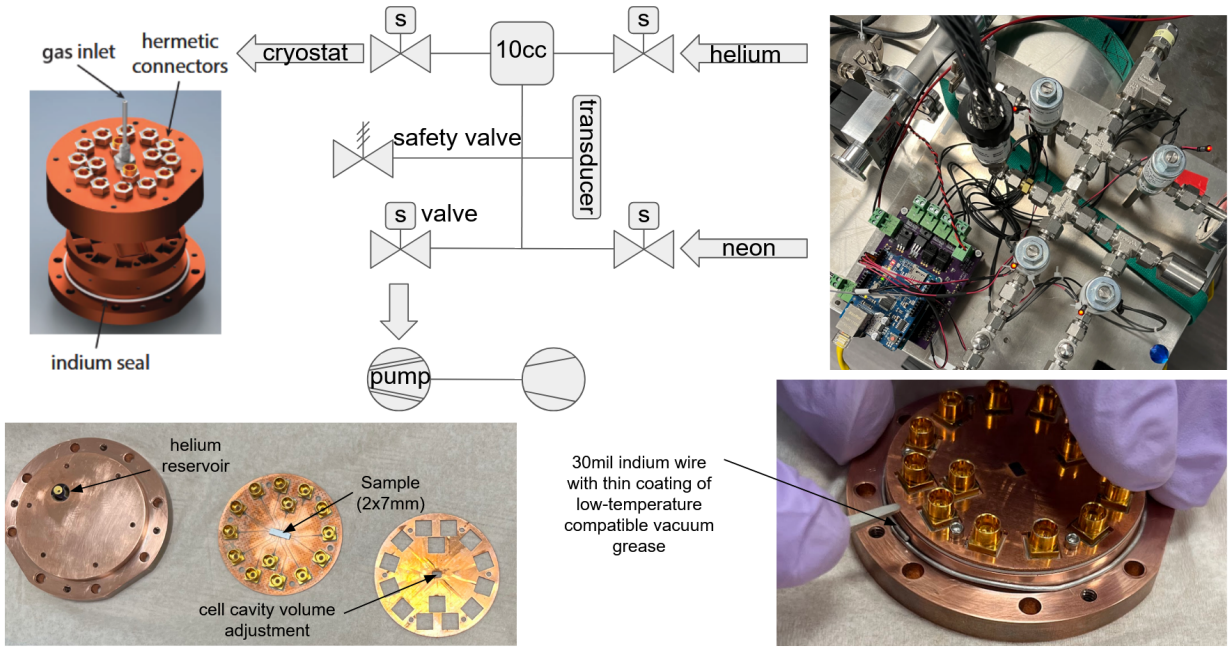


Figure 4.1: Helium filling apparatus

The electron trapping device is housed in a hermetic sample cell at the base stage of a dilution refrigerator, reaching temperatures below 20 mK. The sample cell and the hermetic connectors are assembled with indium wire seals to contain the superfluid helium. There is a < 1 cm^3 dead volume drilled into the base pedestal of the cell holding the reservoir that the superfluid naturally finds its way to. A stainless steel tube thermally anchored by brazing to copper cylinders at each stage of the dilution refrigerator gradually thermalizes the room-temperature helium. An electronically controlled gas manifold at room temperature negotiates gas insertion into the tube. Sample cell schematic adapted from [98, 99].

4.2 RF Spectroscopy and DC Bias Setup

One of the advantages of circuit quantum electrodynamics that has contributed to its rise over the past few decades as both a toolbox for exploration of novel physics and a foundational platform for the creation of a quantum computer is the ability to reach exceptional signal-to-noise ratios (SNR) with rapid throughput. This is particularly true in comparison to the DC measurement techniques often used to study electrons in semiconductor systems. Reaching an SNR of unity within tens of nanoseconds is routine in cQED experiments through the use of microwave quantum-limited amplifiers, while in other hybrid quantum information platforms the time is often orders of magnitude longer [100, 101]. In addition, dispersive

readout techniques allow for non-destructive readout of coherent few-electron states. While the inability to make ohmic contact to the levitating two-dimensional electron gas (2DEG) makes readout more challenging than in most semiconductor systems, recent experiments have made significant strides in detection of levitating electrons in lower-frequency regimes, potentially paving the way for combining the toolbox developed through decades of semiconductor systems measurements with the cQED techniques used in most experiments with single electrons on helium [40, 41].

The experiments in this dissertation were primarily performed through single-tone spectroscopy of microwave resonators. A microwave pulse is delivered to the sample while the transmission amplitude through a second transmission line is monitored, with transmission function

$$S_{21}(\omega) = \frac{\sqrt{\kappa_1 \kappa_2}}{(\kappa_1 + \kappa_2 + \kappa_i)/2 - i(\omega - \omega_r)},$$

where ω_r is the resonator frequency, κ_1 and κ_2 are the coupling rates to the input and output lines, and κ_i is the resonator's internal loss rate. The signal is divided into two quadratures, affording sensitivity to both the relative amplitudes and phases of the input and output signals. A Lorentzian lineshape can be fit to the quadrature for a precise characterization of the resonator frequency, easily down to one percent of the linewidth or better (Fig. 4.3). Parasitic capacitance between the transmission lines coupling to the resonator can produce an asymmetric spectral line. Driving too strongly, especially for high-impedance microwave resonators, eventually leads to bifurcation of the Lorentzian spectral line, placing an upper bound on trading lower averaging for higher input power. The input drive strength, external coupling to the resonator, and resonator's internal losses determine the mean intracavity photon number in steady state. Resonator internal quality factors in these experiments ranged from approximately 10^3 to 10^5, with higher resonator impedance and more fabrication steps generally resulting in less coherent cavities. Going from one fabrication step to five

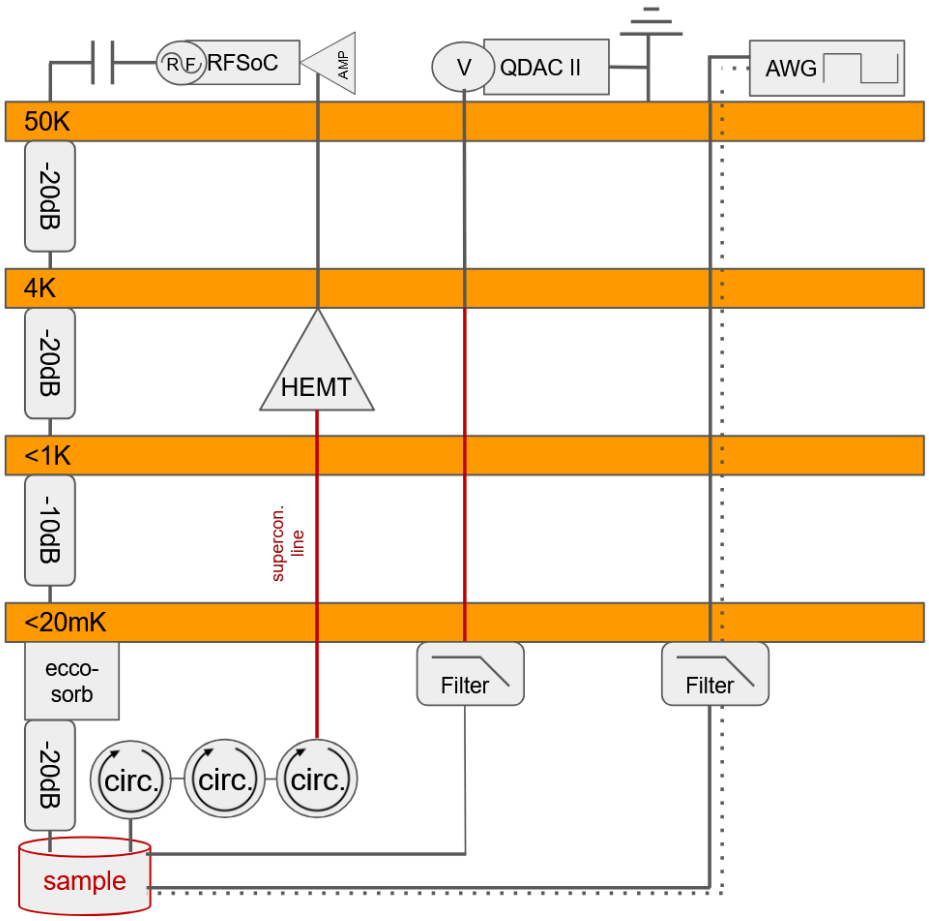


Figure 4.2: Spectroscopy and bias equipment
Spectroscopy experiments are performed with an RFSoC, a circuit board integrating FPGA-based programmable logic and control with on-chip data converters. The spectroscopy input line is attenuated at each thermal stage to reduce the sample's incident noise temperature. Immediately before the sample, an epoxy-based filter attenuates high-frequency noise. Circulators introduce chirality which isolates the output signal without introducing the loss associated with attenuators. The signal is amplified by a low-noise amplifier anchored to the 3 K stage and further amplified at room temperature immediately after exiting the cryostat. Spectroscopy timing is synced to a high-stability voltage source which provides the bias for the device electrodes. The bias lines pass through a resistive filter at base temperature and are weakly thermally anchored at each stage. An arbitrary waveform generator that is more weakly filtered produces pulses for heating the tungsten filament in the sample cell for electron emission.

could decrease the quality factor by one to two orders of magnitude, and a sharp drop in internal quality factor was routinely observed for resonators with pin widths less than approximately 500 nm. Near the resonant limit between the cavity and an electron, a mean

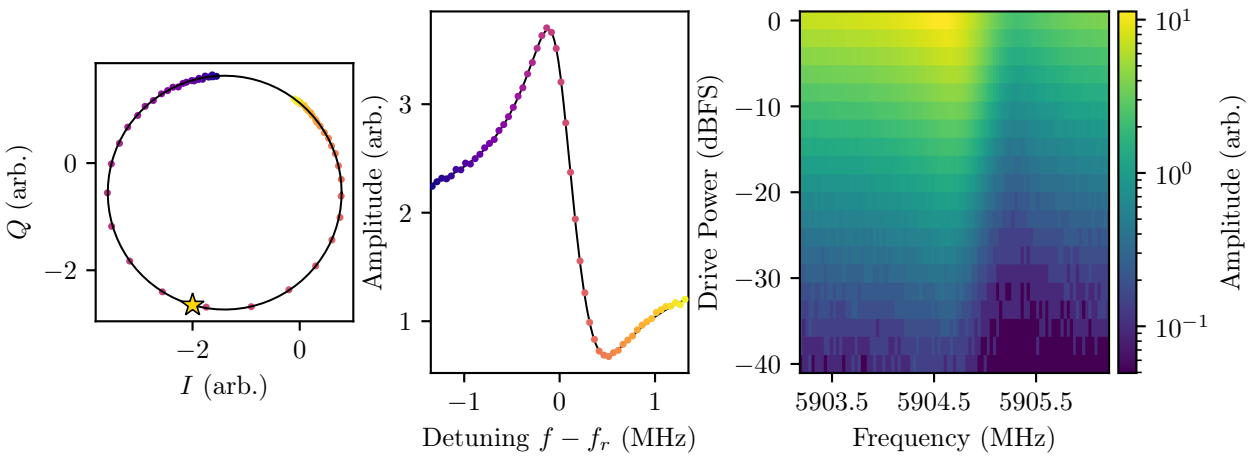


Figure 4.3: Single-tone spectroscopy of a readout resonator
The Lorentzian spectral line of a microwave resonator can be fit to a circle in IQ or phase space, with I being the in-phase component of the response and Q being the quadrature. Combined with the magnitude of the frequency-dependent response, the fit and its error determine the resonance frequency and quality factor or total loss of the resonator. While superconducting resonators are typically harmonic, they can exhibit input-power-dependent responses when there is significant kinetic inductance or when coupled to a nonlinear system.

intracavity photon number significantly larger than one can blur the avoided crossing, so it can be beneficial to drive weakly but average more. Attenuating the input signal at progressively colder temperatures also reduces the input noise temperature to the system. Cryogenic circulators at the sample stage act as isolators, preventing noise from the output side of the line from reaching the sample. Epoxy-based absorptive filters with frequency-dependent performance are also utilized near the sample. At such low signal intensities, the noise temperature of the output signal determines the required averaging time. The output noise temperature is dominated by the noise temperature of the first amplifier in the output chain [102]. In these experiments, that amplifier generally has a noise temperature of approximately 2 K, which introduces approximately 10 photons of thermal noise, whereas a quantum-limited amplifier typically features a noise temperature of 200 mK, reaching the half-quantum noise limit imposed by the uncertainty principle.

Spatial control of the electrons is achieved with heavily filtered DC electrodes submerged in the liquid helium. Since the properties of the electron orbital state transitions are primarily

set by the trapping potentials, careful filtering of the electrode bias lines is necessary to prevent introducing additional noise to the system. In these experiments, the DC biases are provided by a high-stability voltage source at room temperature and filtered through a copper-powder and epoxy filter box that is bolted to the sample stage. On-chip low-pass filters are positioned as launchers for wirebonds to the sample surface from the sample PCB transmission lines [103]. Cascaded low-pass filters with different cutoff frequencies can suppress pass bands from any individual filter [104]. Since the capacitive coupling constant of the trapped electrons to the readout microwave resonator is similar to that of the nearby electrodes, these filters prevent leakage of photons from the electron and cavity system through the DC lines. Similarly, they prevent the introduction of high-temperature noise from the room-temperature bias source without attenuation of the applied voltage. The differential mode of a coplanar stripline resonator allows for voltage biasing of the resonator itself as well since only common modes leak through the voltage tap. The experimental tradeoff for aggressive DC filtering is a longer time constant over which voltage changes at room temperature are realized at the sample.

While the binding of the electron to the helium surface allows this levitating-particle system to circumvent Earnshaw's theorem and utilize electrostatic fields for electron trapping rather than RF potentials as in trapped-ion systems [11], the energy scale of the electron motional states forces some additional considerations of electrode properties. The length scale of the electrodes should be harmonious with the distance to the electrons above the helium since the screening of the inter-electron potential is primarily set by the distance to the substrate and submerged electrodes beneath the electrons. Otherwise, spatial control of single electrons becomes more challenging. In these experiments, the depth of the microchannels over which the electrons are suspended typically ranges from hundreds of nanometers to roughly one micron, so the electrode widths and spacing are similar. Likewise, experiments with electrons over van der Waals films would suggest an optimal electrode length scale of

roughly 30 nm. Single-electron orbital transition energies at typical cQED frequencies correspond to tens of μeV. Roughness of the trapping electrodes introduces unintended spatial variation of the trapping potentials that is Poisson-smoothed with increasing distance from the electrodes and can cause spatial "pinning" of electrons. Deposition techniques that result in smoother surfaces, such as atomic layer deposition, are therefore well suited to the fabrication of electron trapping devices [105]. Similarly, the electrode surfaces can be sensitive to the particulars of any reactive-ion etching processes used in device fabrication [106]. Recent advances in the reverse, atomic layer etching, show promise in smoothing surfaces and potentially reducing the density of native TLS embedded in the electrode and substrate surfaces [107]. Other experiments have demonstrated the use of smooth, amorphous metals to retain high electron mobility even on van der Waals thin films of helium [82, 108].

During measurements, electrode biases are ramped smoothly and synchronized to the internal clock of the microwave source. Levitating electron systems are generally very hysteretic, so the system state is constantly tied to the measurement path. In addition, the trapping potential felt by the electrons can change over time due to stray electrons, helium surface vibrations, or other such instabilities. Compared with most semiconductor quantum dot systems, electron-on-helium orbital states have wavefunction aspect ratios in two dimensions closer to unity, and the electron interactions are long-range, sometimes making tomography of these correlated electron states slow [25, 109]. The DC lever arms are also generically not orthogonal, and unintended asymmetries can significantly narrow the window of system sensitivity. In practice, an experiment with electrons on helium involves optimizing the input drive strength and electrode bias path to collect maximal information before instabilities cause the system to reconfigure while identifying cases of unintended introduction of system hysteresis.

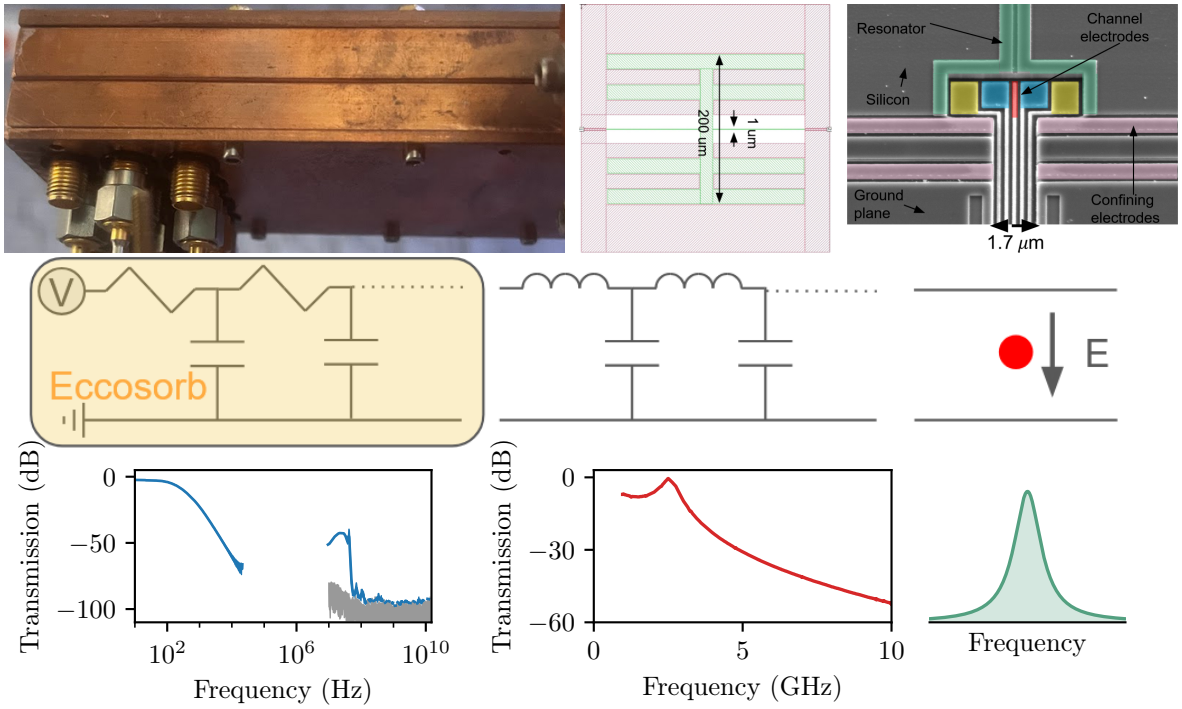


Figure 4.4: DC filtering approach
Weak thermal anchoring to each cryostat temperature stage and a strong resistive filter at base temperature thermalize the bias line. This is critical to minimizing the effective electronic temperature of the electrodes on the sample. On the sample, superconducting reactive filters further protect against signal leakage through the electrodes, some of which are nearly as capacitively coupled to the trapped electron as the readout resonator. The resistive filter is often filled with epoxy, potentially mixed with copper or silver powder, to further reduce the effective temperature and protect against higher-frequency radiation. Top row, left to right: filter box, a model of an on-chip low-pass filter (Filter 4 in Appendix B), and an SEM image of the electron dot of device 3 in Appendix B. Bottom row: measured transmission through cascaded bias-line filters (blue) above the noise floor of the measurement (grey), digitized from Ref. [98], which used the same filter box, the simulated transmission through the on-chip reactive filter, and a Lorentzian spectral line of a resonator.

4.3 Devices for Trapping Single Electrons

In these experiments, electrons are detected via the dispersive shift of a superconducting resonator's frequency from an electric dipole interaction with the orbital states of the levitated electrons [29, 79]. The electric dipole moment of a microwave-frequency electron orbital state is sizable, only one or two orders of magnitude less than that of a typical capacitively coupled transmon qubit and orders of magnitude larger than optical atomic transition dipole

moments. The comparable transition and interaction energy scales make them well suited for integration into cQED systems. However, unlike with a transmon qubit, one cannot arbitrarily increase the coupling strength of the resonator to the electron by bringing the electron closer. The electron's properties are sensitive to its geometric position above the device electrodes beyond just a scalar value. Therefore, an electron trapping device should be designed to maximize the coupling strength to the electrons without bringing the geometric sensitivity into an inconvenient regime.

The most promising tactic for maximizing the coupling without geometric considerations is to utilize high-impedance resonators [110]. With increasing impedance, the zero-point voltage fluctuations of the resonator increase as $\sqrt{Z}$, increasing the coupling electric field. The most straightforward method to fabricate such resonators is to introduce kinetic inductance to the resonator material. When the London penetration depth of a superconducting film becomes larger than its thickness, the inertial mass of its charge carriers, which are no longer confined to a small surface on the exterior of the film, introduces a contribution to the per-length inductance that far exceeds the geometric inductance. At low temperatures, a film with normal-state sheet resistance $R_\square$ and superconducting gap Δ_0 has a kinetic inductance per square of $L_{k,\square} = \hbar R_\square/(\pi\Delta_0)$, so thin, disordered films with high sheet resistance have the largest kinetic inductance. While geometric optimization can bring the impedance of a microwave superconducting resonator from 50 Ω to perhaps several hundred ohms, introducing a sizable kinetic inductance to the resonator material makes resonators with impedances in the tens of kΩ range feasible. Thin-film disordered superconductors in the nitride family, such as TiN, NbN, and NbTiN, are particularly well studied as materials for superconducting microwave resonators [84, 105, 111–113]. These materials can be easily grown via atomic layer deposition and sputtering, and, in the former case, can have sub-nanometer surface roughness, making them particularly suitable for electrons-on-helium experiments. Granular aluminum, though not suitable for these experiments due to its typi-

cal roughness, has also gained significant interest as a high-kinetic-inductance material [114]. NbN, with its magnetic field resilience, could also be of interest in future electrons-on-helium studies involving the spin state of the electrons [115].

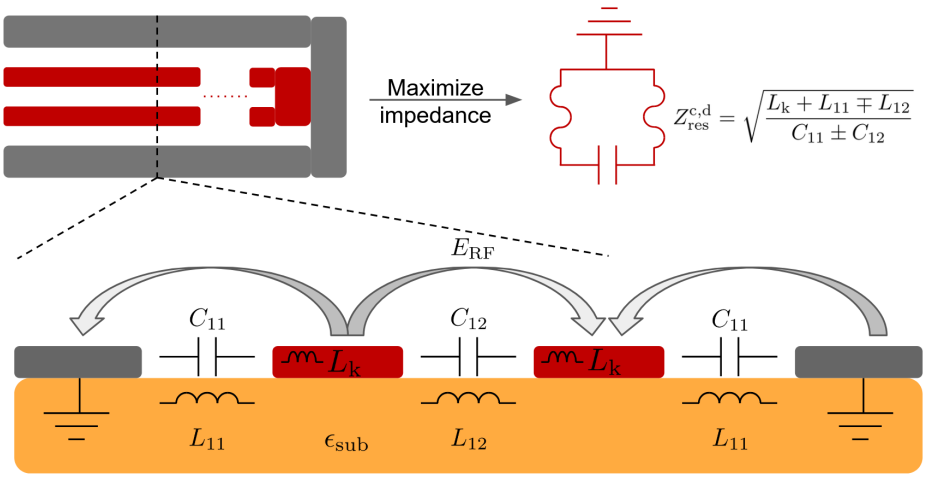


Figure 4.5: Optimal resonator for coupling to an electron
A coplanar stripline resonator's differential mode is protected against leakage through a symmetric voltage tap and exhibits a microwave electric field maximum between its two pins, making it ideal for coupling to an electron in a nearly symmetric potential. The capacitive and inductive coupling matrix elements of the resonator geometry can be used to calculate its frequency to good accuracy. Introducing kinetic inductance to the resonator increases its impedance, which is desirable for stronger electric dipole interactions, and reduces its size. Splitting the two arms of the resonator so that they no longer run adjacent to one another and compacting them into 'wiggles' further increases the impedance.

Since it is not feasible to locally generate only a few electrons via thermionic emission, it is necessary to also manipulate an electron reservoir from which single electrons can be loaded into and unloaded from the traps [79]. Historically, large areal electron densities and high mobilities have been routinely achieved on superfluid helium with microchannel geometries [80]. Capillary effects cause the helium film to snap into tension-stabilized, channel-filling configurations whose curvature can be estimated from the parameters of the microchannel and the amount and location of superfluid helium in the sample cell. The filling of these microchannels can be tuned precisely by monitoring the capacitance of electrodes on the sample surface, which changes predictably as the liquid helium replaces vacuum locally when the sample cell

is filled. In particular, in the experiments described in this manuscript, the helium level is monitored by observing the frequency shift of a superconducting resonator as the modal volume of the resonator electric field is filled with helium [79]. The sensitivity of this method is greatest when the liquid helium thickness is on the order of the length scale of the electrode or resonator transverse dimensions, and while it quickly decreases outside of it, the SNR remains exquisite, so the filling can in principle be monitored over several decades of thickness.

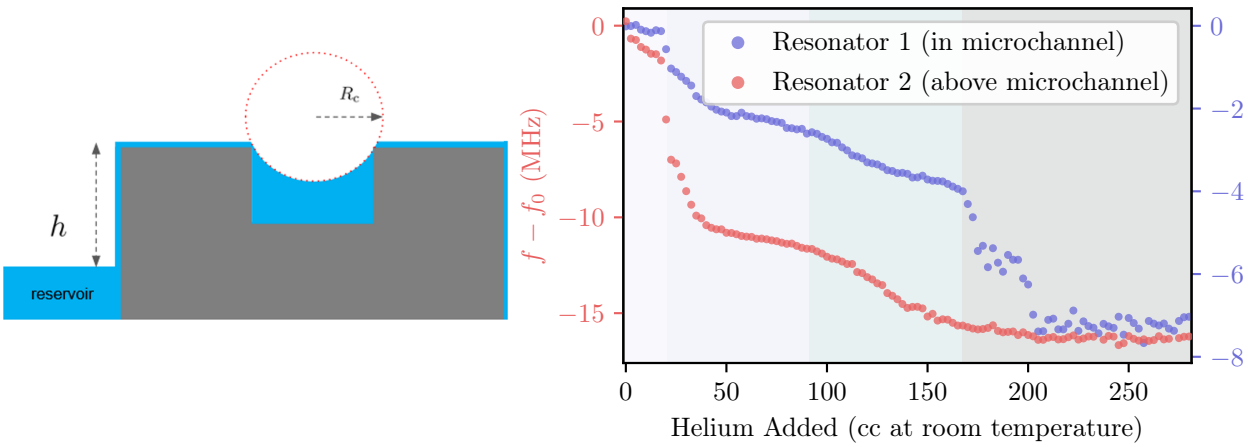


Figure 4.6: Helium capillary action in microchannels
Superfluid helium creeps on all the surfaces of its container and naturally finds the lowest level in the cell when gravity is present. Capillary action causes microchannels to fill with helium even when the helium reservoir is far below the device surface. Typically, for micron-sized channels, the channel already fills rapidly when the helium bath level is millimeters below the sample surface. Small microchannels stabilize the helium surface from the long-wavelength, low-frequency oscillations produced by the pulse tube of the dilution refrigerator, but are still far too wide to have a noticeable effect on ripplons interacting with electron orbital states. The capacitance of a planar resonator is sensitive to the average dielectric constant in its vicinity. When vacuum is replaced with helium, the resonator frequency therefore shifts downward. Different geometries and placements relative to the microchannel or device surface exhibit different helium filling curves. This data was taken with a device similar to device 1 in Appendix B.

The electron reservoir density can be estimated from the voltage-space and microwave properties of the trapped electron ensemble. A trapped electron ensemble has a collective dipole moment scaling with the number of electrons as $\sqrt{N}$, so at typical surface electron

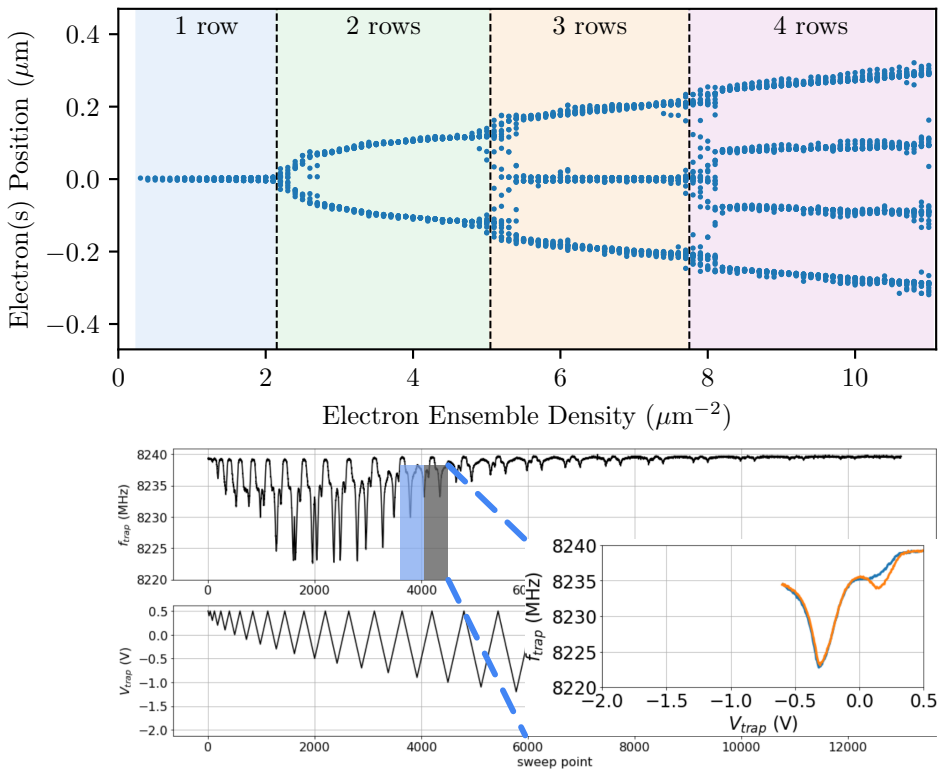


Figure 4.7: Electron ensemble response: resonator
Electron ensembles in microchannel geometries can reach densities of 10^9 cm^{-2}. Because of the high lateral-to-longitudinal planar dimension aspect ratio, the electrons arrange themselves in a triangular lattice structure, forming discrete rows in the transverse direction. The density and configuration determine the ensemble average electrostatic energy or its 'chemical potential', which factors into trap design for single-electron isolation. It is possible to permanently reduce the ensemble density by reducing the electrostatic trap depth until some of the ensemble escapes, seen as voltage sweep-direction hysteresis in the resonator response (orange and blue traces, bottom figure) [79]. We can progressively thin the electron reservoir to a density more appropriate for experiments or even until no ensemble remains and the resonator voltage sensitivity and hysteresis disappear. This data was taken with a device similar to device 2 in Appendix B.

densities, even without leveraging high-impedance resonators, the response of the resonator to the electron ensemble is pronounced [79]. Furthermore, as the electron ensemble minimizes its energy by arranging into a periodic lattice, the motional modes and coupling strength to the resonator of an ensemble of a known density in a specific trapping potential can be numerically calculated. Recent experiments have probed the lower-frequency plasmon modes of these electron ensembles, demonstrating that there is rich physics to be observed even when

not working in the few-electron regime [40]. The density of the ensemble can be estimated by treating the electrons as a sheet of charge and finding the trapping potential depth at which the electrons begin to escape to the nearby ground plane because the mean lateral inter-electron electrostatic potential exceeds the electrode-induced potential. Generally, this value is found in electron-on-helium experiments by monitoring the response of the resonator frequency to electrode voltages for hysteresis as the electron trap is made shallower. Otherwise, the first technique used to detect electron densities on helium, the Sommer–Tanner method, remains effective without needing to reach millikelvin temperatures for superconducting resonators [13]. In this case, the driven capacitance between two electrodes is monitored as a

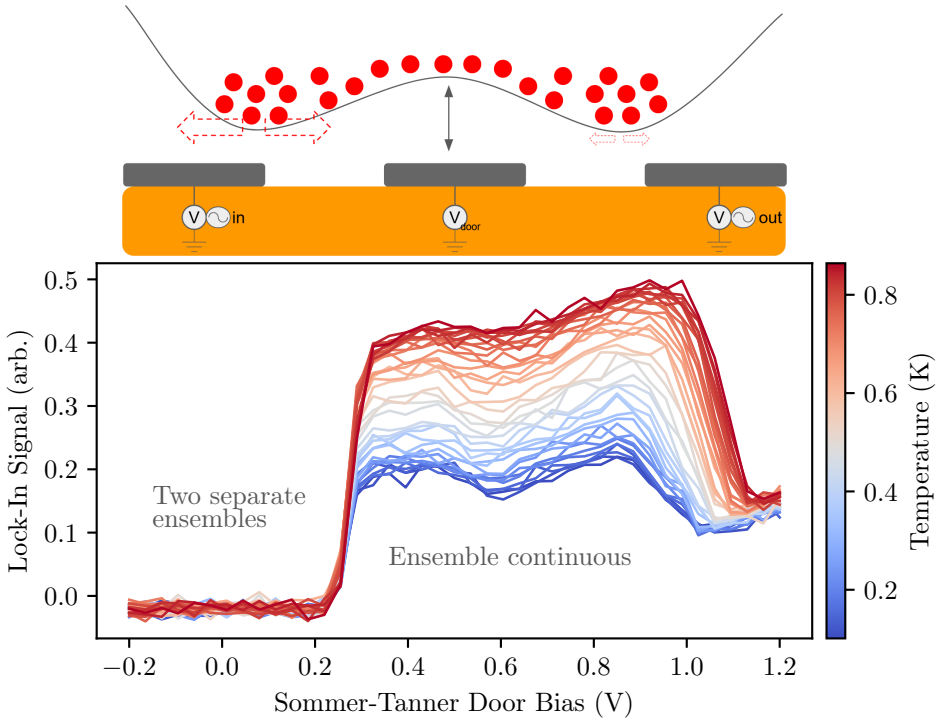


Figure 4.8: Electron ensemble response: Sommer–Tanner
In a Sommer–Tanner type measurement of an electron ensemble, a low-frequency AC voltage is applied to one electrode and the current response in another is monitored while an intermediate electrode's bias is varied. When the middle electrode no longer divides the ensembles above the other two electrodes, the measured current increases, allowing estimation of the ensemble mobility and density without making ohmic contact to the electron ensemble. This data was taken with a device similar to device 4 in Appendix B.

function of the bias of a central electrode. As an electrostatic barrier is raised and lowered

between two electron sheets, a voltage modulation on one electrode produces a notable signal on the other side only when the electron sheets are connected, allowing for precise determination of the ensemble density and mobility, though no information about the motional modes can be obtained in this way.

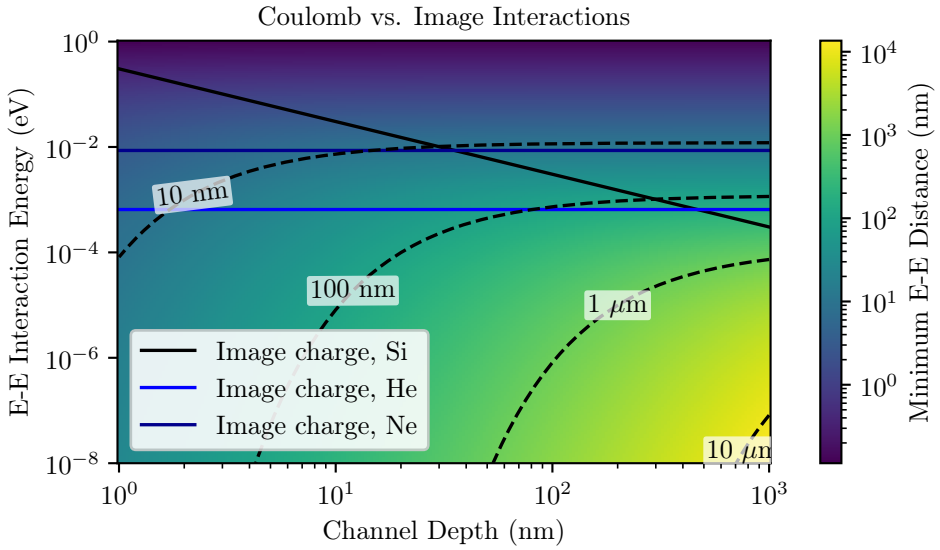


Figure 4.9: Channel depth and inter-electron interactions
Above a conductor such as an electrode or a higher-dielectric-constant substrate, the inter-electron Coulomb interaction is screened by their image charges. Their Coulomb interaction falls off exponentially with the channel depth d as a Yukawa potential with decay constant $-2d$. This motivates microchannels at least several hundred nanometers deep so that the inter-electron interactions at their typical spacing of 100–200 nm exceed the image-charge interaction energy.

The electrons in these experiments are sourced via thermionic emission from a tungsten filament positioned above the sample surface. Tungsten has the highest melting point of all known metallic elements at nearly 3700 K, so a relatively large current can be applied to a small-gauge tungsten wire in the sample cell without melting the wire. Of course, this current must be applied in pulsed duty cycles on the order of tens to hundreds of kilohertz since the mixing chamber of the dilution refrigerator is at millikelvin temperatures when the filament is flashed to generate electrons. In the case of helium, the vapor pressure increases significantly when the electrons are emitted, which scatters and slows the emitted electrons

such that some fraction of them come to rest on the helium surface rather than punching through it and forming electron bubbles or finding a conductor. In practice, the mixing chamber temperature may momentarily reach up to a few hundred millikelvin due to the vapor quickly thermalizing the cell. Aggressive momentary heating of the sample and higher-energy electrons may cause TLS reconfigurations on the sample surface and charging of the device. Another major disadvantage of this method is that it is generally stochastic. Recent experiments have also featured photoemission from various materials as a suitable electron source.

4.4 Finite Element Modeling and Device Design Philosophy

The devices detailed in this dissertation were simulated using commercial finite element modeling software (Ansys Maxwell and HFSS) to explore the electron trapping parameters and the properties of the on-chip microwave components. While different devices were designed with different strategies in mind for probing the electron states, the discussion in this section is framed around one particular device featured in this dissertation, its design process, and design elements that were, in retrospect, particularly useful or instead ill-chosen across multiple devices. The electrostatic potential in three dimensions of each electrode is simulated while all other conductors are grounded. By linearizing the electrode simulations, the electron trapping potential for a given device voltage configuration can be predicted. In the region intended for single-electron confinement, the solution is meshed with a maximum tetrahedral element length smaller than the electron zero-point fluctuations to guarantee that the solved potential is smooth from the perspective of the simulated orbital states. This is critical since most of the energy in the simulated system is in the high-dielectric substrate, which matters little to the electron but allows for the simulation to converge prematurely.

The experimental space for electrons on helium is rich, both from the perspective of quantum information and also condensed matter systems in general, but accessing this space requires an appropriate set of levers on the electron properties. For a single electron oscillator trapped on liquid helium, the immediately useful system parameters are the first transition frequency, anharmonicity, and the classical sensitivity of the transitions to the helium level and the planar position of the electron. A reasonable postulate is that for three independent parameters, three independently controllable parameters of the electrostatic trap are needed: the quadratic and quartic moments of the trap curvature and its depth. By changing the quartic and quadratic terms of the potential, the electron frequency and anharmonicity can be adjusted. The trap depth can be roughly mapped to a sensitivity to the helium level, which is useful since vibrational displacement of the helium surface can lead to dephasing of the

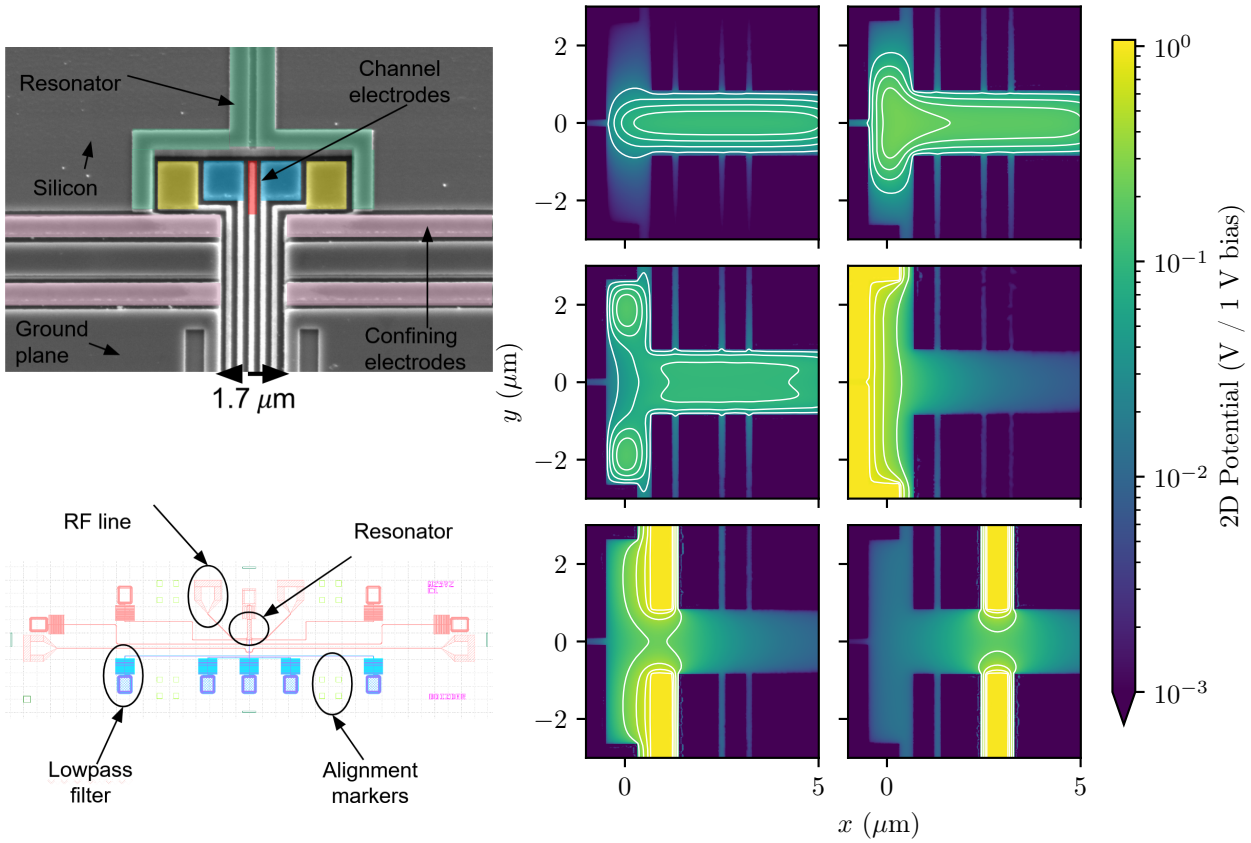


Figure 4.10: Typical electron trap design
While many devices were used to produce the results discussed in this dissertation, some performing better than others, one of the last is depicted here to illustrate the general design principles of an electron trap. In this case, three symmetric sets of electrodes within the microchannel shape the trap curvature with the central electrode typically being biased less positively than the others to 'flatten' the potential to low enough frequencies. Three sets of planar electrodes, including a voltage-tapped superconducting coplanar split-pin resonator, are used to confine electron clusters away from the larger ensemble.

orbital state. This is somewhat straightforward when considering the boundary conditions of the orbital state with respect to its height above a single electrode; if the electron is very close, its oscillatory frequency should be small, and since the same is true for an electron far from the electrode, there is intuitively a 'sweet spot' where the electron frequency is insensitive to vertical displacements.

As of yet, single-electron orbital decoherence remains particularly large, so designing a resonator that maximizes the coupling to the electron is particularly useful in exploring the

system. A coplanar stripline resonator geometry maximizes the coupling to the electron between the center pins, and the coupling strength is first-order insensitive to the transverse electron position. By utilizing a high-kinetic-inductance TiN thin film and minimizing the self-capacitance and capacitance to ground of the resonator by drastically splitting the pins, it is possible to raise the resonator impedance to several kΩ. Since the electron linewidth can be large, it is useful to overcouple to the resonator so that the SNR of the resonator measurement remains nearly constant when the orbital state and resonator are significantly hybridized. It is also helpful to engineer a resonator linewidth slightly broader than the expected dispersive shift due to a far-off resonant electron so that exploring the voltage space of a device is manageable by measuring only a single frequency point.

Detecting single electrons is made more challenging in these experiments by unintended charge states in the modal volume of the resonator, particularly device surface TLS and electrons levitating on the ground plane or resonator [116, 117]. The latter can, to an extent, be removed from the device surface by alternating between 2 and 4 V of positive and negative bias on the resonator, causing some electrons to be ejected to the ground plane and others to be sucked into the helium. If not 'cleaned' away, these stray electrons can perturb the single-electron trapping potential, cause inconsistent dispersive shifts of the resonator frequency, or degrade its quality factor. In the case of surface TLS, it is necessary to assess the scale of the typical TLS density and coupling strength to the resonator before introducing electrons to the device. This aids in differentiating off-resonant levitating single electrons from TLS. The split-pin resonator design makes removing electrons from the resonator more difficult since the modal volume is larger and the electric fields along the body of the resonator are generally weaker, while for the same reasons the sensitivity to TLS is less than that of a conventional coplanar stripline resonator.

CHAPTER 5

SINGLE-ELECTRON ISOLATION

Single electrons on superfluid helium were first isolated in electrostatic traps using a local single-electron transistor (SET) in a microchannel [24]. Unlike in semiconductors, there cannot be ohmic contact between a two-dimensional electron gas on liquid helium and the device, making counting electrons using only their individual capacitances to an electrode challenging. It is therefore not surprising that most experiments since the first counting with an SET have also utilized techniques from superconducting circuits, where the electron signal can be enhanced by level repulsion between the electrons and a superconducting resonator [28, 29]. Optimizing this signal while reducing sensitivity to background sources remains a challenge in the field, reflected by the fact that even today there exist only a handful of devices in the world that can reliably and deliberately isolate single electrons on superfluid helium. This section details the isolation of single electrons with such devices, common challenges faced when doing so, and the implications of typical spectroscopy signals.

5.1 Electron Counting

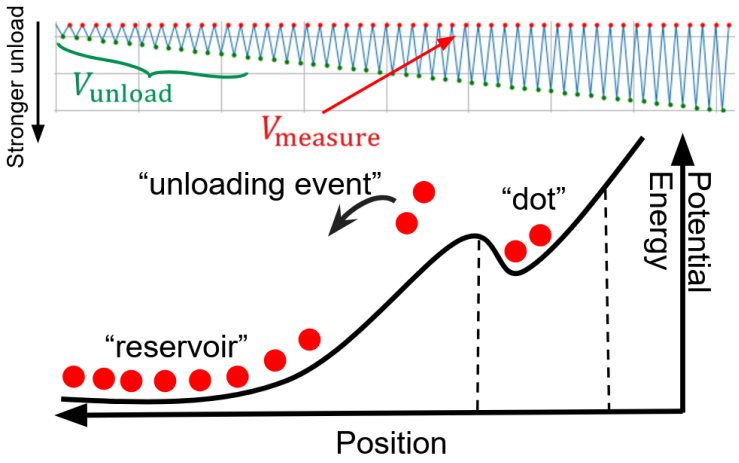


Figure 5.1: Electron unloading

It goes without saying that the first step in measuring single electrons is isolating them from our electron reservoir. In the case of electrons on helium, hysteresis is the defining characteristic of calibration experiments. Because of the length scales set by the helium microchannels, capacitive coupling constants to the electron are relatively weak, so, unlike in quantum dots, it is difficult to engineer a Coulomb blockade such that only a single electron is allowed into a trap. Instead, we gradually reduce the depth of the trap until it is exceeded by the average inter-electron energy and an electron is released back into the reservoir, removing electrons one at a time [29]. For separation between an electron and

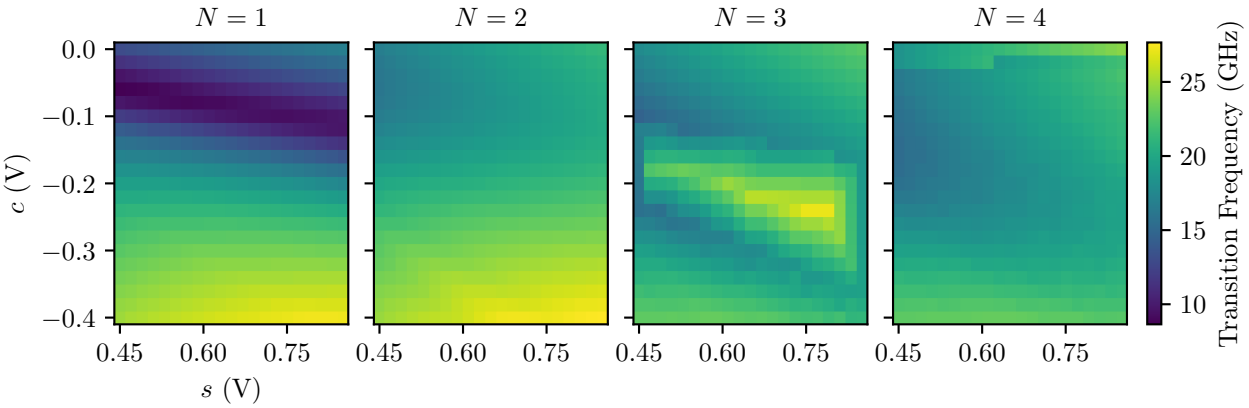


Figure 5.2: Simulation of multi-electron motion
In a two-dimensional potential, each electron's individual equations of motion can be solved with the known trap curvature and the Coulomb interaction energy from the other electrons at their equilibrium positions. Converting the local motional frequencies to effective curvatures, it is possible to solve the cluster equations of motion. This is a more robust approach than taking two spatial derivatives of the simulated electrostatic trap, which requires an exceedingly high mesh density and convergence. Different numbers of electrons have different lowest-lying transitions for the same applied electrode biases.

the detecting resonator on the order of a micron, the capacitance change induced in the latter by the former is approximately an attofarad, 10^5 times less than the typical total capacitance of a superconducting resonator [110]. Since detection of the electron presence by observing a frequency shift caused by the change in capacitance is challenging, it is more straightforward to bring an electron cluster near resonance with the cavity, which can easily shift the frequency by a linewidth. The motional eigenmodes of an electron

cluster change discretely when an electron is removed due to a change in the number of degrees of freedom, which can be observed as 'stepping' in the resonator lineshape when processed along an appropriate vector of electrode biases. Many clusters have metastable electron configurations, so there can be multiple representative signals for identical trap reductions [118].

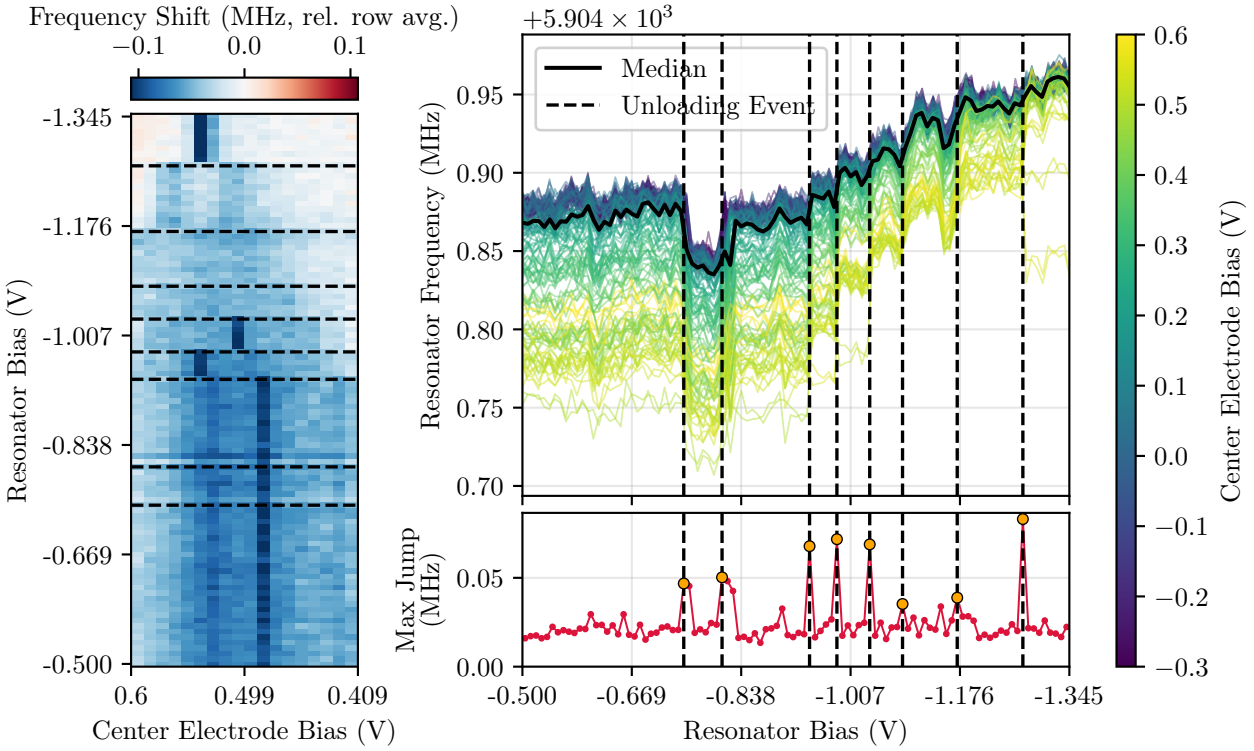


Figure 5.3: Single-electron counting
In this device, the resonator bias is made progressively more negative to push electrons out of the trap. At each 'unloading' step, the other electrodes are ramped to a measurement configuration that brings the orbital transitions closer to the resonator frequency and an electrode to which the trap curvature is particularly sensitive is swept while maintaining isolation from the electron reservoir. Since discrete electron numbers feature distinct motional eigenmode profiles for a given trap curvature, hysteresis is observed in the unloading procedure, corresponding to a single electron exiting the trap. This data was acquired with device 3 in Appendix B.

However, this signal is typically only visible for fewer than ∼10 electrons since above this number, lower-frequency eigenmodes muddle the signal and the change in average inter-electron energy needed to eject an individual electron becomes prohibitively small [118]. Re-

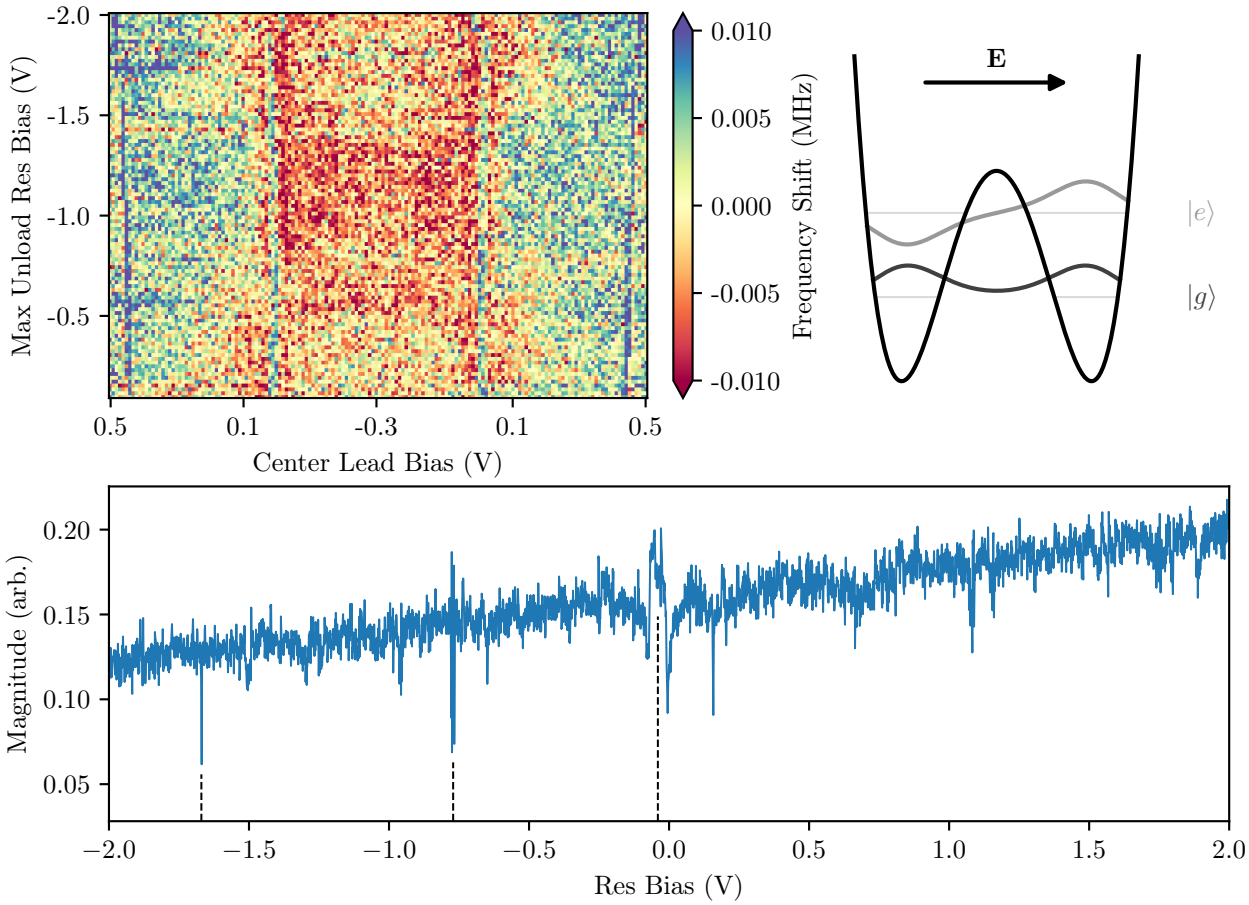


Figure 5.4: Native TLS signal in two dimensions
High-impedance resonators are particularly sensitive to native two-level systems (TLS) because they have relatively large electric field volumes and magnitudes. TLS are typically modeled as one-dimensional systems dominated by charge tunneling. They exhibit a parabolic frequency trajectory with external electric fields, with the frequency minima corresponding to a symmetric, rather than tilted, double well, with typical dipole moments of $\sim 1\ e\,$Å. Here, two TLS are visible in an electron unloading experiment that starts with no electrons in the trap, and the resonator dispersive shift is an order of magnitude smaller than for floating electrons. The typical observable TLS spatial density on our devices is $\sim 1\ \mu\text{m}^{-3}$ when tuning the resonator frequency over ≈100 kHz through helium redistribution. They are useful for verifying working device electrodes at the start of an experiment. This data was acquired with device 3 in Appendix B.

cent research has focused on integrating these plasmon modes with acoustic wave excitation of the helium surface [39, 40]. Competing signals can appear from nearby voltage-tunable TLS and nearby free-floating electrons, which are orders of magnitude weaker when the clusters are near resonance owing to their dipole moments being much weaker than those of

trapped electrons [117]. If it is difficult to bring the electron cluster into resonance, however, these signals can prove deceiving. Ironically, for many in the field, developing this process has proven more challenging than the actual study of trapped single electrons.

5.2 Spectral Signatures of Electron Clusters

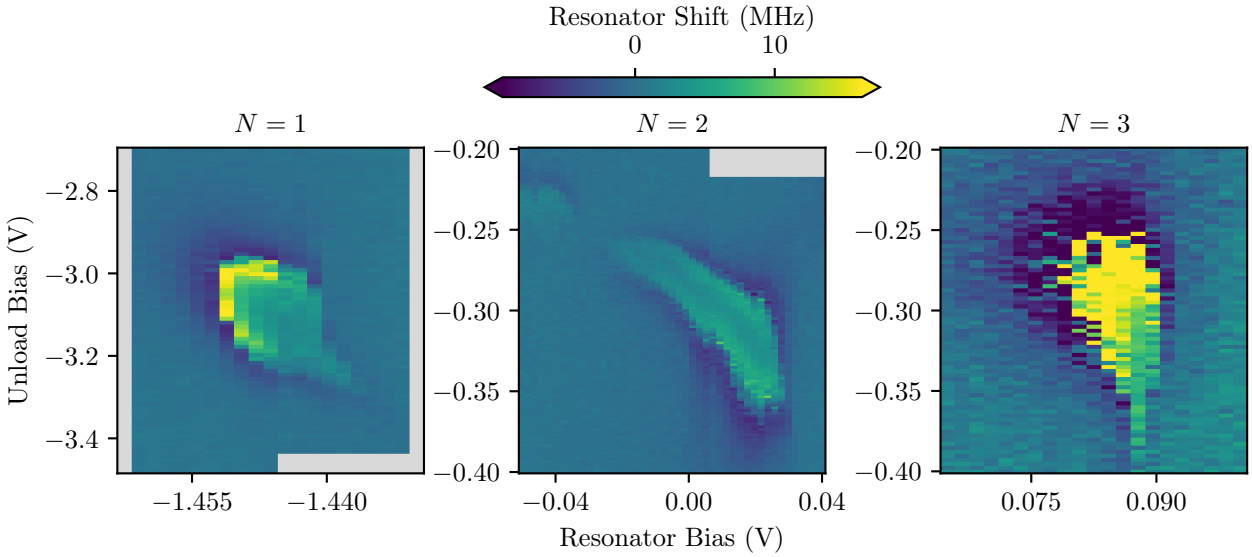


Figure 5.5: Two-dimensional profiles of multiple electrons in experiment
One, two, and three electrons were tuned through resonance with a resonator. The data density was limited by stability over time of the charge diagram. The four-electron response drifted quickly enough that it was not possible to acquire such a 'blob'. This data was acquired with device 4 in Appendix B.

Once isolated, the rich, two-dimensional nature of these trapped electrons becomes clear. Mapping out the response of multi-electron clusters coupled to a superconducting resonator in two voltage dimensions reveals a signal distinct from closer to one-dimensional systems such as junction-based qubits, quantum dots, or even TLS. Due to local asymmetries and other device-native electrostatic potential contributions, there is a finite range of linear combinations of electrode biases that can bring a vibrational eigenmode of the electron cluster to a particular frequency. Surprisingly, electron decoherence mechanisms also appear sensitive to the exact shape of the electrostatic trap and are not equivalent for two otherwise qual-

itatively similar electron first transition frequency trajectories. Eigenmodes of clusters of different numbers of electrons even display different sensitivities to the fixed parameters and asymmetries which limit the response in two dimensions relative to a simpler one-dimensional model. As in the one-electron case, clusters also exhibit configuration-sensitive decoherence mechanisms. While beyond the scope of this dissertation, future work studying the decoherence mechanisms of electron clusters will be valuable to the development of electrons on helium as a quantum information platform. Theoretical models of helium phonon- and ripplon-associated losses are not reflected particularly well in what little experimental data exists so far [28]. Increasing the number of electrons in the trap most notably modulates the spatial extent of the wavefunction sampling the helium excitations, so perhaps such multi-electron studies can bring insights into the loss mechanisms, dielectric excitations as a whole, and how to increase the coherence of the platform in general. As interesting as these clusters or Wigner crystals are, however, our work at present is still mostly concerned with the properties of single trapped electrons.

5.3 Properties of Single Electrons

A trapped electron coupled to a superconducting resonator, while reminiscent in some ways of studies of early Cooper-pair box charge qubits [23, 119], is very much its own class of system. Along a voltage trajectory that apparently maximizes the coupling and minimizes the decoherence, there is a clear pair of avoided crossings between the first electron orbital state transition and the harmonic cavity transitions. The smallest decoherence observed so far in a confirmed single-electron system coupled to a cavity exceeds 60 MHz and is dominated by dephasing [28]. The dephasing generally increases with temperature and the magnitude of the external pressing electric field binding the electron to the surface, though not in precise accordance with theories describing the properties of the decoherence induced by helium bath excitations coupled to the electron. Unlike similar measurements of junction-

based charge qubits, the asymmetry and two-dimensionality of the electron trap result in asymmetric pairs of crossings, both in trajectory and coupling strength to the resonator. There is no effective gate charge in which the system is periodic since it is asymmetric in two dimensions, so the ladder of states as a function of gate voltage does not have constant nonlinearity. Similar to more traditional charge qubits, the electron ladder of states is currently also unstable in time, shifting discretely as a function of gate voltage over time in an apparently random process. While this is somewhat understood in junction-based qubits as a change in the effective bias needed to reach a particular electron number on the Cooper-pair box island, the instability remains a mystery for electrons on helium, with perhaps the most likely suspect being movement or tunneling of nearby electrons pinned to defects beneath thinner sections of helium. Anecdotally, this occurs less frequently after attempts to 'clean' nearby electrodes of unwanted electrons, perhaps on the timescale of hours per jump rather than minutes. Interestingly, the same instability is observed in electrons trapped on solid neon [31]. While these trapped electrons offer new flexibilities compared with junction-based charge qubits, they also come with their own challenges that are not yet well understood.

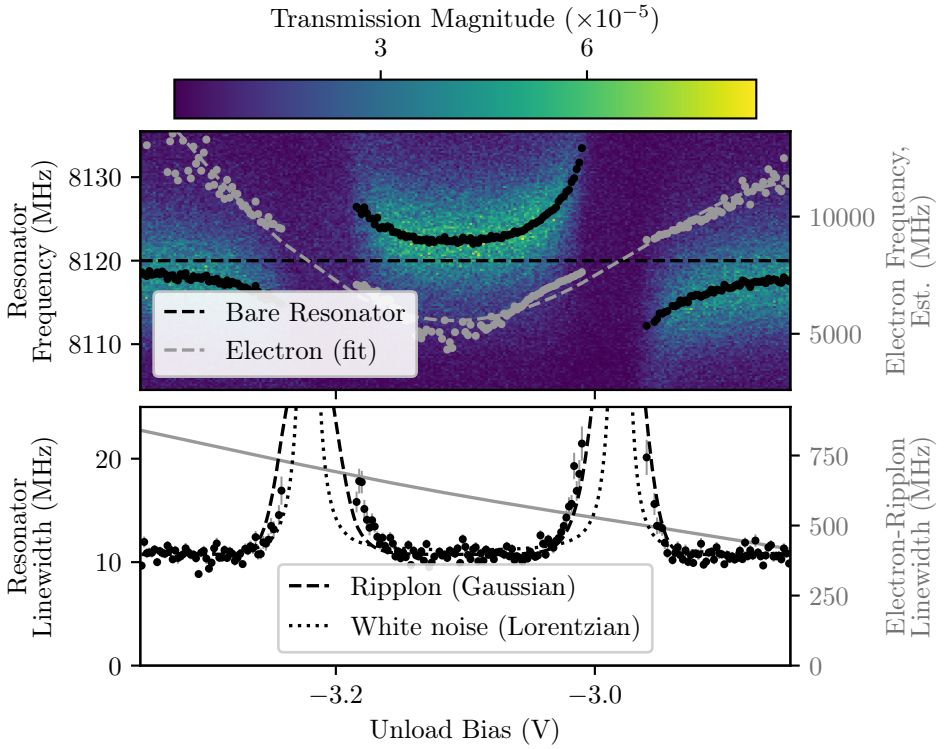


Figure 5.6: Single-electron anticrossing
The electron linewidth is sensitive to the cryostat temperature, which is predicted by the theory of ripplons. The resonator spectral line inherits some of the electron linewidth. As a function of detuning, the resonator linewidth growth is consistent with a Gaussian electron spectral line, supporting that ripplons are the primary contributors. This data was acquired with device 4 in Appendix B at a temperature of ≈ 35 mK with a simulated electrostatic trap depth of ≈ 10 meV.

5.4 Trapping Potential Asymmetry and Stability

The aspect ratio between the orthogonal axes of the electron oscillator is low enough that optimization of system properties requires manipulation of multiple voltage axes. The length scales associated with electrostatic traps for electrons on helium typically result in less than an order of magnitude difference between orthogonal translational motion modes, significantly less than is typical in conceptually similar condensed matter quantum information systems like semiconductor quantum dots. As a result, an electron on helium is very much two-dimensional, so trapping potential asymmetries cannot necessarily be corrected by maintaining a constant ratio of a linear superposition of the device electric field lever arms, as is

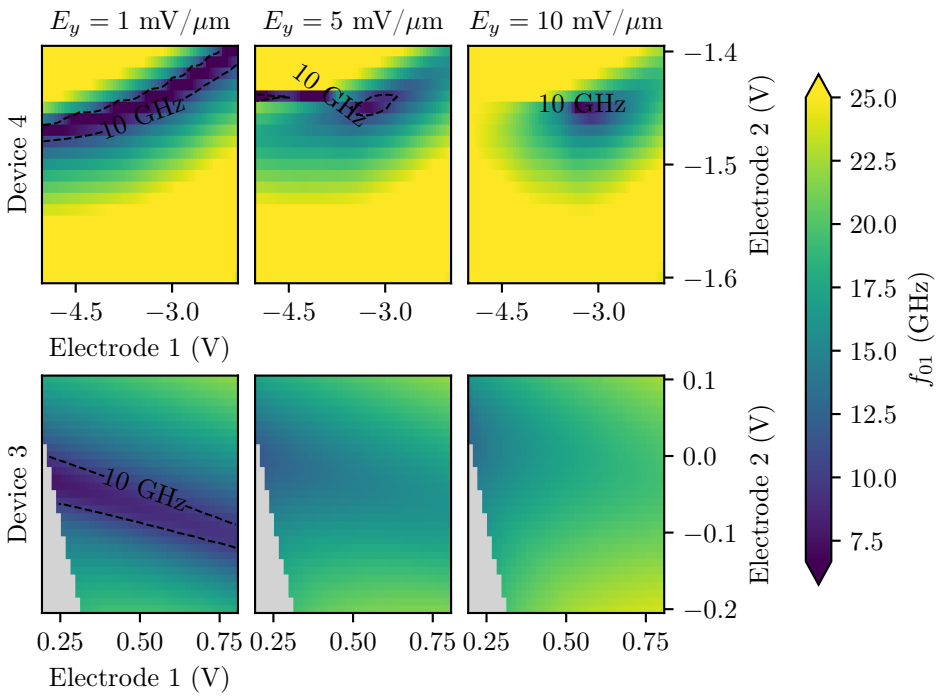


Figure 5.7: Simulated effects of trap asymmetry
The effect of growing asymmetry for two devices with geometrically distinct electron traps was simulated. In both cases, the region in voltage space where the orbital motion approaches the resonator rapidly decreases with added asymmetry on the scale of only a few mV/μm. The top row is simulated from device 4 and the bottom from device 3 in Appendix B.

typically possible for manipulating a one-dimensional system. Both bias asymmetries and magnitudes, therefore, play roles in manipulating the transition frequencies of the trapped electron.

Since the mobility of the system is high, nearby weakly pinned electrons can drift in position over time, perturbing the trapping potential of the electron in the trap. The electrostatic trap curvature contribution of nearby electrons can be as significant as the effect of the helium surface curvature. For a micron-sized trap, one or more electrons pinned to the device surface just outside the trap produce an asymmetry field of roughly 1 mV/μm and a curvature of a few mV/μm^2 at the electron, already corresponding to microwave-range frequencies and corrections. The movement of nearby charges creates instability in the orbital state frequencies over time.

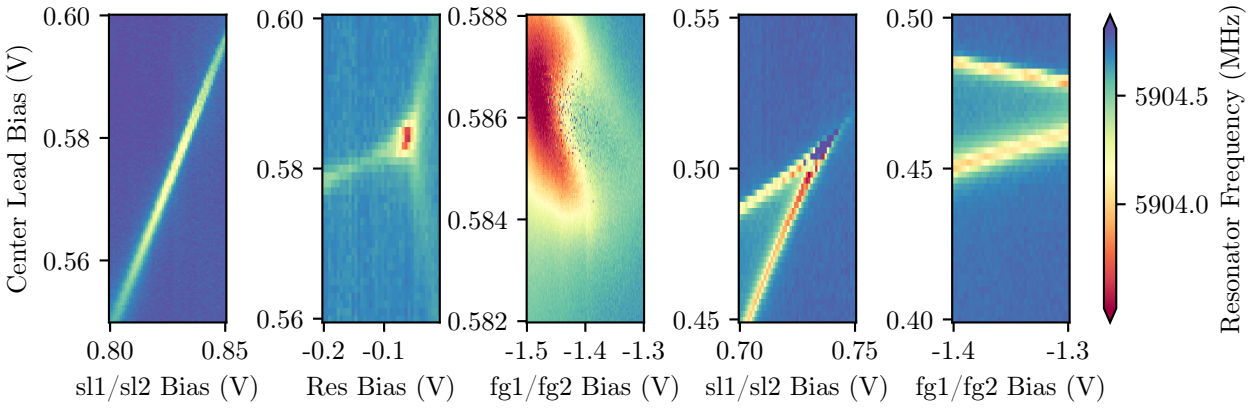


Figure 5.8: Electron in an asymmetric trap

These measurements were performed with a device with a broken wire, so the trap was significantly asymmetric. In this case, the electron could only approach the resonator frequency when every electrode was within a narrow range of biases. To maximize the effective coupling, the electron was tuned with respect to one shared electrode and every other electrode sequentially, and the most sensitive configuration from the previous scan was used as the static configuration for the new scan. Reducing the average bias magnitude with this process maximized the dispersive shift of the resonator. This data was acquired with device 3 in Appendix B.

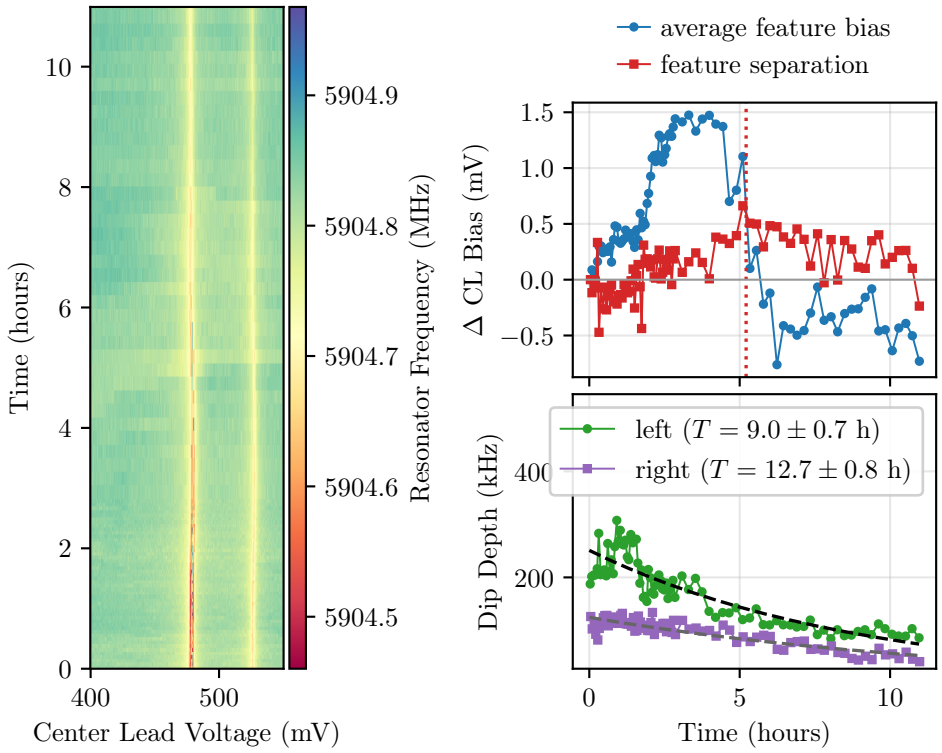


Figure 5.9: Stability in time of the electron trap curvature
Here, an electron is tuned continuously over 11 hours. The observables are the distance between the approaches to the resonator and the dispersive shift. The average bias of the features is relatively constant apart from jumps on a timescale of hours, while the separation between them is largely constant, suggesting that the total asymmetry which sets the minimum frequency changes but the deliberately applied curvature at a particular bias does not. The frequency shift of the two features decreases over time, decaying exponentially with half-day timescales, which also indicates that the asymmetry increases over time. Since the electrostatic trap is positively biased, it is possible that charge migration either through the silicon substrate or from stray floating electrons towards the trap could be responsible for the growing asymmetry. This data was acquired with device 3 in Appendix B.

CHAPTER 6

THE ELECTRON ORBITAL STATE LADDER

Nonlinearity is at the heart of most observables one might be interested in for the development of many quantum information platforms. Like how understanding the anharmonicity and level structure of the transmon has formed much of the basis of quantum information science with modern superconducting circuits [76, 120], understanding and manipulating the nonlinearity of single electrons will be central to their development as charge qubits or otherwise. Electrons on helium enjoy a unique position in this respect; the electron exists in a pristine dielectric environment, so in principle its ladder of states is significantly more manipulable than in other solid-state platforms. An electron's properties should be determinable with finite element modeling and tunable in situ, in contrast with semiconductor and superconductor qubits, whose properties are highly sensitive to fabrication parameters [121]. Therefore, the platform offers powerful flexibility in its nonlinear properties. However, the prominence of asymmetries and instabilities in recent experiments brings this claim into question. In this chapter, we discuss the nonlinearity of the orbital ladder of states of a single trapped electron and the novelties of the electron anharmonicity. The experiments in this chapter were performed in collaboration with EeroQ Quantum Hardware, who provided the device and measurement equipment during a three-month internship.

6.1 Studying Electron Ladder Nonlinearity with a Resonator

While current typical decoherence rates in electrons on helium make studying the electron ladder of states challenging, the significant anharmonicity partially makes up for it. Ordinarily in cQED, for example with a transmon or fluxonium, one can study the qubit ladder of states via two-tone spectroscopy [119, 122]. By probing the system at different frequencies, one can watch for the spectroscopy signals associated with the qubit absorbing or emitting

a photon, and different spectral lines respond with varying contrast to tones of different intensities. Understanding this space is vital to engineering high-fidelity gates since it is necessary to avoid leakage of information out of the intended computational subspace. In the case of an incoherent system, however, it is challenging to distinguish the broad spectral lines associated with higher-order transitions, especially without a quantum-limited amplifier. However, the anharmonicity of the orbital states can be large with $\alpha/\omega > 0.1$ and the coupling strength can be made large through the use of high-impedance microwave resonators [110]. Therefore, it is possible to observe at least characteristics of the electron's nonlinearity with only single-tone spectroscopy, never exciting the electron from its ground state [123, 124].

A cavity coupled to an electron inherits some of the nonlinearity of the orbital state spectrum into its self-Kerr, so it is possible to gather information about the electron orbital states only observing the cavity as a function of gate voltage and drive strength [123–126]. In the dressed basis observed in experiment, the cavity Hamiltonian is no longer harmonic due to repulsion from the electron energy levels. The effective Hamiltonian of the driven, electron-coupled cavity in the dispersive limit can be represented as

$$H/\hbar = (\omega_a + \Delta_a)a^\dagger a + \sum_i K_i (a^\dagger a)^{i+2} + \epsilon_d(a + a^\dagger) - i\frac{\kappa}{2}a^\dagger a \tag{6.1}$$

Each K_i of the cavity determines a photon-number-sensitive contribution of a unique moment to the cavity frequency. Commonly studied as the Hamiltonian in systems like quantum-limited parametric amplifiers, the cavity self-Kerr, often defined as the change in transition frequency per intracavity photon number, can be estimated experimentally through variable-drive-strength single-tone spectroscopy of the system [127]. While it is not possible to decompose the observed dressed states back into cavity and electron frequency ladders, the ordered contributions to the cavity frequency expand in powers of the dispersive parameter g/Δ, implying that lower-order terms tend to dominate the self-Kerr at relatively

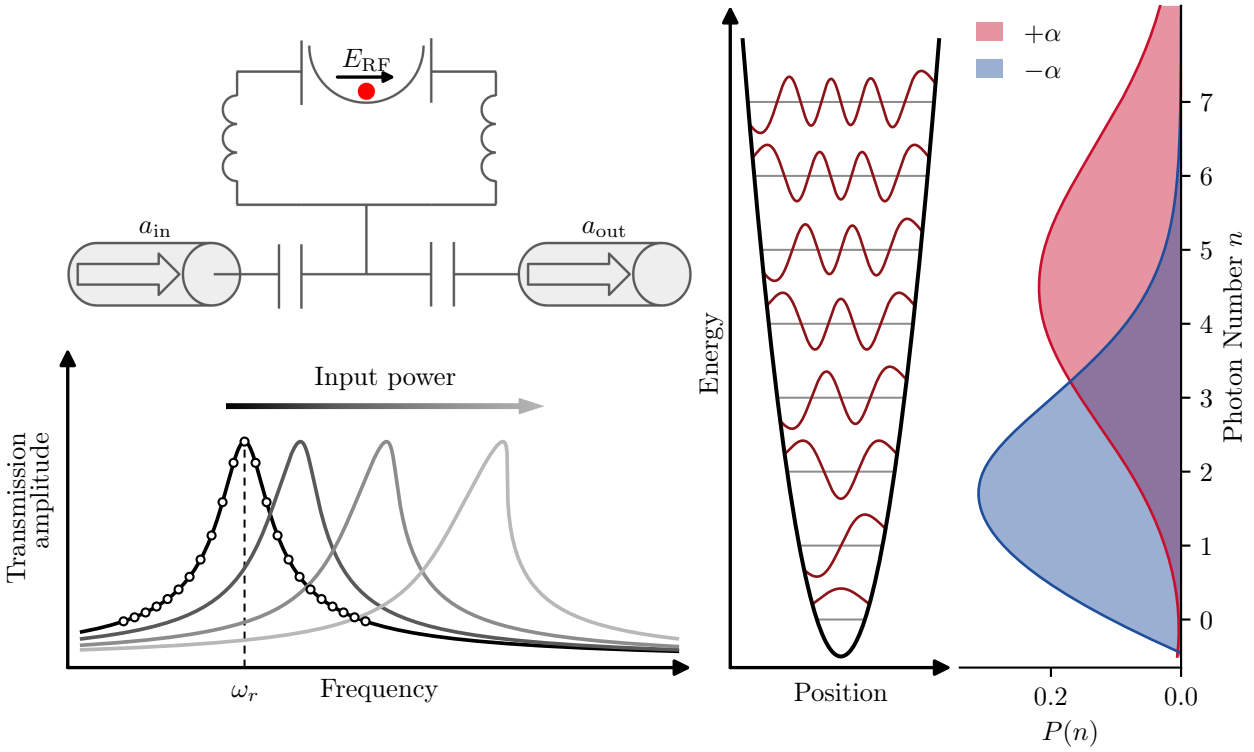


Figure 6.1: Experiment schematic for measuring a resonator with Kerr
The largely linear resonator state ladder inherits some of the nonlinearity of the electron orbital motion. Unlike in a harmonic oscillator, uneven ladder spacing causes crowding of the Poisson-distributed excitations of the resonator at different mean intracavity photon numbers depending on whether sequential rungs are closer or farther apart. This results in an input-power-dependent resonator frequency sensitive to the nonlinearity of the electron ladder.

low intracavity photon numbers in the dispersive limit. When one term in the bare electron Hamiltonian dominates its ladder anharmonicity, it can be estimated from the leading contributions to the cavity nonlinearity. Therefore, it is possible to learn about the anharmonicity of the electron states, which is largely determined by the cubic and quartic moments of its trapping potential curvature, without directly observing higher-order transitions.

6.2 Nonlinearity of a Single Electron

The drive-strength-dependent nonlinearity of a resonator coupled to the motion of a single electron is consistent with an orbital state ladder with tunable anharmonicity. We convert

the magnitude of a continuous cavity drive into a mean intracavity photon number with the internal and external cavity loss rates as $\bar{n} = \frac{4\kappa_e P_{\text{in}}}{\hbar\omega\kappa^2}$. The cavity spectral line shifts and skews as a function of drive strength due to the presence of the electron. When nearer to resonance with the electron or when its ladder is more nonlinear, the effect is more pronounced. Device electrode biases shape the electron's confining electrostatic trap curvature, so a drive-strength dependence that changes with electrode bias reflects an electron ladder of states with changing rung spacing. At sufficiently low drive strengths, the response is linear or quadratic to a good approximation since only leading K_i contribute in the effective Hamiltonian. Stronger drives result in many K_i whose contributions cannot be distinguished uniquely, and near the critical photon number n_{crit}, the approximations of the Jaynes–Cummings Hamiltonian break down. To best estimate the electron orbital state ladder from the resonator response,

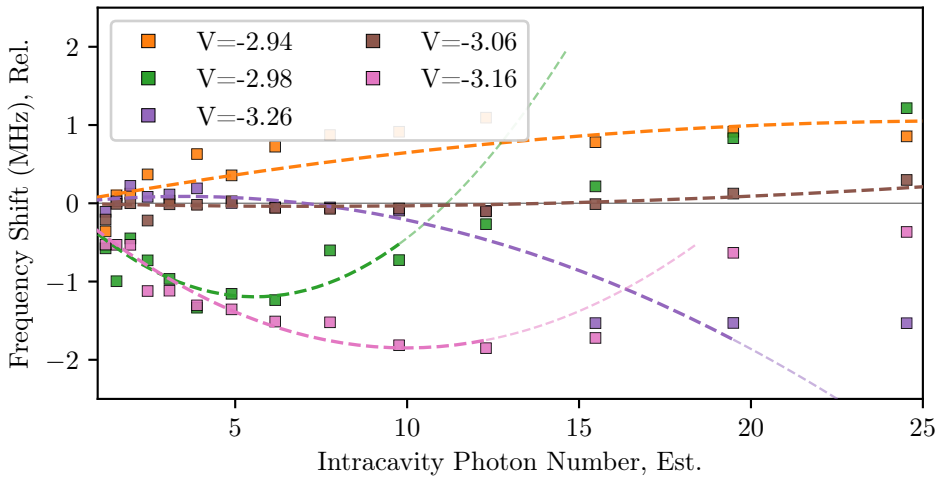


Figure 6.2: Nonlinear-resonator Kerr raw traces
Selected data traces illustrating non-monotonic resonator frequency as a function of drive strength due to competing nonlinear terms in the electron Hamiltonian. This data was acquired with device 4 in Appendix B.

we build a model matching the electron response to two nearly orthogonal lever arms and compare the experimental results to simulation of the cavity-electron dynamics. When the ladder anharmonicity is comparable to the detuning between its levels and the resonator, the leading-order dispersive shift is sensitive to the anharmonicity. Therefore, it is necessary

to recreate the experiment in simulation to make precise descriptions of an appropriate ladder of states. First, we match the simulation's electrostatic potential to the experimental response to the electrode biases. Luckily, asymmetry in the trapping potential results in a distinct two-dimensional shape to the response; these 'blobs' are clearly elliptic at some angle with respect to the electrode bias axes. It is straightforward to brute-force search near the experimental bias values with small asymmetries and offsets when the shape of the response is qualitatively simple. If the matching 'blob' creates an appropriate electron ladder of states, simulating the drive-dependent response of the resonator should match the experimental results. Solving the Lindbladian for the steady-state response of the cavity under a coherent drive is computationally expensive when the Hilbert space is large with many cavity Fock states and qubit transitions that are not necessarily in the dispersive limit. Drawing inspiration from ringdown measurements of cavities, we can initiate the cavity in a particular Fock state and watch its evolution over time through only the leakages inherent to the system, which in this case occur much more quickly than leakage of photons from the cavity ($\gamma \gg \kappa$) [128, 129]. The cavity self-Kerr simulated via this method largely follows the observed Kerr. While it is possible that unexpectedly large higher-order terms in the Hamiltonian could also produce similar results, it is not unreasonable to have confidence in the simplest configuration that reproduces the results. These results also show that the picture of an electron levitating in a predictable dielectric environment is merited.

The ground-state anharmonicity most consistent with the observed resonator self-Kerr is $\approx \pm 1$ GHz throughout the range of experimental data, tuning smoothly but rapidly between the two avoided crossings. Each orbital state transition of the electron is qualitatively even-polynomial along the probed voltage axis, with each parabolic trajectory progressively offset from the last towards the direction corresponding to a less quadratic confining potential. The point where the resonator self-Kerr flips sign points to the ground-state anharmonicity vanishing. The simulation of the system dynamics produces an agreeing resonator self-Kerr

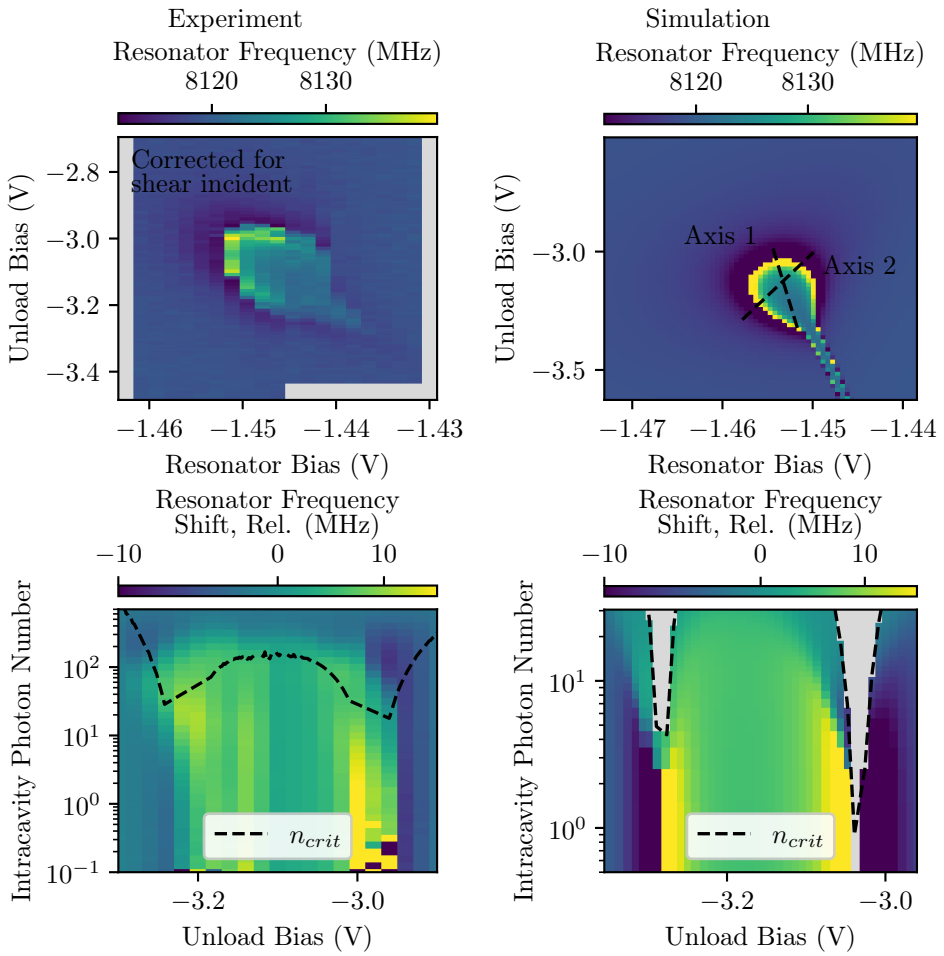


Figure 6.3: Comparison of model to data in Kerr experiments
We find good agreement between the power dependence of a model system best matching the electron response to two electrodes and experiment. The electrostatic model was found with a brute-force optimization search guided by the distinct shape of the electron response. This data was acquired with device 4 in Appendix B.

at the correct dephasing scale of 100 MHz for the ground state and increasing approximately harmonically for the higher-order transitions. A simulation with significantly less dephasing suggests qualitatively different behavior would be observed for a more coherent electron, including a bias configuration where the resonator nonlinearity vanishes but the first-order anharmonicity remains large, which would be desirable for dispersive readout of the electron state.

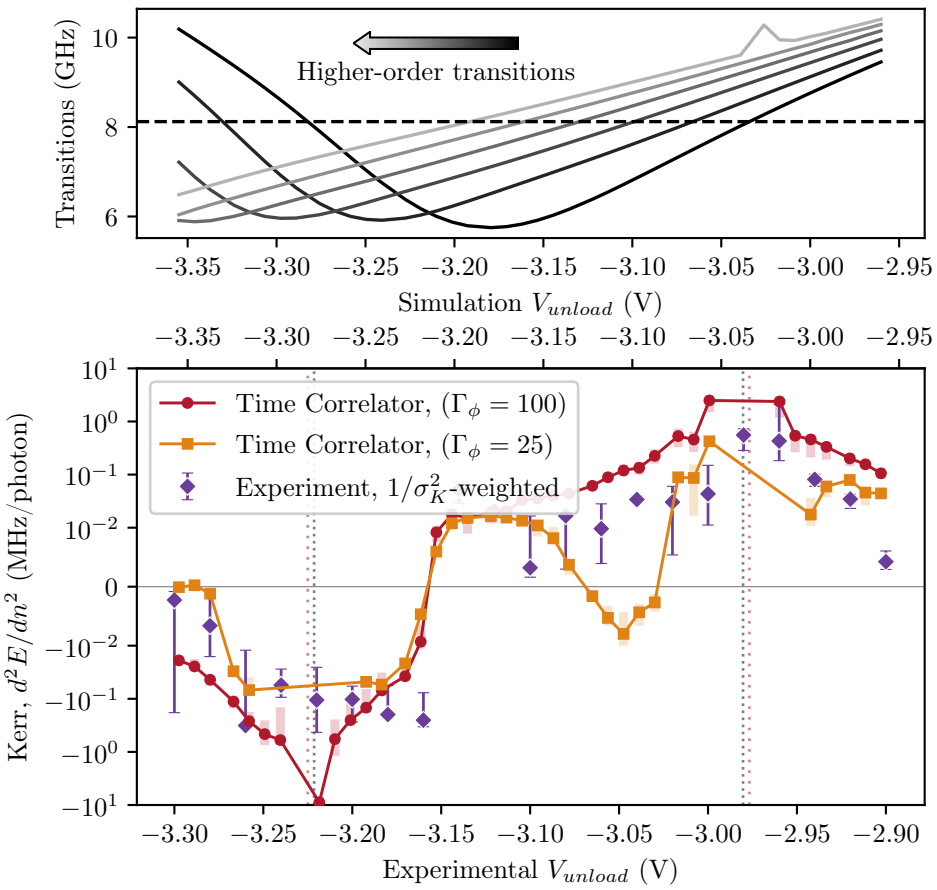


Figure 6.4: Experimental evidence of anharmonicity tunability of orbital states Along a double anticrossing between the resonator and electron, the resonator frequency is measured as a function of mean intracavity photon number, converted from the effective drive strength applied to the resonator. At stronger drives, the Jaynes–Cummings approximation breaks down ($n_{crit} \approx \frac{\Delta^2}{4g^2}$). At weaker drives up to ∼10 intracavity photons, the response of the cavity frequency to drive strength can be fitted to a second-degree polynomial, and the derivative(s) of the frequency with respect to drive strength is the Kerr. The change in sign of the Kerr in the data is consistent with the first-order anharmonicity tuning smoothly from ≈ -1 to 1 GHz. This data was acquired with device 4 in Appendix B.

6.3 Implications for Future Studies

The anharmonicity of the electron orbital states demonstrates qualities relatively unique to the landscape of superconducting circuits. Most notably, the Kerr flips sign between the pair of anticrossings, indicating that the first-order anharmonicity also changes sign, effectively becoming tunable in sign across three orders of magnitude, from being nearly harmonic to

an anharmonicity on the order of the transition frequencies themselves. This is substantially beyond what is typical with junction-based qubits. With a more stable electron, it would be possible to take denser data along the transition point. The anharmonicity significantly factors into the gate speed possible with an electron charge qubit while also limiting the potential of bosonic enhancement to the charge coupling by displacing the electron further. Tunability of the anharmonicity offers rare flexibility in designing logical operations for the platform and increasing their fidelity, such as by pairing electron qubits with opposite anharmonicities to facilitate higher-contrast interactions [130]. These results also potentially form the foundation for creating a parametric amplifier from an electron on helium, which would have an impressive tuning range and could handle significant drive strengths given the relatively deep trapping potentials utilized in the platform [100, 101, 127]. Matching the apparent resonator self-Kerr to a simulated cavity coupled to an electron builds confidence in our estimated charge state ladder and unlocks deeper observations about the system nonlinearity.

These observations of the electron nonlinearity suggest several operating principles for maximizing the coherence of the platform in the near term. Presently, all measurements of the electron orbital state lifetime fall modestly short of predictions. In the vicinity of the charge sweet spot in these experiments, which would normally be an intuitive measurement configuration, the state ladder goes from no first-order anharmonicity to multiple higher-order transitions crossing the resonator. These states are likely even less coherent than the first excited state. On either side of the anticrossings, the ladder again either looks similar or the transitions bunch together into a lower-anharmonicity configuration. Just as population fraction in the higher states boosts the observed cavity self-Kerr from what would be expected for a higher-coherence system, these states likely reduce the qubit's lifetime. Aside from reducing the asymmetry in the system, which ironically ensures a point at which the first transition frequency is semi-classically insensitive to height variation of the helium surface,

further increasing it or decreasing the resonator frequency until the transitions never cross the bare resonator should improve the charge lifetime while also preserving the anharmonicity tunability. While much work remains to be done in the development of levitating electron qubits, many avenues for improvement exist for this unique nonlinear system.

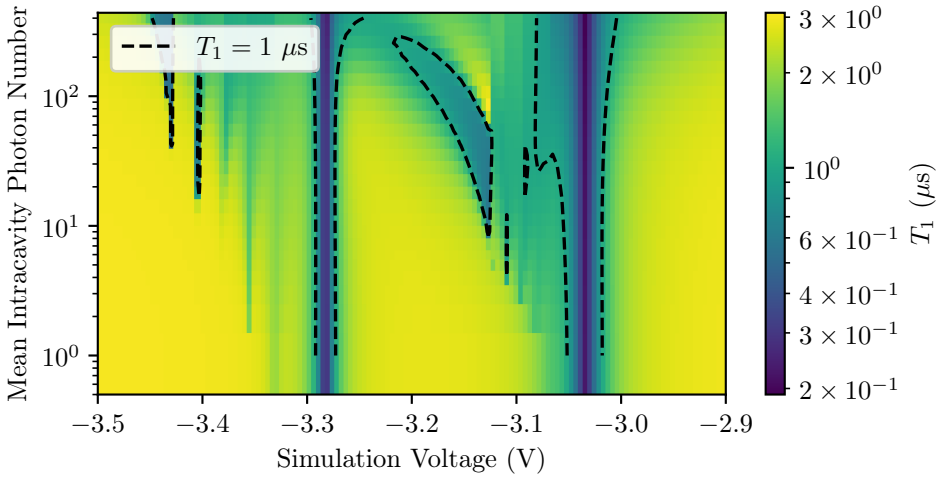


Figure 6.5: Simulated electron lifetime dependence on trap structure
In the case of stronger ripplon coupling, the spectral lines of the electron orbital states are broad. When the spectral lines nearly overlap and some are degenerate with the resonator, at higher applied resonator drives leakage through the resonator is enhanced, resulting in a decrease in the lifetime in this case even near the bias-insensitive point of the electron tuning curve.

CHAPTER 7

ELECTRONS ON NEON

While this dissertation's focus is electrons on helium, the past several years have seen the revitalization of the broader noble gas substrate research community. Noble gas substrates attracted significant research attention in the 1970s in the two-dimensional electron physics community [4, 131]. Theory had already predicted exciting phenomena arising from strongly correlated inter-electron interactions such as the formation of Wigner crystals and sharply resolved Landau levels, but experiments were limited by substrate imperfections [12, 132]. Research in semiconductors, of course, rapidly advanced and eventually opened doors to studying most of this physics, and continues today [133, 134]. 'Ultrapure' substrates composed of condensed noble gases, in theory, circumvented the issues associated with substrate impurities and limited electron mobilities. While superfluid helium is the best-known such instance, motivating decades of research in electron mobility aside from its critical role in cryogenics, the liquid and solid phases of other noble gases were at the time perhaps equally enticing [135].

Neon was first cooled to its triple point in the early 20th century [136]. Deterministic growth of solid noble gas substrates was challenging. Triple-point dynamics discourage localized solidification of moderate-thickness liquid films. Instead, the liquid essentially vaporizes and is redeposited throughout the sample container as a rough, nanometer-scale solid film, unless the transition occurs at much higher pressures [8, 137]. In contrast to research on electron gases on liquid helium of thicknesses spanning tens of nanometers to millimeters, growth of solid neon was generally restricted to ultrathin-film and bulk neon crystals. Additionally, these films were rough, with electron mobilities orders of magnitude less than in experiments utilizing helium films, with limited dependence on the roughness of the underlying device substrate. While these limitations largely remain today, experiments with levitating electrons have breathed new life into the study of solid noble gas substrates,

and integration of these substrates into quantum information science and into studies of electron gases has progressed significantly in only a few years [27, 31]. This chapter will detail experiments studying neon films in the primary thickness regime of interest to quantum information applications and briefly detail measurements of single electrons trapped on roughness-dominated solid neon films.

7.1 Neon Growth

A critical factor to the continued development of solid noble gas substrates as a platform for levitated electron experiments is the degree to which the dielectric growth can be controlled. In contrast to most condensed matter quantum information platforms, levitated electrons have spatial mobility, offering the prospect of straightforward all-to-all connectivity of qubits. However, surface pinning from a rough surface largely negates this possibility. Similarly, if electron trapping potentials are largely determined by surface morphology rather than deliberately generated electric fields, then the platform begins to resemble a collection of coherent defects. Unlike with superfluid helium, where the electron floats about 11 nm above the helium surface, an electron on neon is only separated from the surface by 1–2 nm, making surface roughness of critical importance for the system. Growth of these solid films at the primary length scales of interest for quantum information applications, tens to hundreds of nanometers, remains underexplored relative to how promising the platform is.

Neon reaches its triple point at a temperature slightly over 24 K when below ambient pressures, making studying its growth with superconducting circuit devices challenging. At temperatures achieved by typical cryocoolers, microwave devices fabricated from most commonly studied superconductors remain very lossy due to conductor losses and the impact of substantial thermal radiation. Iterating through neon film growth conditions would therefore typically require repeated cycling of a dilution refrigerator between a few kelvin and millikelvin temperatures, taking optimistically several hours per cycle. Luckily, there are

superconducting materials more suitable for studying the growth of neon films.

Some d-wave superconductors such as YBCO feature exceptionally high critical temperatures while also being suitable materials for microwave resonators. Unlike commonly used s-wave superconductors such as niobium and aluminum, such d-wave superconductors enable fabrication of microwave devices suitable for studies in the tens of kelvin temperature range. The superconducting energy gap is anisotropic in momentum space for d-wave superconductors, creating nodes for which the gap vanishes [138]. Low-energy quasiparticle densities near these nodal points are not exponentially suppressed below the critical temperature of a d-wave superconductor, making them naturally lossier at finite temperatures than s-wave superconductors. However, the critical temperature of YBCO is approximately 92 K [139], and microwave resonators fabricated from this material can still achieve internal quality factors of 10^4 at 20 K [140, 141]. We can therefore utilize the excellent SNR afforded by microwave resonators to study the growth of neon films near the triple point and remove the need for a dilution unit in such experiments.

We utilized a voltage-tapped YBCO coplanar stripline (CPS) resonator to monitor the growth of solid neon from its liquid phase near its triple point in real time. Similar resonator-based studies of neon film growth have recently been performed using YBCO resonators [142] and NbTiN resonators [143]. The frequencies of the resonator modes are largely determined by the mutual and self-capacitances and inductances of the device geometry. The capacitances in particular are sensitive to the effective dielectric constant of the resonator locale, which changes as neon fills the vacuum space around the resonator. While just using a small capacitor may accomplish much the same, adopting a superconducting resonator for measurement offers several conveniences and opportunities. First, the modal profiles of the resonances are generally localized to the device area rather than filling the entire bias line, reducing the measurement chain sensitivity to low-frequency electrical noise. At the same time, the center of the Lorentzian spectral line can routinely be located to a thousandth

of its linewidth or better, making for exquisite sensitivity to localized capacitance changes. Using a superconducting resonator also opens the door to studying the microwave loss of the dielectric environment and the effect of the added noble gas substrate, which is only presumably pristine. Finally, while not successfully demonstrated in this dissertation, the coupling of an ensemble of electrons on solid neon to a superconducting resonator would be a valuable early experiment in the study of the mobility and coherence of these electrons [79]. In this section, we detail a study performed on solid neon growth and dielectric loss and discuss the prospects for further electrons-on-neon experiments that draw inspiration from previous experiments on helium.

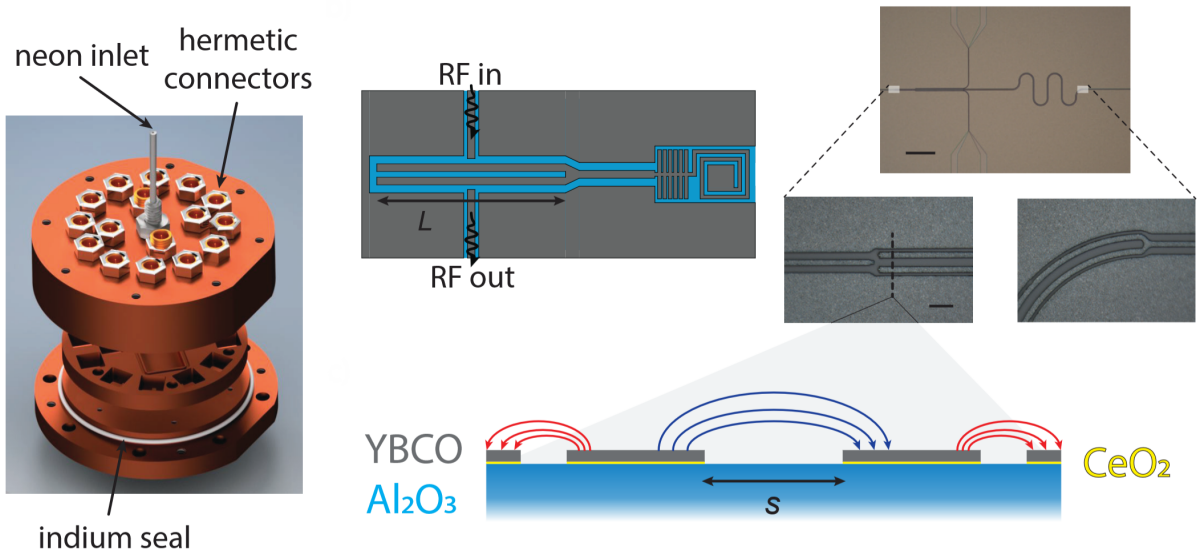


Figure 7.1: Experiment setup for monitoring neon growth
Similar to the helium filling experiments described earlier, we also monitor growth of solid neon using a coplanar stripline resonator. Since at low pressures the gas-to-liquid-to-solid neon phase transitions occur between 24 and 27 K, the resonator is fabricated from YBCO with a superconducting critical temperature of approximately 90 K. Adapted from Ref. [99].

The sensitivity of a microwave resonator to its dielectric environment is determined by the length scales of its modal fields. To maximize the sensitivity to changes in neon thickness in the hundreds of nanometers regime of most interest, we utilize a resonator with a minimum gap width of one micron, near the edge of the optical resolution limit for photolithography.

By simulating the change in capacitance associated with different amounts of neon on the device with finite element modeling (FEM) and converting the capacitance changes to modal frequency shifts, we were able to estimate the amount of neon coating the device at a given time based on the frequencies of the resonator modes. Motivated by applications to floating electrons, with this device, we studied how the amount of solid neon changes with the depth of the liquid neon on the device immediately prior to the phase transition and how the rate of the transition affects the result. Additionally, we studied neon liquid dynamics on the micrometer length scale, observing periodic liquid instability.

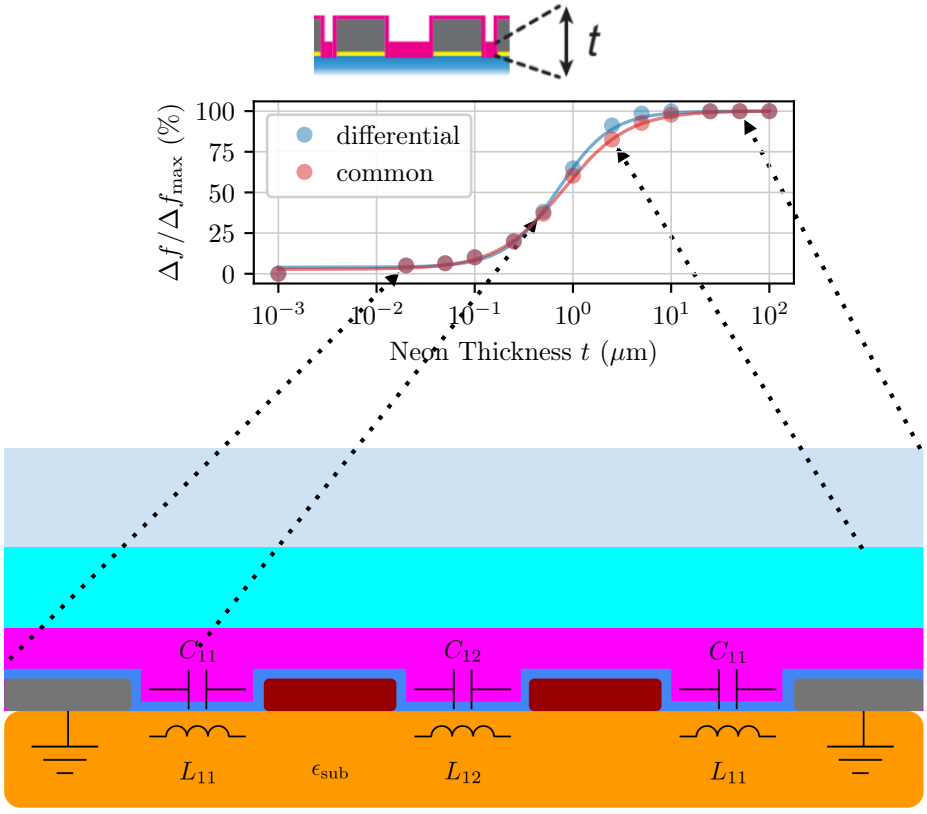


Figure 7.2: Sensitivity of the device to neon growth
The sensitivity curve to neon growth of the resonator frequency is determined by the aspect ratio of the resonator's features. This particular resonator was designed to be maximally sensitive to changes in its dielectric environment on the growth scale of 1 μm, which is of most interest to proposals for manipulation of electrons on neon. Adapted from Ref. [99].

Growing a solid neon film when crossing the phase boundary requires a significantly

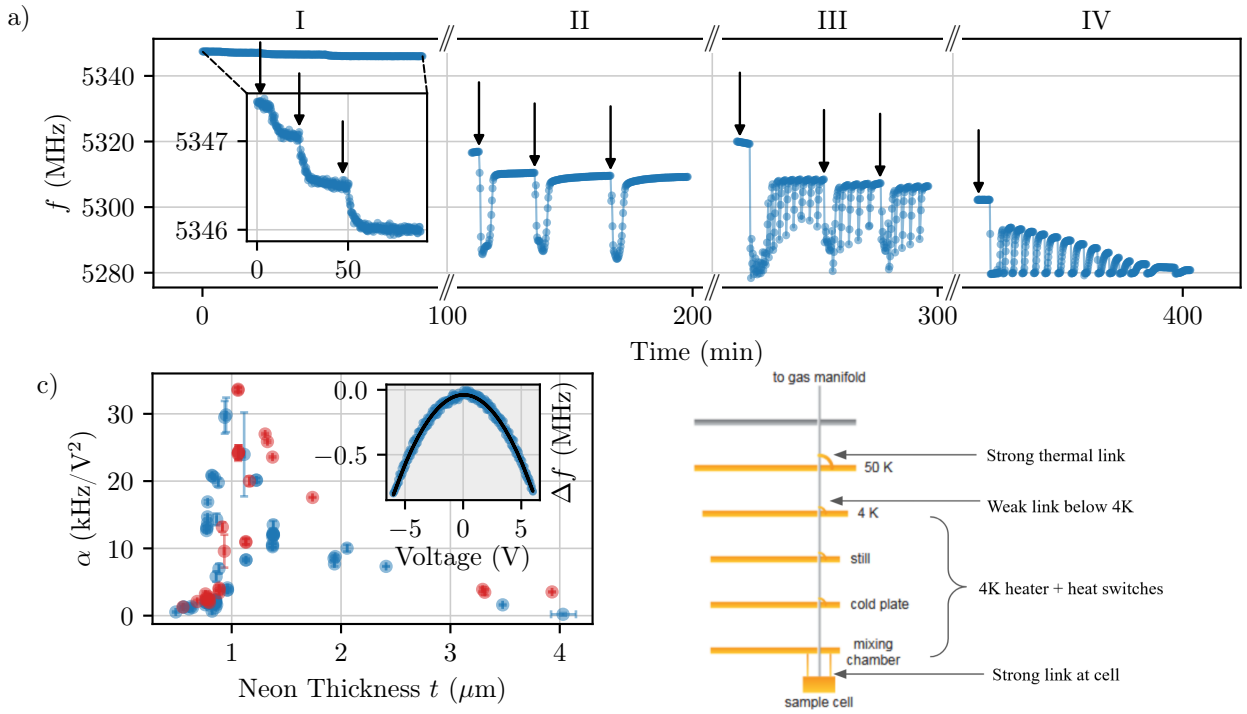


Figure 7.3: Liquid neon deposition and dynamics
Progressive filling of the device modal sensitivity volume with liquid neon is divided into four apparent phases: 1. Liquid thin films, 2. Stable thicker films, 3. Unstable films, and 4. Total saturation of the sample's modal volume. By applying voltage to the resonator, the neon liquid is attracted to the increase in electrostatic field density, increasing its thickness near the resonator. This effect is maximized near the height of optimal sensitivity for the resonator, but the magnitude of response away from the optimum differs from the earlier dielectric sensitivity curve. Thin films are too stiff to reshape while thicker films must move more neon, resulting in asymmetrically suppressed response about the sensitive point. Adapted from Ref. [99].

thicker liquid film due to dynamics at the triple point. Most of the liquid evaporates into a thin solid film distributed throughout the sample cell, but adding enough liquid to compensate allows more of the liquid to solidify locally on the device surface. Eventually, the majority of the liquid remains, saturating the device's modal volume. While there is approximately an order of magnitude range of solid growth for a given liquid height, repeated phase transitions could in principle approximately reach a target solid height [144].

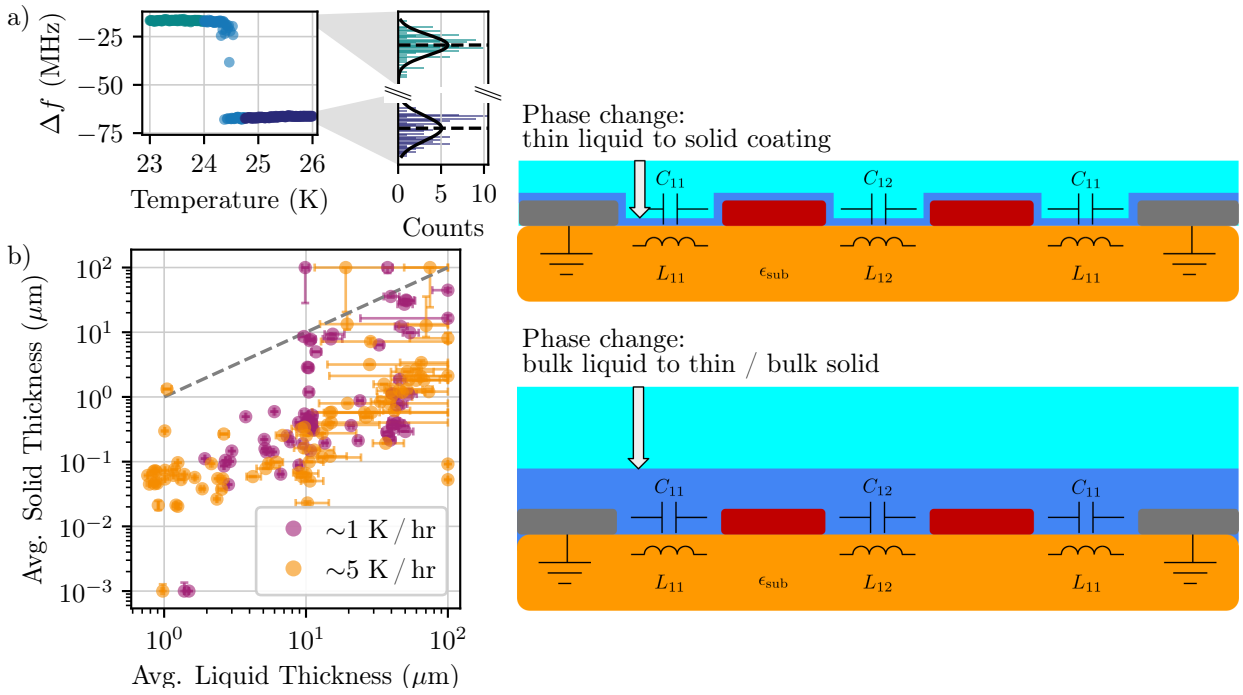


Figure 7.4: Solid neon growth through a quasi-static phase transition
Over many trials and estimated liquid thicknesses, the resulting solid neon layer thickness is estimated at two transition rates corresponding to previously recorded rates for more stable solid neon growth and a rate that is significantly higher. The maximum rate is effectively the maximum cooling rate of the cryostat pulse tube for the experiment's presented thermal load. Little difference in growth patterns is observed between the two rates, and a specific solid neon thickness can only be targeted to within an order of magnitude for a given instance of solidification. Growing any amount of solid neon typically requires significantly more liquid since much of the solid is redistributed throughout the sample cell interior surface due to phase change dynamics near the neon triple point. Adapted from Ref. [99].

7.2 Dielectric Loss Experiments with Tunable Dielectric Thickness

Understanding how both macroscopic and microscopic systems with quantized energy levels interact with their local electromagnetic environment is central to circuit quantum electrodynamics. Coupling to two-level systems (TLS) in local dielectrics remains a common limiting loss source in cQED systems. Much effort has gone into understanding how resonators and junction-based qubits couple to lossy surfaces and material bulk, and in situ techniques for manipulating away this coupling have recently led to qubit lifetimes on the scale of milliseconds in planar circuits [47]. Since some studies estimate that at least an order of magnitude

of lifetime improvement remains on the table before normal-fluid fraction conductor loss becomes the limiting factor for junction-based qubits in the microwave range, exploration of low-loss dielectrics remains a productive research direction. Noble gas substrates are presumably lossless, free from internal electric dipoles, and can be isotopically purified of spins. Uniquely, they can be grown in situ on the device surface, altering the dielectric loss by drawing electric field density out of the bulk towards the pristine noble gas liquid or solid. This section details the effects of locally grown neon on the losses of our YBCO device.

We observed a decrease in the internal loss of both modes of our YBCO resonator that trended with the reduction in participation of the modal electric fields in the underlying substrate. After saturating the sample cell with solid neon, the internal quality factors of both the common and differential modes increase, specifically doubling in the case of the latter, suggesting a significant reduction in the dominant internal loss mechanism. The increase in quality factor as a function of neon thickness changes most rapidly between 100 nm and 1 μm of neon coating the device, coinciding strikingly with the sensitivity curve of the device frequency to its dielectric environment, indicating that the spatial distribution of the most lossy coupling is similar to that of the modal participation in the device dielectrics. The common mode loss decreases more gradually than that of the differential mode, likely owing to the former's participation in the on-chip coiled filter, which has a spatial extent an order of magnitude larger than that of the resonator itself. Given the effect is observed coarsely in the liquid phase as well, the mechanism is related only to the addition of the dielectric rather than any properties of the solid neon crystallization.

Using finite element modeling (FEM), we simulated the dielectric participations for various levels of neon coating the device surface, finding that the loss mitigation by the added neon cannot be attributed to traditional dielectric loss mechanisms in the device substrate and surface. Several studies have modeled both transmon and resonator dielectric loss effectively by carefully subdividing the device participation spatially [69, 145–147]. Given the

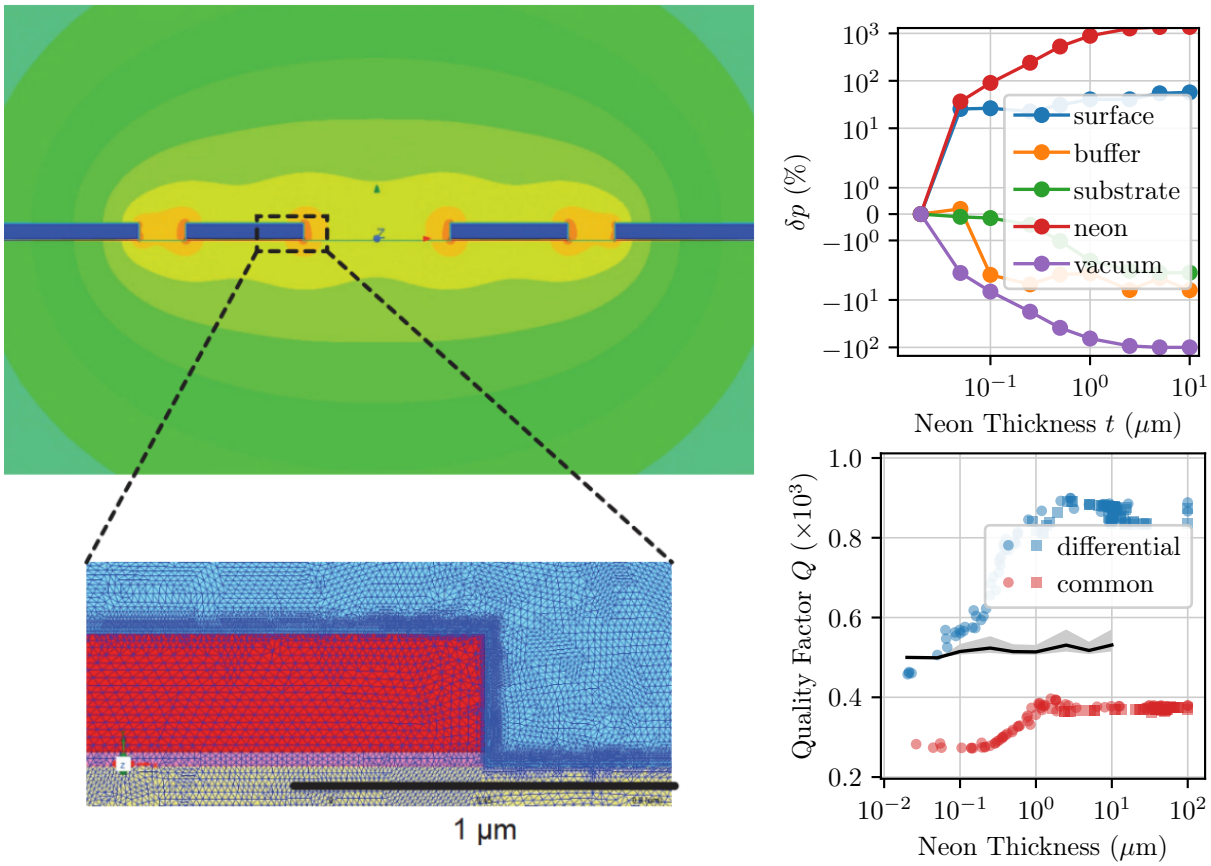


Figure 7.5: Dielectric loss model from participation ratios
The geometry of the microwave resonator and the dielectric constants of nearby materials determine the energy density of the resonator electric field in different regions. The total loss of the resonator is determined by the individual loss rates of the materials scaled by their participation fractions. Using dense meshing of a two-dimensional model, we can estimate how the addition of the neon dielectric changes the participation in each device material for a given thickness. In experiment, we observe a significantly greater decrease in resonator loss than in simulation, suggesting that most of the loss is due to thermal radiation which the neon shields the device from. Adapted from Ref. [99].

low quality factor of the device and uniformity of its cross section along its length, we simplified this subdivision, purely extracting the electric field distribution in two dimensions and estimating the loss from only the most basic participants: the device sapphire substrate, the thick buffer oxide at the YBCO-sapphire interface, the rough surface layer of the YBCO, and the neon itself. The resonator internal quality factor follows from the participation ratios p_k, the fraction of the electric field energy stored in each dielectric, and their associated loss

tangents $\tan\delta_k$,

$$\frac{1}{Q_i} = \sum_k p_k \tan\delta_k + \frac{1}{Q_{other}}, \qquad \sum_k p_k = 1,$$

while Q_{other} collects non-dielectric losses and the resonator frequency tracks the total capacitance as neon replaces vacuum. Across a range of plausible dielectric constants for the surface and buffer layer, we predicted a maximum increase in a dielectric-loss-limited quality factor of less than ten percent for a device limited by loss concentrated in the buffer dielectric rather than the order-of-magnitude stronger observed improvement. Some studies have attributed similar results with noble gas substrates to a reduction in incident thermal quasiparticles; there is significant blackbody radiation above temperatures in the millikelvin range and the gapless nature of YBCO allows for many pair-breaking opportunities across the thermal distribution of energies. Because we found no measurable power dependence of the quality factor at any temperature, we concluded that the loss was largely due to generation of thermal quasiparticles far beyond the microwave energy scale, consistent with the common picture of conductor-limited losses in high-temperature superconductors. In the case of hydrogen, it is thought that YBCO surface oxides can polarize local spins in the frozen gas, reflecting incident thermal radiation [148]. However, given that we observed device losses smoothly decreasing with neon thickness and the gas is largely spin-free, we could not identify a sole mechanism responsible for the observed effect. That being said, these results do point towards potential benefits in device encapsulation in solid noble gases; at least several percent of bulk dielectric loss can always be drawn out of the device substrate into a clean noble gas layer, though surface losses will conversely increase. In a future where dielectric losses are superseded by radiation losses, such encapsulation would certainly be a valuable technique. Future experiments could make use of multimodal resonance structures with different characteristic sensitivity length scales for each mode, allowing for better estimation of competing loss mechanisms and making for a device with strong sensitivity to dielectric filling at all length scales.

7.3 Towards Electron Ensemble Detection on Neon

Isolating one electron from many is a natural first goal in any free-electron system, so control and characterization of an electron ensemble on neon is of significant interest. Over the course of these experiments, we attempted to generate a detectable ensemble of electrons over a wide range of temperatures, neon thicknesses in both solid and liquid phases, and tungsten filament heating parameters. We found no definitive signs of voltage-dependent or hysteretic signals pointing towards the presence of electrons on the neon surface similar to the telltale signs of electrons over a resonator on a helium surface, though we did observe hysteretic phase change behavior after firing the filament that could point towards either immobile electrons or altering of the neon surface morphology by the heating of the tungsten. The most plausible explanations for these observations are a lack of electrons or, more likely, immobile electrons on a rough neon surface. Electron generation is sensitive to the partial pressure in the sample container since gases dampen the motion of thermally emitted electrons. Helium gas is readily generated by rapid heating of the sample container even at millikelvin temperatures and quickly cools, whereas the partial pressure of neon gas varies sharply between 10 K and the triple point. If electrons were generated, a mobility below the higher end of historically measured values would put the sensitivity to the motion at microwave frequencies below that of our device, even after utilizing locking techniques to reduce the magnitude of device phase fluctuations to just thousandths of a degree. In future experiments, sweeping a wide range of voltage-tuning parametric drives could be a fruitful direction.

7.4 Electron-on-Neon Charge Qubits

Unlike in the case of coherent control of single electrons on helium, which began with characterization of ensembles and is journeying towards longer lifetimes and more complex time-domain manipulations, the story of electrons on neon as a quantum information platform

has unfolded more nonlinearly. The first experiments integrating neon, floating electrons, and microwave resonators quickly showcased some of the most coherent charge qubits yet measured [27, 31]. Development of the platform has involved looking both backwards and forwards: understanding how to grow and move electrons on suitable neon films but also building our understanding of electron qubits on solid neon. While so far this section has exclusively focused on the former, I will now briefly detail the results of our work with collaborators towards the latter.

Although charge qubits, both in superconducting circuits and quantum dots, have largely been superseded by significantly more coherent capacitively and inductively shunted junctions and spin-based dots [76, 122], their study remains relevant. A competitively coherent charge qubit would avoid the challenges of spin isotopic substrate purification and compatibility issues between superconductors and strong external magnetic fields. Electric dipole coupling is also intrinsically stronger than that of magnetic dipoles, allowing for larger coupling strengths at farther distances on a device, making spin-orbit coupling schemes generally promising [149, 150]. In that case, one inherits both the capacity to easily drive the charge state and the superior coherence of the spin at the tradeoff of the latter inheriting some of the former's decoherence. Even if charge qubits never catch up to their peers, coherent charge states are vital to the performance of spin-orbit-based platforms.

In their current state, electron-on-neon qubits operationally resemble very coherent TLS. Electric fields from local DC electrodes move the electron qubit frequency through a parabolic trajectory with regard to applied voltages. In a voltage space of two lever arms, it is common to observe the same parabolic trajectory following a linear relationship between the electrode biases throughout the range of the experiment, which is typically a differential of several volts between neighboring conductors. The coupling strength changes little along the trajectory and typical values range from several to tens of MHz even without high-impedance resonators, over an order of magnitude larger than so-called 'giant TLS' in granular aluminum [151]

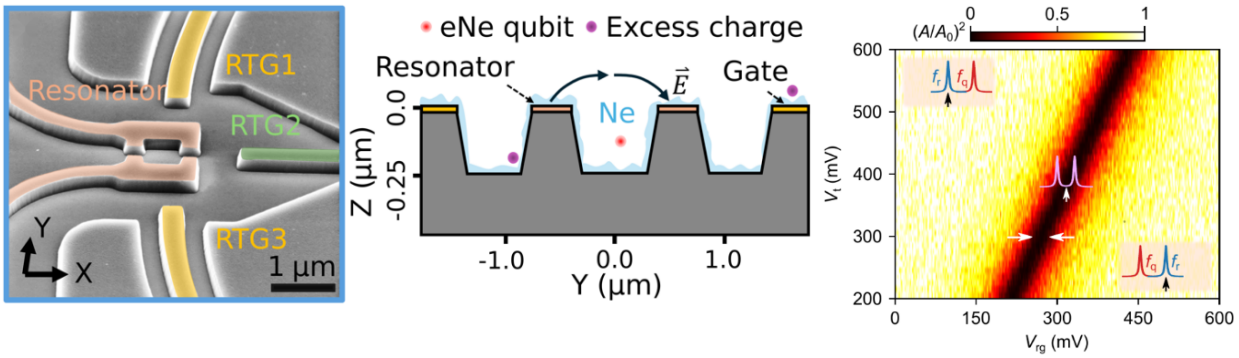


Figure 7.6: Electron-on-neon charge qubits
A split-pin, voltage-tunable, superconducting TiN resonator and several electrodes converge on a small region containing electrons on neon. A device for characterizing electron-on-neon qubits looks similar to a helium-type device, but the trapping potential of the electron is, in this case, likely dominated by surface roughness or defects. These qubits qualitatively resemble TLS in two-dimensional voltage scans and typically exhibit more severe bias-hopping over time than an electron on helium. Reproduced with permission from Springer Nature from Ref. [27, 32].

and anything observed natively on the device without the combination of both a several-nanometer neon coating and firing the filament. While the angle of the trajectory in 2D voltage space remains mostly constant over time, the offset fluctuates in time, with shorter excursions occurring over minutes to hours and larger excursions occurring on the timescale of hours to days more monotonically. Native TLS are, in contrast, typically much more stable. While this instability has made it challenging to perform the full repertoire of cQED experiments with the platform, significant development has still occurred within only a few years in a relatively small research community.

We supported collaborators studying the coherence of electron charge qubits trapped on presumably rough, nanometer-scale neon surfaces. Coherence times ranged from tens of microseconds to over 100 μs, often limited by Purcell loss into the cavity in the best measured cases so far rather than charge noise [31]. In comparison, the coherence time of conventional Cooper-pair box qubits, though outdated, is on the order of microseconds. Unlike in the case of levitated electrons on helium, there are no liquid excitations responsible for rapid dephasing. The variation in coherence times from one qubit to another is poorly

understood, unfortunately. Ordinarily, one would expect charge noise to be the limiting factor in the coherence. Biasing at the charge sweet spot of these qubits does not reveal a consistent lifetime between electrons, indicating that another mechanism that varies more aggressively between one qubit and another is primarily responsible for the loss. However, the relatively long lifetime of these charge qubits makes them excellent probes of charge noise in their environment.

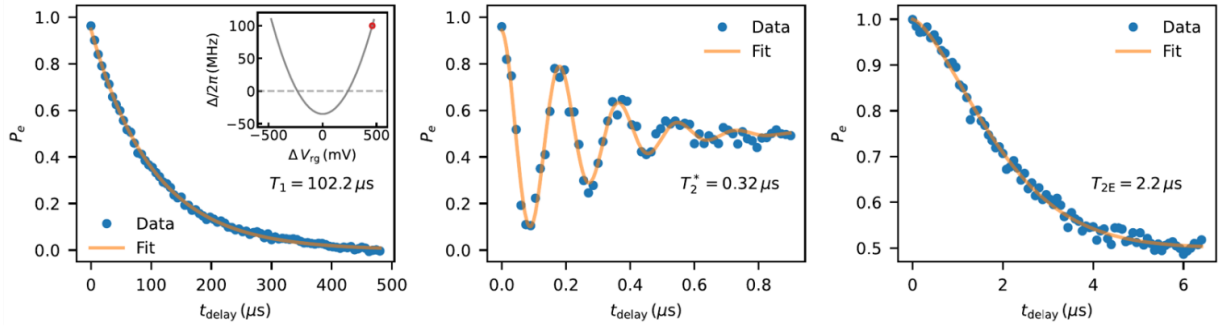


Figure 7.7: Lifetime and coherence of an electron-on-neon charge qubit
Electron qubit lifetimes on solid neon can be exceptionally long for charge qubits. The lifetime and coherence are sensitive to the bias configuration in a way that is not uniform from one trapped electron to another. The electron frequency trajectory with regard to external electrode bias is typically parabolic. Reproduced with permission from Springer Nature from Ref. [31].

Characterizing the decoherence mechanisms as a function of qubit bias demonstrates the advantages of manipulating a charge state physically distant from device substrate impurities. The dephasing of the qubit inherits a fraction of the decay rate and then further increases as sources of spectral noise cause fluctuations in the energy levels of the electron. However, much like how Hahn echo techniques are used to refocus evolution signals in spin ensembles in which the spins all precess with slightly different frequencies, pulse trains can be used to study these pure-dephasing terms. Pulse trains of different rates refocus over different timescales, acting as filters for the noise spectral density which dephases the qubit. For a

sequence of N refocusing pulses, the coherence decays as $e^{-\chi_N(t)}$ with

$$\chi_N(t) = \int \frac{d\omega}{2\pi} S_\omega(\omega) \frac{F_N(\omega t)}{\omega^2},$$

where S_ω is the spectral density of qubit frequency fluctuations and F_N is the filter function. The pulses push the observed dephasing time towards the relaxation limit $2T_1$, with more repetitions allowing only higher-frequency noise sources. Together with the electron's sensitivity to nearby electric fields, it is possible to use the coherence as a function of pulse time to estimate the noise spectral density at a particular frequency. Electrons on neon demonstrate a charge noise environment nearly as quiet as the best measured in semiconductors in the 10 kHz to 1 MHz range [32, 90]. It is likely that high-frequency noise sources beyond this range dominate electron dephasing, such as coupling to other nearby electrons. These stray electrons may also serve as the inconsistent, non-radiative source governing the decay time and causing inconsistencies between otherwise qualitatively similar qubits. Hopefully, further improvements in the neon surface quality and electron control will shed light on these mechanisms. Regardless, these results suggest electrons on neon could also make excellent spin qubits, with spin-orbit coupling facilitating readout with a superconducting resonator [34].

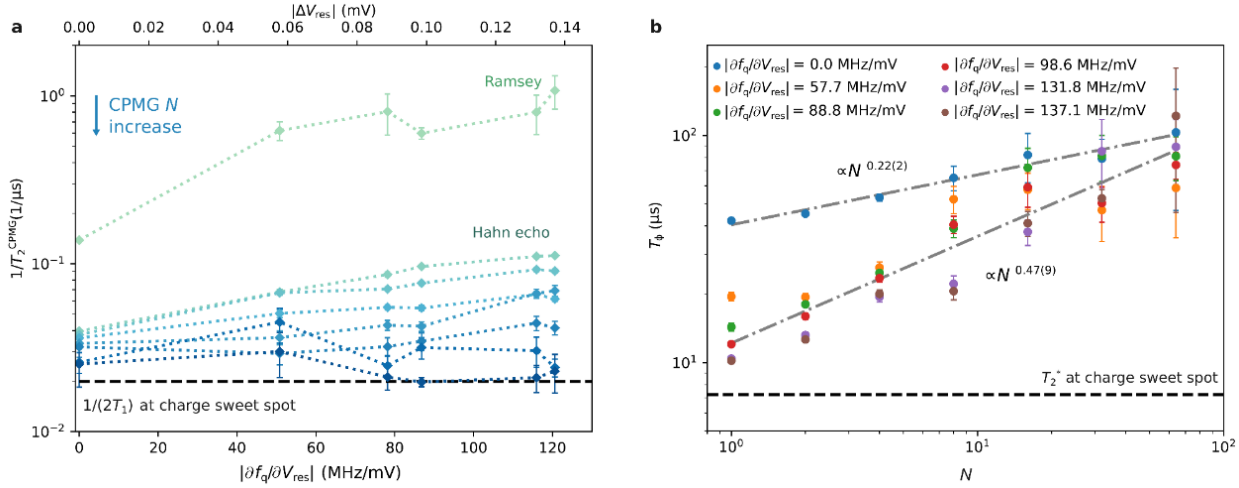


Figure 7.8: Characterization of qubit noise with dynamic decoupling
For this qubit, the dephasing increased with separation from the charge insensitive point of the electron tuning curve. However, at all bias points, the dephasing time increased towards the coherence limit $2T_1$ with refocusing pulses. Reproduced with permission from Springer Nature from Ref. [32].

7.5 Qubit Models

While these electrons have come far as charge qubits already, little is understood about the nature of the underlying system. While spectroscopy reveals some voltage-tunable energy levels of the system, it is not possible to recover an analytic Hamiltonian purely from a subset of eigenvalues. The persistent, linear trajectory in voltage space points towards a one-dimensional representation. If modeled, like TLS often are, as an electron tunneling between two potential wells, then the effective electric field in one dimension is always zero along the path followed by the minima of the qubit frequency. Some proposed mechanisms have been studied more extensively, so for completeness we will discuss these models, though only briefly since none of the models convincingly support the experimental observations.

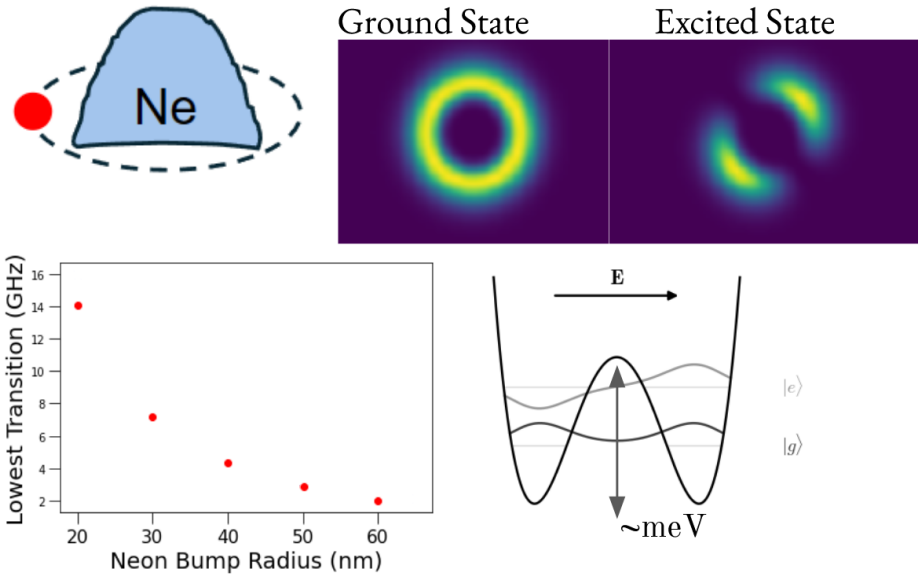


Figure 7.9: Bump-model for a trapped electron
Near an elliptical dielectric defect or in the vicinity of multiple such defects of the same scale, the electron wavefunction can follow a curve equivalent to a one-dimensional representation, similar to the two-site tunneling model used to describe TLS [10].

The roughness of the neon surface presents a few candidates for the neon qubit morphology. The most deliberately studied system these past few years involves the binding of electrons to the perimeter of raised bumps on the neon surface [144, 152]. For a circular neon

bump of radius 15–30 nm, the stable trapping potential extremum for the electron is near the base of the feature, with the image charge setting a trap depth of approximately 1 meV and a transition energy scale in the traditional microwave range. Choosing a coordinate system that follows the bump perimeter, the system maps to one dimension. However, to couple to a microwave resonator via a dipole interaction, the bump must be asymmetric. Similarly, this idea can be extended to clusters of bumps, giving rise to many possible candidates. However, the trap depth is small compared to the scale of electric fields applied in the experiments. Furthermore, a convincing candidate would feature an insensitivity to electric fields along one direction since it is unlikely that all electrons on neon observed so far existed in device locales where two or more bias lever arms could exactly negate one another. That being said, coupling to motion in a direction along the bump nearly perpendicular to the device surface has not been explored as thoroughly as motion confined to two dimensions. The superconducting resonator electric field lines necessarily weaken and are nearly perpendicular close to the electrode surface, satisfying three of the most consistent experimental observations: two bias levers can nearly always facilitate an avoided crossing, the trap depth is effectively larger since the electrostatic field lines are weaker, and the coupling strength is on the weaker end of what one would predict is reasonable with high-impedance resonators. A simple direction would be to imagine electrons trapped in the neon, tunneling across a weak barrier set by discontinuities in the dielectric environment. Some studies have shown evidence that neon and other noble gas solids are porous and trap electrons sourced from a focused emission [153]. While a suitable model has not yet been proposed, there are clearly many avenues to explore in the space of the neon surface morphology.

CHAPTER 8

FUTURE DIRECTIONS AND CONCLUSION

8.1 Spin-Orbit Interaction

While this dissertation has focused on charge states of electrons levitating on helium and neon, there is of course a more fundamental property of the electron that is perhaps of more interest for quantum computation: its spin. While the zero-point energy is split evenly between current and voltage fluctuations in a superconducting resonator, the electric dipole moment of an electron far exceeds its spin magnetic moment. Furthermore, while higher-impedance resonators can be readily produced from high-kinetic-inductance films, the impedance is difficult to decrease with geometric modifications alone, though the growth of low-loss, high-permittivity dielectrics is an active field of research that will contribute significantly towards this end. Coupling directly to the spin is, therefore, challenging. While it is certainly possible to fabricate features of a more appropriate length scale for interacting with the spin directly, a more accessible goal in the near term is to take inspiration from levitated ions and quantum dots and utilize spin-orbit coupling to mediate the spin-resonator interaction [154–156]. In fact, the coupling to the spin through the charge can be made impressively large since the charge coupling can already exceed 100 MHz [28].

Placing micromagnets or a current-carrying nanowire in the vicinity of the trap can produce local magnetic field gradients facilitating spin coupling strengths similar to the charge coupling [22, 26, 149, 157]. The spin-orbit interaction strength can be estimated semi-classically as

$$\hbar g_{so} = \frac{g_e \mu_B}{2} \frac{\partial B_\perp}{\partial x} x_{zpf} \qquad g_s \approx \frac{2 g_{so}\, g_c\, \omega_x}{\omega_x^2 - \omega_L^2}$$

where g_c is the charge-photon coupling and g_s is the resulting spin-photon coupling. On the typical length scales of microchannel geometries, cobalt micromagnets can produce significant

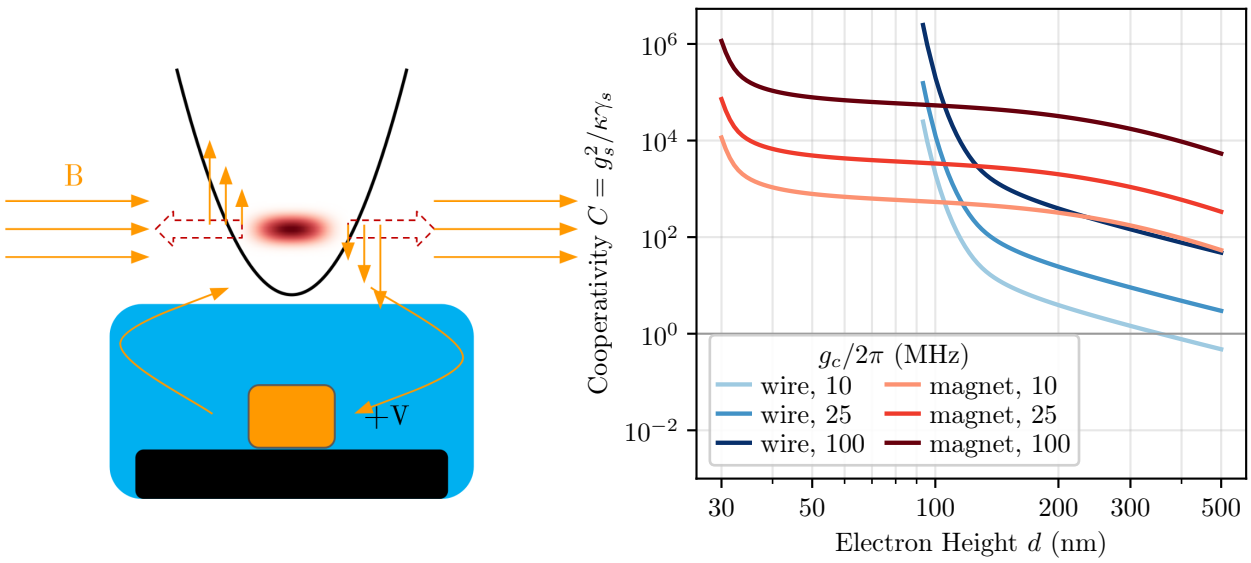


Figure 8.1: Spin-orbit coupling schematic
The cooperativity between the resonator and the spin represents how effectively they interact relative to their decoherence rates and is useful for determining the feasibility of logical operations with the qubit. Detuning the orbital states from the spin states suppresses the decoherence inherited by the spin from the charge, with most of the spin linewidth coming from fluctuations of the Larmor frequency caused by longer-wavelength ripplons displacing the electron vertically. The electron motion might act as a bus for two-qubit gates, and an incoherent bus hurts the gate fidelity. The simulations for this figure assume a 500 × 500 × 100 nm (length, width, height) magnet inside a one-micron-wide channel with bulk cobalt magnetization saturation or a 100 × 100 nm nanowire. The wire dimension can be increased without significantly impacting the cooperativity if it remains narrow relative to the microchannel depth.

magnetic field gradients, and ideally require no fabrication changes to existing devices beyond an additional step for deposition of a ferromagnet like cobalt [158, 159]. For bulk cobalt magnetization saturation and common microchannel geometries, the spin-orbit coupling can be made nearly as strong as the orbital coupling itself. However, cobalt micromagnets often fall short of bulk saturation magnetization at low applied fields, depending sensitively on their geometry. In this case, it is possible to reach the strong coupling limit for resonator-spin interaction without reaching the same for resonator-charge interaction. Another approach is to introduce a current-carrying nanowire which produces the necessary magnetic field gradient [22, 160]. In this case, the gradient is smaller, but the spin-orbit coupling can

be shut off to preserve the spin state. To maximize the current-carrying capacity of the superconducting wire, using nitride metals such as NbN and NbTiN would be ideal.

While the bare spin lifetime can be exceedingly long, in this case it is still not possible to neglect the orbital coherence. Dephasing in the electron motion can facilitate single-photon decay of the spin. Although this effect is suppressed by detuning the electron motion from the spin, this also rapidly reduces the coupling strength, so without improving the orbital coherence, one effectively trades spin coherence for coupling strength. However, the dressed spin lifetime when driven by the charge, even with present orbital state coherence, can approach milliseconds, which would match the current state of the art in superconducting circuits. The largest contribution to the spin's intrinsic linewidth comes from fluctuations in the Larmor frequency due to proximity variation to the micromagnet or nanowire caused by ripplonic excitations of the helium surface [33, 161]. Unlike in the case of the orbital linewidth, however, the frequency fluctuations are $1/f$ noise since the spin states have identical geometric distributions over the ripplon surface, so for ripplons in a helium bath with no geometric boundary conditions, the phase coherence can be refocused. Microchannels could potentially introduce boundary conditions for the ripplons and push the noise into the motional-narrowing limit instead.

8.2 Quantum Computing with Multiple Electrons

Although control of a single electron demonstrates the fundamental physics of the platform, single electrons do not necessarily need to form the basis for quantum computation with electrons on helium. Two-electron configurations are apparently less sensitive to trapping potential asymmetries. Spin-orbit manipulation of electron pairs, drawing inspiration from ion traps, forms the basis for schemes like the Mølmer–Sørensen gate [162, 163]. A key advantage of such an approach is first-order insensitivity of the spin states to fluctuations in the orbital energy levels. Furthermore, for trapped electrons, one can operate the trap

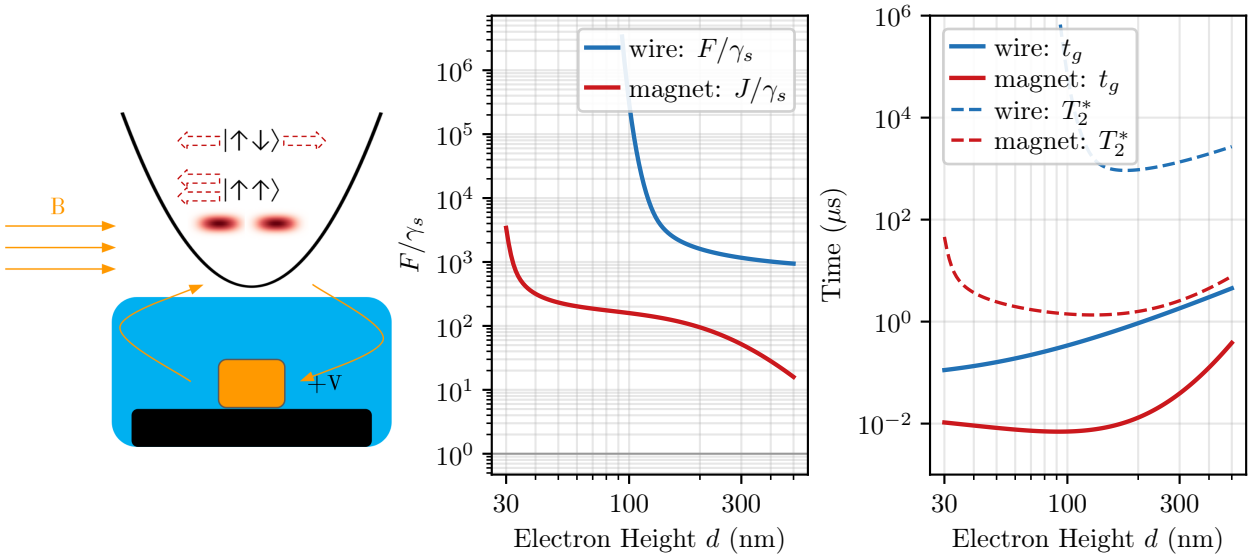


Figure 8.2: Mølmer–Sørensen gate scheme for electrons on helium
In a Mølmer–Sørensen gate for two electron spins on helium, pulsing current through a nearby nanowire produces a spin-dependent force, forming the basis for a geometric phase gate between the electrons. If instead a static magnetic field gradient produced by a micromagnet generates a persistent spin-orbit coupling, virtual exchange of photons between the spins can facilitate an iSWAP gate. These calculations hold similar assumptions to Fig. 8.1 and are performed with an assumed charge-photon coupling strength of 10 MHz.

in both harmonic and anharmonic potential configurations. In the former, the electron pair can be driven harder to artificially increase the spin coupling.

For two electrons in a trap, possible two-qubit gates include Mølmer–Sørensen and exchange interaction approaches. A straightforward realization of the former is to include a current-carrying wire beneath two trapped electrons to introduce the magnetic field gradient necessary for spin-orbit coupling. Applying simultaneous sideband tones at the charge-spin detuning frequency exerts a total spin-dependent force, directly driving the orbital motion when the spins are aligned. After a gate time $t_g = 2\pi/\delta$, where δ is the detuning of the drive tones from the motional sidebands, the orbital state returns to its initial configuration by completing a loop in phase space and is disentangled from the spin, while the spins become entangled with a geometric phase proportional to $(\sigma_x^{(1)} + \sigma_x^{(2)})^2$. If $\delta = 4F$, where F is the spin-dependent force or sideband rate, then $t_g = \pi/2F$. In this approach, at sufficiently low

pressing fields, the orbital motion is a relatively coherent bus and the gate is insensitive to the starting orbital state. The gate is sensitive to slow drift in the orbital frequencies from longer-wavelength ripplons, but creative pulse shaping can reduce the sensitivity to orbital transition noise. The alternating current in the wire can also be switched off, letting the spin states idle coherently.

Utilizing a magnetic field gradient produced by a nearby micromagnet opens the possibility of deeper microchannels than would be possible with a wire since the spin-dependent force becomes significantly greater than with a wire. In this case, it would be natural to utilize a motion-mediated exchange interaction between the spins: near resonance with one another, one spin emits a virtual photon by flipping and the other absorbs it. The spins become charge-like and the orbital modes dispersively shift according to the spin states. Reminiscent of multiple transmons coupled through a bus resonator, the spin qubits are controlled through the orbital motion alone, enabling iSWAP gates. Because the spin is significantly detuned from the motion, it inherits little of the orbital motion's ripplon-induced linewidth, but because the field gradient is stronger in this case, the spin is more sensitive to dephasing due to longer-wavelength ripplons than when using a wire. The spin-orbit coupling is always on, exacerbating the drawback.

8.3 Electron Manipulation on van der Waals Helium Thin Films

Another regime of interest that has not been explored in tandem with superconducting circuits is the control of electrons on thin helium films. Van der Waals forces produce helium thin films with thicknesses on the order of 30 nm. By reducing the thickness of the film by an order of magnitude from the microchannel regime, the coupling strength between an electron and a submerged resonator is similarly increased. Since the linewidth of high-impedance superconducting resonators is often limited by strong interactions with surface TLS, the flexibility to work with a smaller resonator impedance facilitates higher-quality-

factor cavities in these experiments. At this distance, strong spin-orbit interactions can also be created with nanowires rather than micromagnets.

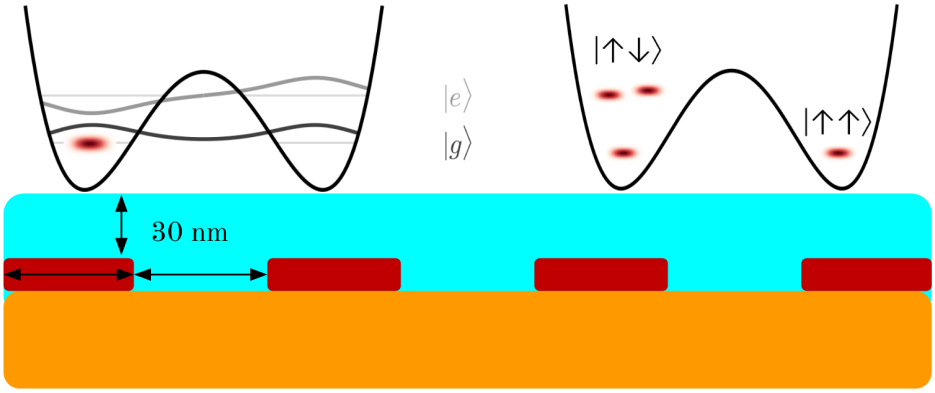


Figure 8.3: Electron control on helium thin films
Electrons on thin helium films are much closer to the electrodes, allowing for higher-aspect-ratio traps and stronger coupling to the electron. Tunneling can form the basis for charge states potentially less sensitive to ripplons. Spin manipulation more similar to that in semiconductor quantum dots may also be accessible.

Manipulating electrons on helium thin films presents unique advantages and challenges. While electron orbital states in helium microchannel devices resemble those of trapped ions, in the case of helium thin films the resemblance shifts towards semiconductor quantum dots. Shuffling electrons effectively requires an electrode pitch on the order of the image-charge screening length of the system, $2h \approx 60$ nm in the case of helium films, relatively straightforward features to produce with electron-beam lithography. At this length scale, tunneling can dictate the orbital state structure rather than the electrostatic trap curvature. This can be preferable since the trap curvature sensitivity in this regime is > 1 GHz/μV while the tunneling state separation sensitivity is > 1 GHz/mV. While reducing the distance to the dielectric substrate certainly harms charge and spin coherence, at this point progress is largely limited by helium film excitations. Tunneling-type orbital states may be significantly less sensitive to ripplon-induced dephasing because the ground and first excited states have similar spatial extents. We have observed states of electrons on helium with linewidths consistent with dephasing induced only by the image charge that, similar to electrons trapped

on solid neon, appeared one-dimensional with significant bias instability. Tunneling of a single electron is one candidate explanation for this data, though definitely not the only one. Proximity to the underlying substrate can also reduce electron mobility, but recent work in single-electron chain manipulation and measurements of the electron mobility on ultrasmooth amorphous metals make this a promising research direction [41, 108]. However, at this length scale, it may also be possible to etch the underlying substrate to create a bandgap in the spectrum of relevant phonon or ripplon excitations. Beyond applications to quantum computing, probing the quantum degenerate regime of a two-dimensional levitating electron gas makes studying novel science typically limited to the field of semiconductors possible with a nearly disorder-free system.

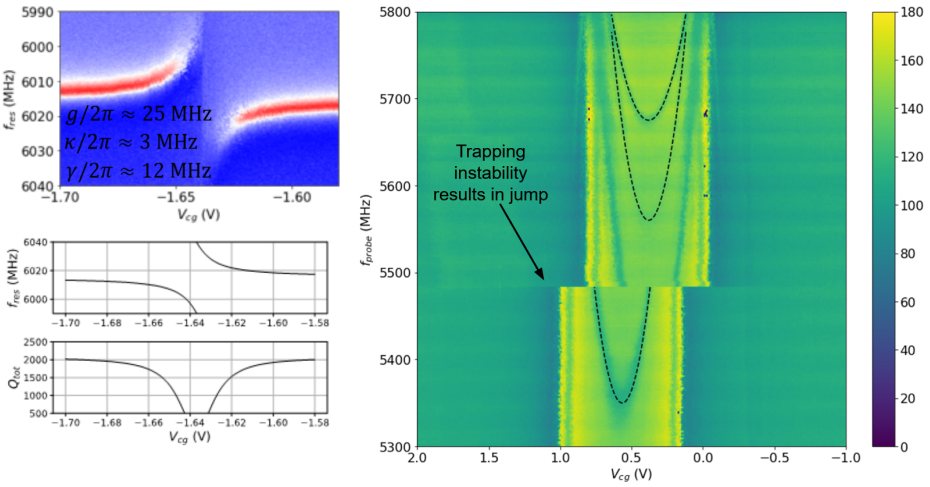


Figure 8.4: Narrower-linewidth charge states of electrons on helium
We have observed electron charge states in devices with helium films with orbital linewidths near the image-charge-associated ripplon floor (left). It is unknown if these signatures were from single electrons or what charge state geometries produced them. The electron trapping was unstable in time, but two-tone spectroscopy did reveal the hallmarks of higher-order transitions (right). This data was acquired with a device similar to device 2 in Appendix B. Similar signatures have also been observed in device 5.

8.4 Conclusion

While the story of electrons on helium in quantum information science began at nearly the same time as that of circuit quantum electrodynamics, only recently have levitating electrons approached the qubit-manipulation stepping stone which has often preceded rapid development in other platforms. The platform faces unique challenges and although it is optimistic to take for granted that it will experience the same growth, it also holds compelling strengths as a system for quantum information science. The electrons float in a nearly ideal dielectric environment, possess multiple properties all suitable as qubits, and different underlying device length scales can shift the system's closest sibling from superconducting circuits to trapped ions or even semiconductor quantum dots. The versatile toolbox of circuit quantum electrodynamics, which has already been utilized in other platforms, integrates exceptionally well with levitating electrons. Because these electrons can straddle the boundaries between other platforms, they could eventually inherit many of their strengths as well. Although the experiments described in this dissertation are still early-life experiments for a platform that was ironically one of the first proposed for quantum information science, they also detail valuable characteristics and considerations for developing the system further. With abundant future research directions, there is likely more story yet to be told about electrons on helium.

APPENDIX A

MODEL FOR COUNTING ELECTRONS

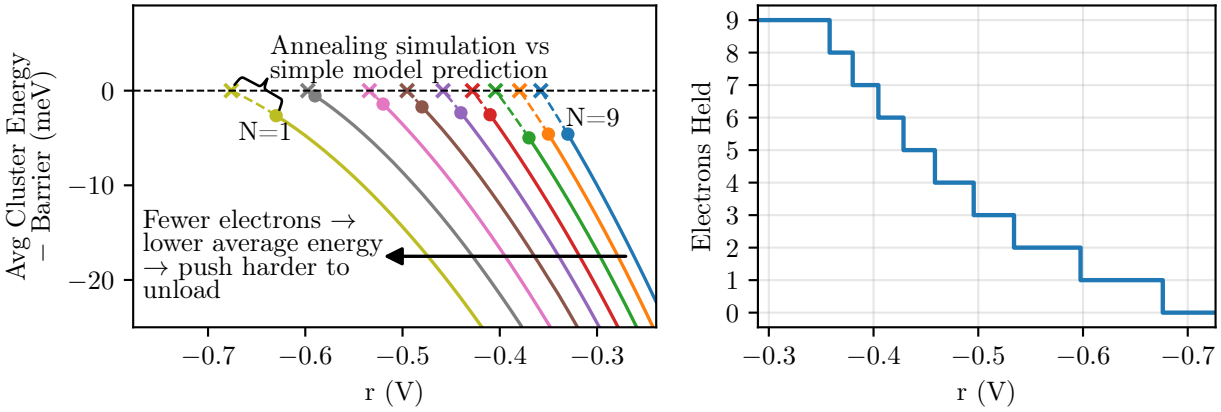


Figure A.1: Simulation of electron unloading
Each colored trace represents the average potential energy of a cluster of electrons as a function of an electrode voltage which reduces the depth of their confining potential well as it is biased more negatively. As the well becomes shallower, single electrons exit the trap.

To model the unloading of electrons from an electrostatic trap, we solve for the equilibrium positions of a cluster of electrons. We use gradient descent to minimize the total energy of the electron cluster, including contributions from their position in the confining potential $U(x_i, y_i)$ and Coulomb interactions $\frac{1}{2}\sum_{i\neq j} C_{ij}$. Some clusters feature metastable configurations, so after convergence criteria are met, we randomly perturb the electron positions with a magnitude consistent with sample temperatures in experiment. When a trap is too shallow to confine N electrons and one exits, it is removed from subsequent position annealing steps in the simulation. These simulations typically see electrons exit the trap slightly before their marginal energy exceeds the trap depth, which is likely a result of FEM meshing artifacts. In experiment, stray electrons, local conductor work function differences, and asymmetries produce different trap unloading curves, so these simulations are primarily useful for design verification.

APPENDIX B

DEVICE GALLERY

In this appendix, we discuss device design philosophies and lessons learned over the course of many experiments. The data presented in this manuscript is sourced from four devices which were a subset of approximately thirty design attempts. So far, only a handful of devices are featured in the body of literature for single-electron manipulation with microwave resonators. Therefore, there are as many lessons learned in devices that disappoint or surprise as there are in devices which produce desirable results. Here, I present a representative gallery of devices designed, fabricated, and measured over the course of my research with brief insights into what we learned, qualitatively, from each device. Since DC-biased electrodes are a key part of these devices, a second gallery for the on-chip filter launchers is also included.

B.1 Devices

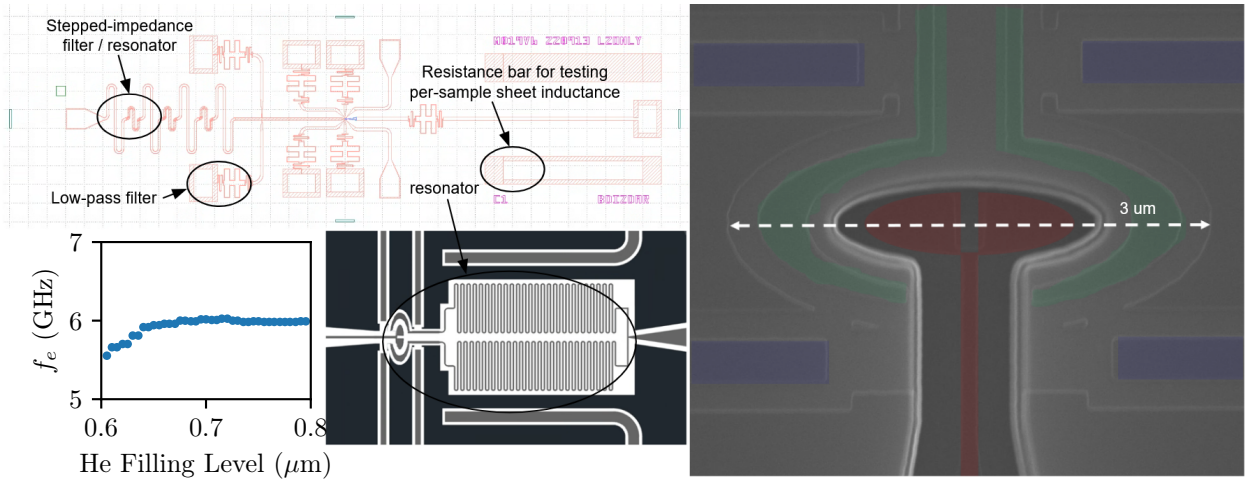


Figure B.1: Early devices: sacrificing trap-flattening for field and ripplon insensitivity The sensitivity of the trapping potential curvature to the electron's height in the microchannel is one of the largest contributions to the electron orbital linewidth. This becomes large when the curvature frequency is decreased by flattening the well into a quartic potential. When the potential well is shallow and more quadratic, the dependence becomes weaker and can vanish at leading order. This device features a > 5 kΩ impedance resonator, a single electrode in the microchannel, and a stepped-impedance or coplanar stripline resonator in the microchannel for detecting reservoir electrons. The large impedance typically resulted in a lossy resonator, especially when multiple fabrication steps and potentially leaky bias lines were added. The stepped-impedance resonator was not effective at detecting or moving electrons in the reservoir to the single-electron trap. It was also difficult to reduce the curvature by reducing the potential depth without losing electrons in the process. While it comes with drawbacks, it is difficult to work without independent curvature knobs.

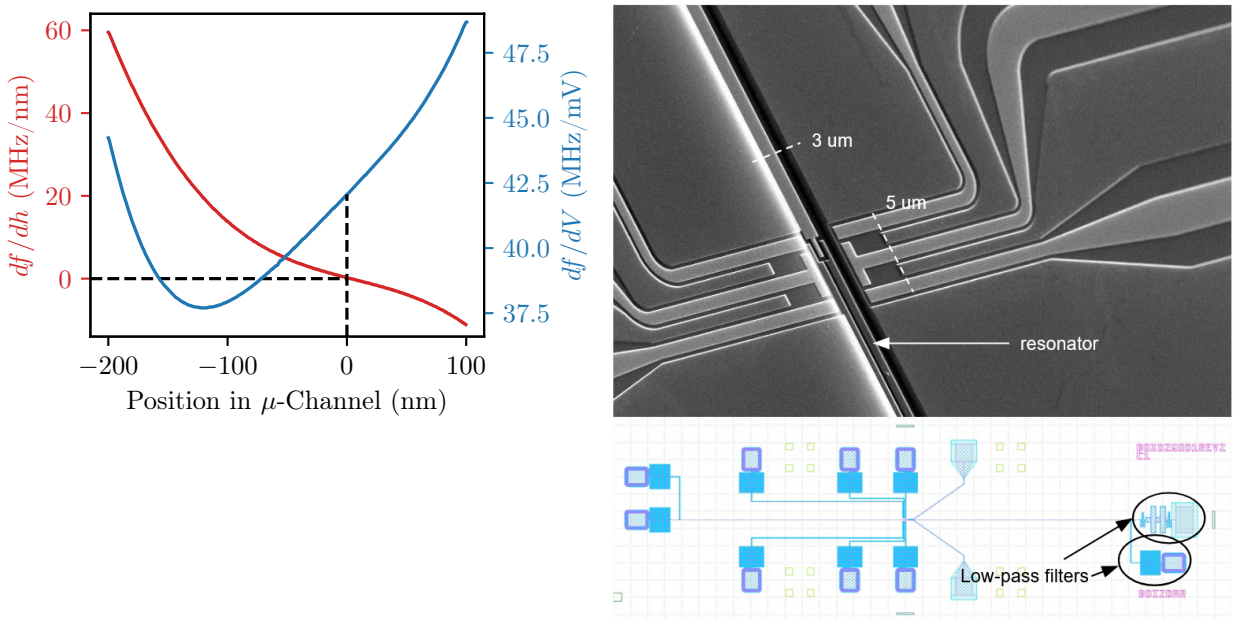


Figure B.2: Change in direction: inspiration by previous works with some compromise In this design, we moved the resonator for coupling to single electrons into the microchannel as in previous experiments and significantly reduced its impedance. However, we still did not appreciate the usefulness of independent curvature knobs. This device was relatively successful. Electrons were trapped and detected easily in the reservoir and could be loaded into and unloaded from the single-electron dot. However, the unloading signals were muddled and inconsistent, perhaps due to excessive ground plane electrons. This device produced strong coupling to an unstable electron(s) charge state, but it was challenging to calibrate two-tone spectroscopy experiments on the stability timescale and prove that it was a single electron. An apparatus failure also ended the experiments prematurely. We also learned that even with thorough cleaning of an etched, smooth silicon surface, high-impedance resonators in microchannels were much lossier than those outside of them. We also faced challenges due to contact potentials between electrodes of different metals.

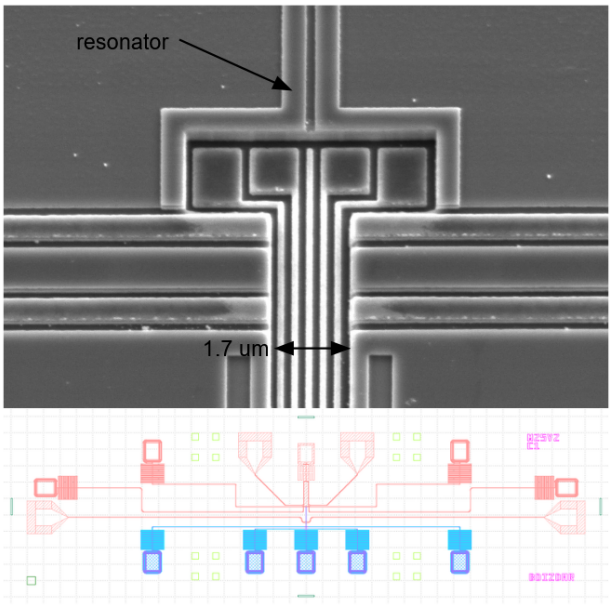


Figure B.3: More successful: maximize the knobs

In this design, many independent knobs to the trap curvature were introduced and the resonator impedance was increased to just before the point where we typically observed rapid increases in loss with further impedance. For our TiN resonators, we found that nanowires narrower than 500 nm resulted in rapid degradation of resonator quality, perhaps due to etch-damaged edges making up a significant portion of the wire cross section. This design was effective at counting and tuning single electrons, but was very sensitive to charge-polluted ground planes, requiring regular 'cleaning' of electrodes to remove stray electrons. In principle, the orbital frequency sensitivity to height fluctuations could be tuned to an insensitive point. Due to an asymmetry that was eventually realized to be a result of a broken bias line cable, the electrons could not be tuned into resonance. After remedying the issue, the device met an untimely demise due to a static discharge incident. We also learned that for lower-temperature superconductors like aluminum, it was less forgiving to lack resistive filtering for the bias lines.

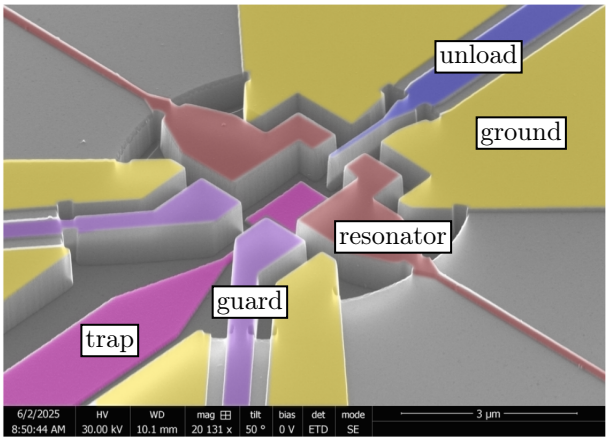


Figure B.4: Collaborator (EeroQ Quantum Hardware) device
A collaborator's design, which had already achieved strong coupling of resonator photons to the orbital states, was used for the Kerr experiments in this dissertation. This design features independent curvature knobs that are planar with the electron, which is made possible with the use of on-device air bridges. The coupling resonator was relatively lossy, consistent with its significant impedance and narrow nanowires.

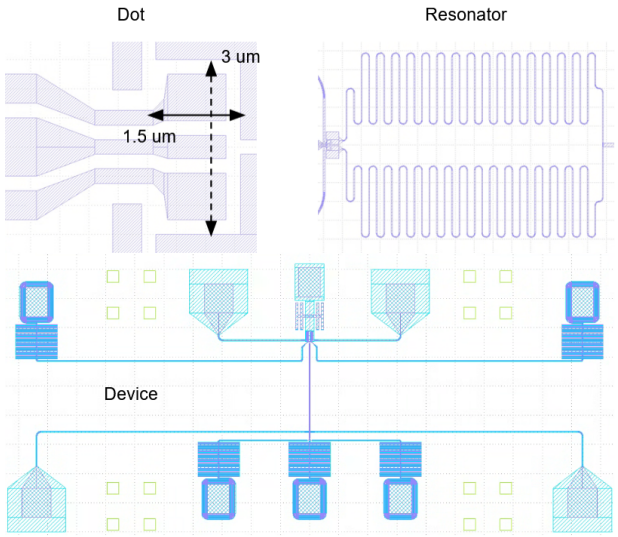


Figure B.5: Sensitivity Improvements
With our previous device, we learned that while significant aspect ratio differences between curvature knobs could reduce sensitivity to helium height fluctuations, it typically increased sensitivity to asymmetry. This device reduced the number of curvature knobs and featured aspect ratios which balanced asymmetry sensitivity with height sensitivity. We also finally realized that a relatively straightforward answer to height sensitivity was to introduce some asymmetry deliberately. While not exactly at the charge sweet spot, for an appropriate amount of asymmetry there is typically a nearby height-insensitive point in bias space. Equipment issues resulted in not having much time with this device.

B.2 On-Chip Filters

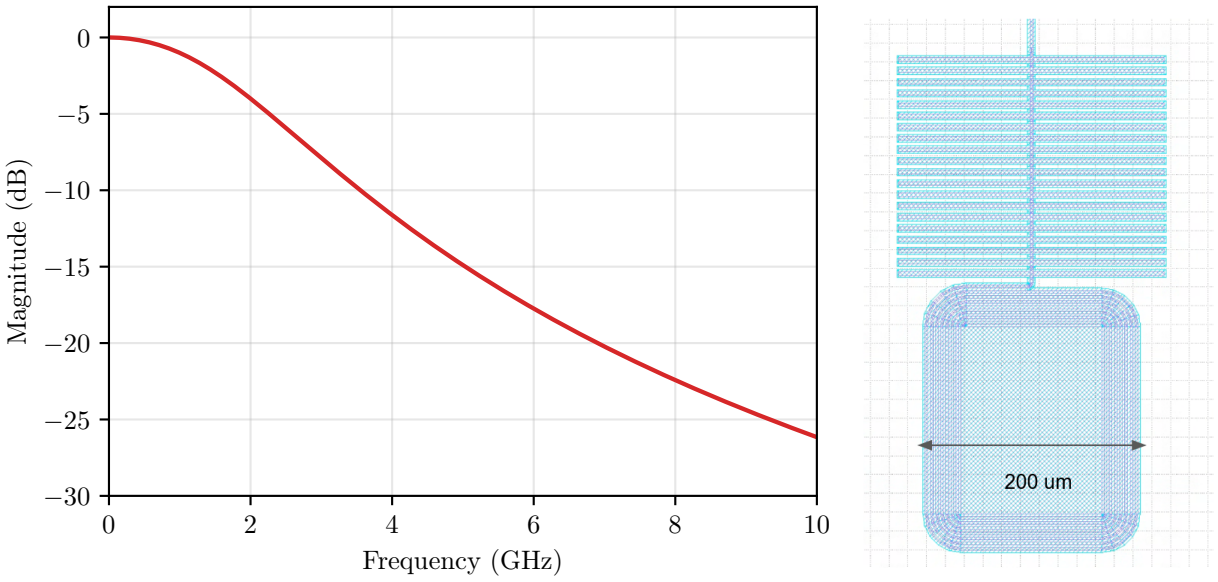


Figure B.6: Filter 1: low-pass with inductive spiral and finger capacitors using Nb/Al Modeled transmission ($L = 2.5$ nH, $C = 4$ pF) from Ref. [98].

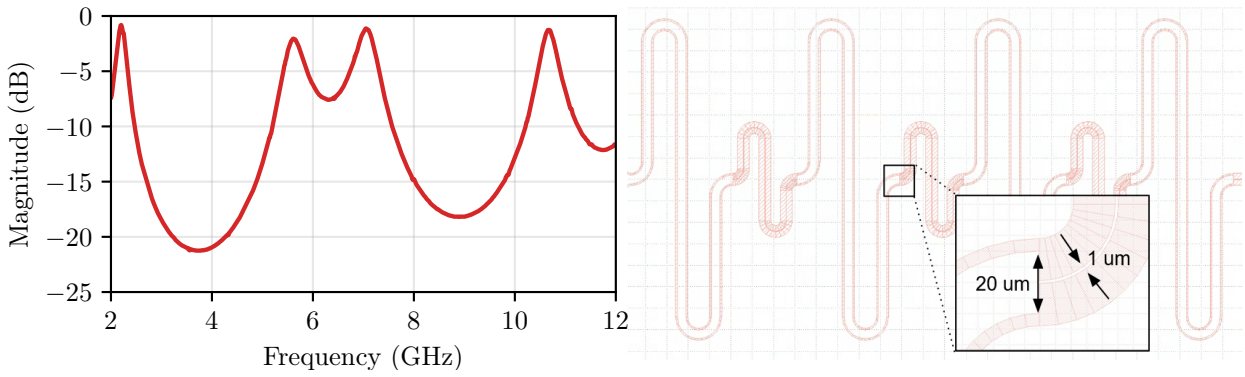


Figure B.7: Filter 2: stepped-impedance waveguide filter using TiN

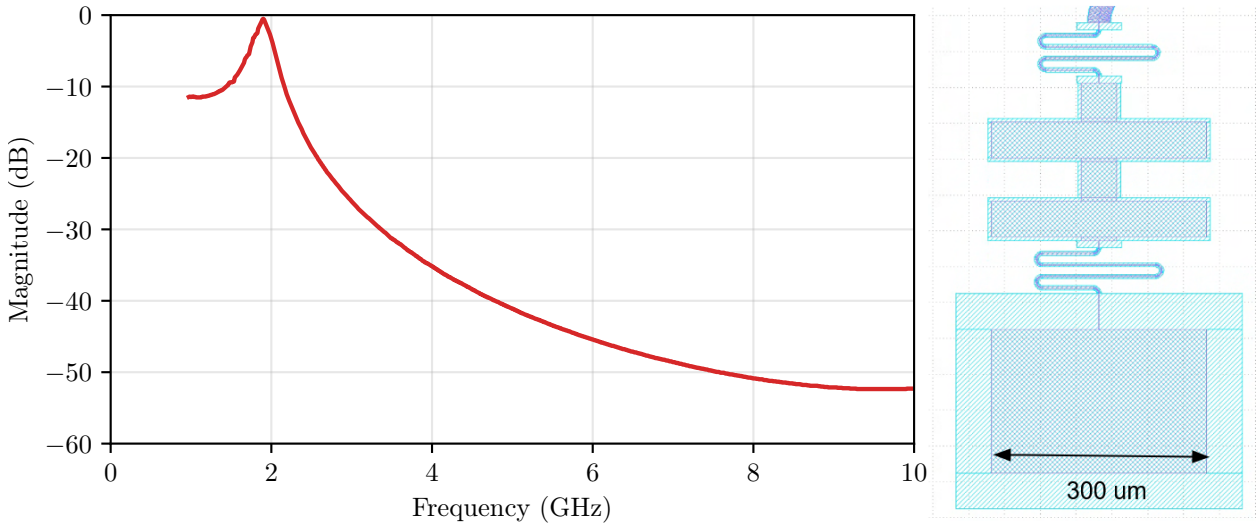


Figure B.8: Filter 3: lumped low-pass using TiN

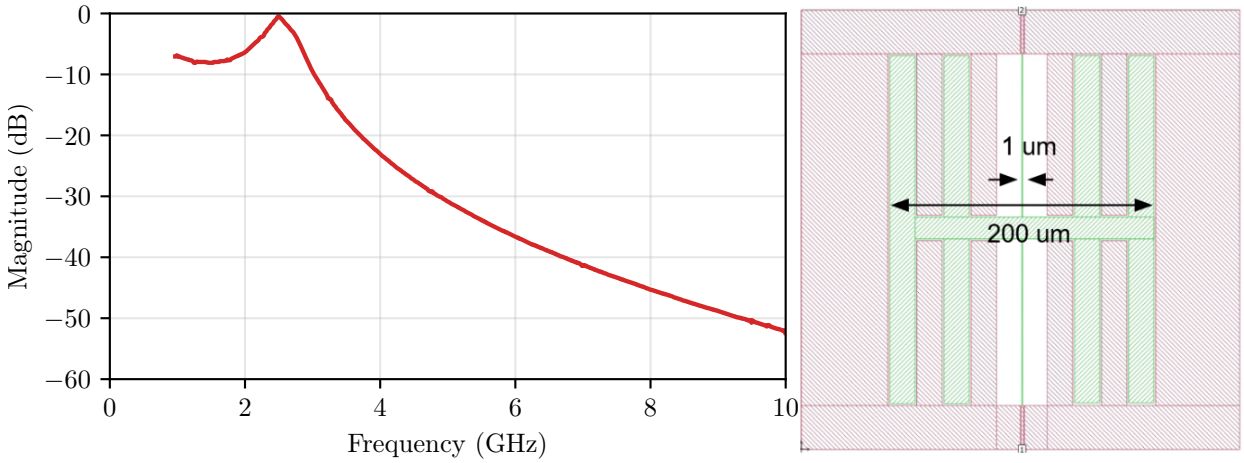


Figure B.9: Filter 4: compact lumped low-pass using TiN

APPENDIX C

DEVICE FABRICATION RECIPES

The devices used throughout this experiment were produced with different fabrication recipes. In this section, we detail the fabrication of one device step by step. However, we also include other relevant processes used for other complete devices, test devices, or other experiments relevant to this work.

C.1 Full Device Recipe

- **ALD of base layer**

    1. Clean polished silicon wafer (Virginia Semiconductor, FZ <111> 2", > 20 kΩ cm) with medium-power sequential sonication, 1 minute each at frequencies 144 kHz and 72 kHz, in toluene, acetone, methanol, IPA, and DI water.
    2. 3-minute dip in Nanostrip 80°C followed by transfer to DI water and swirl 3 minutes and then transfer to another DI water source followed by DI water stream rinse and N_2 dry
    3. Buffered HF solution, room temperature, for 3 minutes followed by two DI water transfers as earlier and N_2 dry
    4. Within 15 minutes, transfer cleaned wafer to loadlock of Fiji G2 ALD system
    5. Deposit 150 cycles (≈15 nm) TiN with TDMAT precursor at 270°C [105]
    6. After deposition, cool sample in load lock for 30 minutes
    7. Sonicate again following earlier procedure with only acetone, IPA, and DI water

- **Alignment Markers**

    1. Spin AZ703 photoresist @ 2000 rpm for 60 seconds, 500 rpm/s spinup and spin-down, for ≈ 1 μm film

2. Bake 1 minute @ 95°C
3. Expose chip-local and global alignment marker pattern with Heidelberg MLA, dose 120 mJ/cm^2
4. Develop 30 s with generous agitation in AZ MIF developer
5. Swirl 30 s in DI water followed by running stream DI water rinse and N_2 dry
6. Etch 4 minutes in SF_6-based chemistry, Plasmatherm ICP, for 1200 nm marker depth
7. Liftoff 4 hours NMP 80°C, followed by acetone/IPA/DI water sonication clean

- **Microchannels**

1. Spin AR-P6200.18 e-beam resist at 2000 rpm, 500 rpm/s.
2. Bake at 150°C for 1 minute
3. Expose microchannel pattern (Raith EBPG-5200+), dose 550 μC/cm^2 with custom numeric PEC
4. Develop 60 s in amyl acetate 2°C, gentle agitation
5. Rinse gently 60 s IPA and N_2 dry
6. Etch in earlier fluorine-based recipe for 750 nm etch depth
7. Resist liftoff and shortened (acetone/IPA/DI) solvent clean as described earlier

- **Deposit non-KI material electrodes**

1. Spin AR-P6200.09 e-beam resist at 2000 rpm, 500 rpm/s.
2. Bake 150°C for 1 minute
3. Expose electrode pattern (Raith EBPG-5200+), dose 380 μC/cm^2 with custom numeric PEC

4. Develop 60 s in amyl acetate 2°C, gentle agitation
5. Rinse gently 60 s IPA and N_2 dry
6. Deposit via evaporation Al (or Nb, more challenging) at 5 Å/s
7. Liftoff 4 hours NMP 80°C followed by gentle stream of NMP to agitate
8. Shortened solvent clean (acetone/IPA/DI) with typical sonication at low power (use of full solvent clean may result in damage of small features due to surface tension changes)

- **Etching of small features**

1. Spin AR-P6200.04 e-beam resist at 2000 rpm, 500 rpm/s.
2. Bake 150°C for 1 minute
3. Expose electrode pattern (Raith EBPG-5200+), dose 280 μC/cm^2 with custom numeric PEC
4. Develop very gently 60 s in amyl acetate 2°C
5. Rinse gently 60 s IPA and N_2 dry
6. Etch in fluorine-based chemistry for 15 seconds
7. Liftoff 4 hours NMP 80°C
8. Shortened solvent clean (acetone/IPA/DI) with typical sonication at low power (use of full solvent clean may result in damage of small features due to surface tension changes)

- **Overetching to prevent electrical breakdown**

1. Repeat previous etching step to increase the inter-electrode etch depth

C.2 Additional Recipes

- **Chlorine-based etch recipes:** Chlorine-based recipes can provide silicon etches which do not fluorinate metal surfaces with etch-resistant polymers. An effective and anisotropic chemistry for etching silicon, TiN, and Nb uses HBr, Cl_2, and O_2. Our apparent optimal parameters for etch rate and an anisotropic etch were 50:20:3 and 50:3:3, respectively at 200 W RF power and 50 V DC bias. This chemistry is ineffective at etching silicon oxides, and must be preceded with a 700 W Cl_2-based etch for 5–10 s. The downside to the chemistry is that for deeper microchannels, the heavy Br ions cause redeposition of silicon oxides in the channel, resulting in micropillars.

- **CSAR Resist Profiles:** ARP-6200.09 and ARP-6200.13 are both suitable for evaporative deposition. The choice of CSAR resist corresponds to the written feature size. Positive features narrower than approximately half the resist height tend to collapse. Negative features are more forgiving, but if written over long distances often result in undeveloped sections which lead to shorts. ARP-6200.18 and occasionally ARP-6200.13 can form post-development fractures at the ends of millimeters-long features, which can often be mitigated by broadly rounding the corners of features. The resist profile also changes near the borders of the microchannels, typically thinning rapidly.

APPENDIX D

EQUIPMENT CATALOGUE

Table D.1: Equipment catalogue

Equipment	**Notes**
Corning Gilbert 0119-783-1 hermetic SMP feedthrough	Carries microwave and DC signals through the sample cell lid while keeping the cell superfluid-leak-tight.
Rosenberger 19K106-K00L5 SMP bullet adapter	Connects lid feedthroughs to PCB connectors. Tolerate some axial misalignment between the lid and the PCB.
Rosenberger 19S101-40ML5 SMP PCB connector	Surface-mount connector joining the bullet adapters to the PCB transmission lines.
Arlon AD1000 PCB laminate	Dielectric for the sample PCB. The dielectric constant is close to that of sapphire or silicon.
Indium wire (0.030" diameter)	Superfluid-tight seals of the sample cell.
Stainless steel capillary (1/16" OD, 0.020" ID)	Carries helium into the sample cell.
Model Power No. 153/157 light bulbs	Tungsten filaments used as the electron source.
GE varnish	Mounts the chip to the PCB.
Silver paint	Alternative adhesive for mounting the chip.
Apiezon N cryogenic vacuum grease	Indium seal grease.
Bluefors LD250 dilution refrigerator	Cools the sample cell to a base temperature of $\sim$20 mK.
AMD (Xilinx) Zynq UltraScale+ RFSoC ZCU216	Generates and digitizes the microwave control and readout signals.

Table D.1: Equipment catalogue (continued)

Equipment	**Notes**
Quantum Machines QDAC-II	Low-noise DC bias source.
Berkeley Nucleonics (BNC) 645 AWG	Pulses the filament.
Low Noise Factory LNF-LNC4_8F HEMT amplifier	Cryogenic amplification of the readout signal.
Low Noise Factory LNF-CIC4_8A single-junction circulator	Isolates the experiment output signal chain from room-temperature noise.
KRYTAR 4020080 180° hybrid	Splits or combines signals into differential and common modes.
Nord Cryo Therma Filter Box	Low-frequency cryogenic filtering of DC lines.
Custom cryogenic low-pass filter	Lumped-element series RC filter with waveguides potted in Eccosorb.

REFERENCES

[1] P. M. Platzman and M. I. Dykman. Quantum computing with electrons floating on liquid helium. *Science*, 284:1967, 1999. doi:10.1126/science.284.5422.1967.

[2] Yu. P. Monarkha and K. Kono. *Two-Dimensional Coulomb Liquids and Solids*. Springer, Berlin, 2004.

[3] W. T. Sommer. Liquid helium as a barrier to electrons. *Phys. Rev. Lett.*, 12:271, 1964. doi:10.1103/PhysRevLett.12.271.

[4] M. W. Cole and M. H. Cohen. Image-potential-induced surface bands in insulators. *Phys. Rev. Lett.*, 23:1238, 1969. doi:10.1103/PhysRevLett.23.1238.

[5] R. J. Donnelly and C. F. Barenghi. The observed properties of liquid helium at the saturated vapor pressure. *J. Phys. Chem. Ref. Data*, 27:1217, 1998. doi:10.1063/1.556028.

[6] C. C. Grimes and T. R. Brown. Direct spectroscopic observation of electrons in image-potential states outside liquid helium. *Phys. Rev. Lett.*, 32:280, 1974. doi:10.1103/PhysRevLett.32.280.

[7] M. W. Cole. Properties of image-potential-induced surface states of insulators. *Phys. Rev. B*, 2:4239, 1970. doi:10.1103/PhysRevB.2.4239.

[8] P. Leiderer. Surface electrons on solid quantum substrates: A brief review. *J. Low Temp. Phys.*, 219:262, 2025. doi:10.1007/s10909-025-03286-3.

[9] A. M. Troyanovskii, A. P. Volodin, and M. S. Khaikin. Electron localization over the surface of crystalline hydrogen and neon. *JETP Lett.*, 29:382, 1979.

[10] T. Kanai, D. Jin, and W. Guo. Single-electron qubits based on quantum ring states on solid neon surface. *Phys. Rev. Lett.*, 132:250603, 2024. doi:10.1103/PhysRevLett.132.250603.

[11] W. Paul. Electromagnetic traps for charged and neutral particles. *Rev. Mod. Phys.*, 62:531, 1990. doi:10.1103/RevModPhys.62.531.

[12] T. Ando, A. B. Fowler, and F. Stern. Electronic properties of two-dimensional systems. *Rev. Mod. Phys.*, 54:437, 1982. doi:10.1103/RevModPhys.54.437.

[13] W. T. Sommer and D. J. Tanner. Mobility of electrons on the surface of liquid ^{4}He. *Phys. Rev. Lett.*, 27:1345, 1971. doi:10.1103/PhysRevLett.27.1345.

[14] V. B. Shikin and Yu. P. Monarkha. On the interaction of surface electrons in liquid helium with oscillations of the vapor-liquid interface. *J. Low Temp. Phys.*, 16:193, 1974. doi:10.1007/BF00655867.

[15] E. Wigner. On the interaction of electrons in metals. *Phys. Rev.*, 46:1002, 1934. doi:10.1103/PhysRev.46.1002.

[16] C. C. Grimes and G. Adams. Evidence for a liquid-to-crystal phase transition in a classical, two-dimensional sheet of electrons. *Phys. Rev. Lett.*, 42:795, 1979. doi:10.1103/PhysRevLett.42.795.

[17] K. von Klitzing, G. Dorda, and M. Pepper. New method for high-accuracy determination of the fine-structure constant based on quantized Hall resistance. *Phys. Rev. Lett.*, 45:494, 1980. doi:10.1103/PhysRevLett.45.494.

[18] L. P. Gor'kov and D. M. Chernikova. Concerning the structure of a charged surface of liquid helium. *JETP Lett.*, 18:68, 1973.

[19] F. M. Peeters and P. M. Platzman. Electrons on films of helium: A quantum mechanical two-dimensional fermion system. *Phys. Rev. Lett.*, 50:2021, 1983. doi:10.1103/PhysRevLett.50.2021.

[20] M. I. Dykman, P. M. Platzman, and P. Seddighrad. Qubits with electrons on liquid helium. *Phys. Rev. B*, 67:155402, 2003. doi:10.1103/PhysRevB.67.155402.

[21] S. A. Lyon. Spin-based quantum computing using electrons on liquid helium. *Phys. Rev. A*, 74:052338, 2006. doi:10.1103/PhysRevA.74.052338.

[22] D. I. Schuster, A. Fragner, M. I. Dykman, S. A. Lyon, and R. J. Schoelkopf. Proposal for manipulating and detecting spin and orbital states of trapped electrons on helium using cavity quantum electrodynamics. *Phys. Rev. Lett.*, 105:040503, 2010. doi:10.1103/PhysRevLett.105.040503.

[23] Y. Nakamura, Yu. A. Pashkin, and J. S. Tsai. Coherent control of macroscopic quantum states in a single-Cooper-pair box. *Nature*, 398:786, 1999. doi:10.1038/19718.

[24] G. Papageorgiou, P. Glasson, K. Harrabi, V. Antonov, E. Collin, P. Fozooni, P. G. Frayne, M. J. Lea, D. G. Rees, and Y. Mukharsky. Counting individual trapped electrons on liquid helium. *Appl. Phys. Lett.*, 86:153106, 2005. doi:10.1063/1.1900301.

[25] E. Rousseau, D. Ponarin, L. Hristakos, O. Avenel, E. Varoquaux, and Yu. Mukharsky. Addition spectra of Wigner islands of electrons on superfluid helium. *Phys. Rev. B*, 79:045406, 2009. doi:10.1103/PhysRevB.79.045406.

[26] E. Kawakami, J. Chen, M. Benito, and D. Konstantinov. Blueprint for quantum computing using electrons on helium. *Phys. Rev. Appl.*, 20:054022, 2023. doi:10.1103/PhysRevApplied.20.054022.

[27] X. Zhou, G. Koolstra, X. Zhang, G. Yang, X. Han, B. Dizdar, X. Li, R. Divan, W. Guo, K. W. Murch, D. I. Schuster, and D. Jin. Single electrons on solid neon as a solid-state qubit platform. *Nature*, 605:46, 2022. doi:10.1038/s41586-022-04539-x.

[28] G. Koolstra, E. O. Glen, N. R. Beysengulov, H. Byeon, K. E. Castoria, M. Sammon, S. A. Lyon, D. G. Rees, and J. Pollanen. Strong coupling of a microwave photon to an electron on helium. *Nat. Phys.*, 22:1293, 2026. doi:10.1038/s41567-026-03342-z.

[29] G. Koolstra, G. Yang, and D. I. Schuster. Coupling a single electron on superfluid helium to a superconducting resonator. *Nat. Commun.*, 10:5323, 2019. doi:10.1038/s41467-019-13335-7.

[30] E. Kawakami, A. Elarabi, and D. Konstantinov. Image-charge detection of the Rydberg states of surface electrons on liquid helium. *Phys. Rev. Lett.*, 123:086801, 2019. doi:10.1103/PhysRevLett.123.086801.

[31] X. Zhou, X. Li, Q. Chen, G. Koolstra, G. Yang, B. Dizdar, Y. Huang, C. S. Wang, X. Han, X. Zhang, D. I. Schuster, and D. Jin. Electron charge qubit with 0.1 millisecond coherence time. *Nat. Phys.*, 20:116, 2024. doi:10.1038/s41567-023-02247-5.

[32] X. Li, C. S. Wang, B. Dizdar, Y. Huang, Y. Wen, W. Guo, X. Zhang, X. Han, X. Zhou, and D. Jin. Solid neon as a noise-resilient host for electron qubits above 100 mK. *Nat. Electron.*, 9:621, 2026. doi:10.1038/s41928-026-01613-4.

[33] M. I. Dykman, O. Asban, Q. Chen, D. Jin, and S. A. Lyon. Spin dynamics in quantum dots on liquid helium. *Phys. Rev. B*, 107:035437, 2023. doi:10.1103/PhysRevB.107.035437.

[34] Q. Chen, I. Martin, L. Jiang, and D. Jin. Electron spin coherence on a solid neon surface, 2022. arXiv:2205.00589.

[35] M. I. Dykman and J. Pollanen. Electrons in quantum dots on helium: From charge qubits to synthetic color centers. *Entropy*, 27:787, 2025. doi:10.3390/e27080787.

[36] D. Wineland, P. Ekstrom, and H. Dehmelt. Monoelectron oscillator. *Phys. Rev. Lett.*, 31:1279, 1973. doi:10.1103/PhysRevLett.31.1279.

[37] L. S. Brown and G. Gabrielse. Geonium theory: Physics of a single electron or ion in a Penning trap. *Rev. Mod. Phys.*, 58:233, 1986. doi:10.1103/RevModPhys.58.233.

[38] C. Matthiesen, Q. Yu, J. Guo, A. M. Alonso, and H. Häffner. Trapping electrons in a room-temperature microwave Paul trap. *Phys. Rev. X*, 11:011019, 2021. doi:10.1103/PhysRevX.11.011019.

[39] H. Byeon, K. Nasyedkin, J. R. Lane, N. R. Beysengulov, L. Zhang, R. Loloee, and J. Pollanen. Piezoacoustics for precision control of electrons floating on helium. *Nat. Commun.*, 12:4150, 2021. doi:10.1038/s41467-021-24452-7.

[40] C. A. Mikolas, N. R. Beysengulov, A. J. Schleusner, D. G. Rees, C. Undershute, and J. Pollanen. Plasmon mode engineering with electrons on helium. *Nat. Commun.*, 16: 4959, 2025. doi:10.1038/s41467-025-60305-3.

[41] K. E. Castoria, H. Byeon, N. R. Beysengulov, E. O. Glen, M. Sammon, J. Pollanen, D. G. Rees, and S. A. Lyon. Selective shuttling of electrons on helium using a CMOS control platform, 2025. arXiv:2511.15922.

[42] M. H. Devoret and R. J. Schoelkopf. Superconducting circuits for quantum information: An outlook. *Science*, 339:1169, 2013. doi:10.1126/science.1231930.

[43] P. Krantz, M. Kjaergaard, F. Yan, T. P. Orlando, S. Gustavsson, and W. D. Oliver. A quantum engineer's guide to superconducting qubits. *Appl. Phys. Rev.*, 6:021318, 2019. doi:10.1063/1.5089550.

[44] A. P. M. Place, L. V. H. Rodgers, P. Mundada, B. M. Smitham, M. Fitzpatrick, Z. Leng, A. Premkumar, J. Bryon, A. Vrajitoarea, S. Sussman, G. Cheng, T. Madhavan, H. K. Babla, X. H. Le, Y. Gang, B. Jäck, A. Gyenis, N. Yao, R. J. Cava, N. P. de Leon, and A. A. Houck. New material platform for superconducting transmon qubits with coherence times exceeding 0.3 milliseconds. *Nat. Commun.*, 12:1779, 2021. doi:10.1038/s41467-021-22030-5.

[45] C. Wang, X. Li, H. Xu, Z. Li, J. Wang, Z. Yang, Z. Mi, X. Liang, T. Su, C. Yang, G. Wang, W. Wang, Y. Li, M. Chen, C. Li, K. Linghu, J. Han, Y. Zhang, Y. Feng, Y. Song, T. Ma, J. Zhang, R. Wang, P. Zhao, W. Liu, G. Xue, Y. Jin, and H. Yu. Towards practical quantum computers: Transmon qubit with a lifetime approaching 0.5 milliseconds. *npj Quantum Inf.*, 8:3, 2022. doi:10.1038/s41534-021-00510-2.

[46] A. Somoroff, Q. Ficheux, R. A. Mencia, H. Xiong, R. Kuzmin, and V. E. Manucharyan. Millisecond coherence in a superconducting qubit. *Phys. Rev. Lett.*, 130:267001, 2023. doi:10.1103/PhysRevLett.130.267001.

[47] M. Bland, F. Bahrami, J. Martinez, P. Prestegaard, B. M. Smitham, A. Joshi, E. Hedrick, A. Pakpour-Tabrizi, S. Kumar, A. Jindal, R. Chang, A. Yang, G. Cheng, N. Yao, R. Cava, N. P. de Leon, and A. A. Houck. Millisecond lifetimes and coherence times in 2D transmon qubits. *Nature*, 647:343, 2025. doi:10.1038/s41586-025-09687-4.

[48] Google Quantum AI and Collaborators. Quantum error correction below the surface code threshold. *Nature*, 638:920, 2025. doi:10.1038/s41586-024-08449-y.

[49] A. Blais, R.-S. Huang, A. Wallraff, S. M. Girvin, and R. J. Schoelkopf. Cavity quantum electrodynamics for superconducting electrical circuits: An architecture for quantum computation. *Phys. Rev. A*, 69:062320, 2004. doi:10.1103/PhysRevA.69.062320.

[50] A. Blais, A. L. Grimsmo, S. M. Girvin, and A. Wallraff. Circuit quantum electrodynamics. *Rev. Mod. Phys.*, 93:025005, 2021. doi:10.1103/RevModPhys.93.025005.

[51] D. P. DiVincenzo. The physical implementation of quantum computation. *Fortschr. Phys.*, 48:771, 2000. doi:10.1002/1521-3978(200009)48:9/11<771::AID-PROP771>3.0.CO;2-E.

[52] B. M. Terhal. Quantum error correction for quantum memories. *Rev. Mod. Phys.*, 87: 307, 2015. doi:10.1103/RevModPhys.87.307.

[53] E. Knill, D. Leibfried, R. Reichle, J. Britton, R. B. Blakestad, J. D. Jost, C. Langer, R. Ozeri, S. Seidelin, and D. J. Wineland. Randomized benchmarking of quantum gates. *Phys. Rev. A*, 77:012307, 2008. doi:10.1103/PhysRevA.77.012307.

[54] R. Blume-Kohout, J. K. Gamble, E. Nielsen, K. Rudinger, J. Mizrahi, K. Fortier, and P. Maunz. Demonstration of qubit operations below a rigorous fault tolerance threshold with gate set tomography. *Nat. Commun.*, 8:14485, 2017. doi:10.1038/ncomms14485.

[55] C. D. Wilen, S. Abdullah, N. A. Kurinsky, C. Stanford, L. Cardani, G. D'Imperio, C. Tomei, L. Faoro, L. B. Ioffe, C. H. Liu, A. Opremcak, B. G. Christensen, J. L. DuBois, and R. McDermott. Correlated charge noise and relaxation errors in superconducting qubits. *Nature*, 594:369, 2021. doi:10.1038/s41586-021-03557-5.

[56] A. G. Fowler, M. Mariantoni, J. M. Martinis, and A. N. Cleland. Surface codes: Towards practical large-scale quantum computation. *Phys. Rev. A*, 86:032324, 2012. doi:10.1103/PhysRevA.86.032324.

[57] E. M. Purcell. Spontaneous emission probabilities at radio frequencies. *Phys. Rev.*, 69: 681, 1946.

[58] D. Kleppner. Inhibited spontaneous emission. *Phys. Rev. Lett.*, 47:233, 1981. doi:10.1103/PhysRevLett.47.233.

[59] A. A. Houck, J. A. Schreier, B. R. Johnson, J. M. Chow, J. Koch, J. M. Gambetta, D. I. Schuster, L. Frunzio, M. H. Devoret, S. M. Girvin, and R. J. Schoelkopf. Controlling the spontaneous emission of a superconducting transmon qubit. *Phys. Rev. Lett.*, 101: 080502, 2008. doi:10.1103/PhysRevLett.101.080502.

[60] A. A. Fragner. *Circuit Quantum Electrodynamics with Electrons on Helium.* PhD thesis, Yale University, New Haven, Connecticut, 2013.

[61] S. Kotler, R. W. Simmonds, D. Leibfried, and D. J. Wineland. Hybrid quantum systems with trapped charged particles. *Phys. Rev. A*, 95:022327, 2017. doi:10.1103/PhysRevA.95.022327.

[62] A. A. Clerk, K. W. Lehnert, P. Bertet, J. R. Petta, and Y. Nakamura. Hybrid quantum systems with circuit quantum electrodynamics. *Nat. Phys.*, 16:257, 2020. doi:10.1038/s41567-020-0797-9.

[63] J. T. Muhonen, J. P. Dehollain, A. Laucht, F. E. Hudson, R. Kalra, T. Sekiguchi, K. M. Itoh, D. N. Jamieson, J. C. McCallum, A. S. Dzurak, and A. Morello. Storing quantum information for 30 seconds in a nanoelectronic device. *Nat. Nanotechnol.*, 9: 986, 2014. doi:10.1038/nnano.2014.211.

[64] P. Wang, C.-Y. Luan, M. Qiao, M. Um, J. Zhang, Y. Wang, X. Yuan, M. Gu, J. Zhang, and K. Kim. Single ion qubit with estimated coherence time exceeding one hour. *Nat. Commun.*, 12:233, 2021. doi:10.1038/s41467-020-20330-w.

[65] R. J. Glauber. The quantum theory of optical coherence. *Phys. Rev.*, 130:2529, 1963. doi:10.1103/PhysRev.130.2529.

[66] B. Yurke and J. S. Denker. Quantum network theory. *Phys. Rev. A*, 29:1419, 1984. doi:10.1103/PhysRevA.29.1419.

[67] M. H. Devoret. Quantum fluctuations in electrical circuits. In S. Reynaud, E. Giacobino, and J. Zinn-Justin, editors, *Quantum Fluctuations, Les Houches Session LXIII*, page 351. Elsevier, Amsterdam, 1997.

[68] D. I. Schuster. *Circuit Quantum Electrodynamics*. PhD thesis, Yale University, New Haven, Connecticut, 2007.

[69] S. Ganjam, Y. Wang, Y. Lu, A. Banerjee, C. U. Lei, L. Krayzman, K. Kisslinger, C. Zhou, R. Li, Y. Jia, M. Liu, L. Frunzio, and R. J. Schoelkopf. Surpassing millisecond coherence in on chip superconducting quantum memories by optimizing materials and circuit design. *Nat. Commun.*, 15:3687, 2024. doi:10.1038/s41467-024-47857-6.

[70] A. Wallraff, D. I. Schuster, A. Blais, L. Frunzio, R.-S. Huang, J. Majer, S. Kumar, S. M. Girvin, and R. J. Schoelkopf. Strong coupling of a single photon to a superconducting qubit using circuit quantum electrodynamics. *Nature*, 431:162, 2004. doi:10.1038/nature02851.

[71] S. Bravyi, D. P. DiVincenzo, and D. Loss. Schrieffer–Wolff transformation for quantum many-body systems. *Ann. Phys.*, 326:2793, 2011. doi:10.1016/j.aop.2011.06.004.

[72] A. Wallraff, D. I. Schuster, A. Blais, L. Frunzio, J. Majer, M. H. Devoret, S. M. Girvin, and R. J. Schoelkopf. Approaching unit visibility for control of a superconducting qubit with dispersive readout. *Phys. Rev. Lett.*, 95:060501, 2005. doi:10.1103/PhysRevLett.95.060501.

[73] R. Vijay, D. H. Slichter, and I. Siddiqi. Observation of quantum jumps in a superconducting artificial atom. *Phys. Rev. Lett.*, 106:110502, 2011. doi:10.1103/PhysRevLett.106.110502.

[74] F. Motzoi, J. M. Gambetta, P. Rebentrost, and F. K. Wilhelm. Simple pulses for elimination of leakage in weakly nonlinear qubits. *Phys. Rev. Lett.*, 103:110501, 2009. doi:10.1103/PhysRevLett.103.110501.

[75] G. Lindblad. On the generators of quantum dynamical semigroups. *Commun. Math. Phys.*, 48:119, 1976. doi:10.1007/BF01608499.

[76] J. Koch, T. M. Yu, J. Gambetta, A. A. Houck, D. I. Schuster, J. Majer, A. Blais, M. H. Devoret, S. M. Girvin, and R. J. Schoelkopf. Charge-insensitive qubit design derived from the Cooper pair box. *Phys. Rev. A*, 76:042319, 2007. doi:10.1103/PhysRevA.76.042319.

[77] M. Werninghaus, D. J. Egger, F. Roy, S. Machnes, F. K. Wilhelm, and S. Filipp. Leakage reduction in fast superconducting qubit gates via optimal control. *npj Quantum Inf.*, 7:14, 2021. doi:10.1038/s41534-020-00346-2.

[78] A. Pathak and S. Mandal. Classical and quantum oscillators of quartic anharmonicities: second-order solution. *Phys. Lett. A*, 286:261, 2001. doi:10.1016/S0375-9601(01)00401-7.

[79] G. Yang, A. Fragner, G. Koolstra, L. Ocola, D. A. Czaplewski, R. J. Schoelkopf, and D. I. Schuster. Coupling an ensemble of electrons on superfluid helium to a superconducting circuit. *Phys. Rev. X*, 6:011031, 2016. doi:10.1103/PhysRevX.6.011031.

[80] D. G. Rees, I. Kuroda, C. A. Marrache-Kikuchi, M. Höfer, P. Leiderer, and K. Kono. Point-contact transport properties of strongly correlated electrons on liquid helium. *Phys. Rev. Lett.*, 106:026803, 2011. doi:10.1103/PhysRevLett.106.026803.

[81] H. W. Jiang, M. A. Stan, and A. J. Dahm. Electron transport on thin helium films. *Surf. Sci.*, 196:1, 1988.

[82] K. E. Castoria and S. A. Lyon. Measurement of high density electrons above a helium film on an amorphous metal substrate. *J. Low Temp. Phys.*, 210:441, 2023. doi:10.1007/s10909-022-02904-8.

[83] K. Kajita. Electronic properties of two dimensional electrons formed on liquid helium and solid neon. *Jpn. J. Appl. Phys.*, 26:1943, 1987.

[84] A. Anferov, A. Suleymanzade, A. Oriani, J. Simon, and D. I. Schuster. Millimeter-wave four-wave mixing via kinetic inductance for quantum devices. *Phys. Rev. Appl.*, 13:024056, 2020. doi:10.1103/PhysRevApplied.13.024056.

[85] P. W. Anderson. A mathematical model for the narrowing of spectral lines by exchange or motion. *J. Phys. Soc. Jpn.*, 9:316, 1954. doi:10.1143/JPSJ.9.316.

[86] R. Kubo. Note on the stochastic theory of resonance absorption. *J. Phys. Soc. Jpn.*, 9:935, 1954. doi:10.1143/JPSJ.9.935.

[87] J. B. Johnson. Thermal agitation of electricity in conductors. *Phys. Rev.*, 32:97, 1928. doi:10.1103/PhysRev.32.97.

[88] H. Nyquist. Thermal agitation of electric charge in conductors. *Phys. Rev.*, 32:110, 1928. doi:10.1103/PhysRev.32.110.

[89] R. J. Schoelkopf, A. A. Clerk, S. M. Girvin, K. W. Lehnert, and M. H. Devoret. Qubits as spectrometers of quantum noise. In Yu. V. Nazarov, editor, *Quantum Noise in Mesoscopic Physics*, page 175. Kluwer, Dordrecht, 2003.

[90] J. Yoneda, K. Takeda, T. Otsuka, T. Nakajima, M. R. Delbecq, G. Allison, T. Honda, T. Kodera, S. Oda, Y. Hoshi, N. Usami, K. M. Itoh, and S. Tarucha. A quantum-dot spin qubit with coherence limited by charge noise and fidelity higher than 99.9%. *Nat. Nanotechnol.*, 13:102, 2018. doi:10.1038/s41565-017-0014-x.

[91] A. A. Clerk, M. H. Devoret, S. M. Girvin, F. Marquardt, and R. J. Schoelkopf. Introduction to quantum noise, measurement, and amplification. *Rev. Mod. Phys.*, 82: 1155, 2010. doi:10.1103/RevModPhys.82.1155.

[92] F. Pobell. *Matter and Methods at Low Temperatures*. Springer, Berlin, 3rd edition, 2007.

[93] P. Kapitza. Viscosity of liquid helium below the λ-point. *Nature*, 141:74, 1938. doi:10.1038/141074a0.

[94] J. F. Allen and A. D. Misener. Flow of liquid helium II. *Nature*, 141:75, 1938. doi:10.1038/141075a0.

[95] B. V. Rollin and F. Simon. On the "film" phenomenon of liquid helium II. *Physica*, 6: 219, 1939. doi:10.1016/S0031-8914(39)80013-1.

[96] E. S. Sabisky and C. H. Anderson. Verification of the Lifshitz theory of the van der Waals potential using liquid-helium films. *Phys. Rev. A*, 7:790, 1973. doi:10.1103/PhysRevA.7.790.

[97] G. L. Pollack. Kapitza resistance. *Rev. Mod. Phys.*, 41:48, 1969. doi:10.1103/RevModPhys.41.48.

[98] G. Koolstra. *Trapping a Single Electron on Superfluid Helium Using a Superconducting Resonator*. PhD thesis, The University of Chicago, Chicago, Illinois, 2019.

[99] B. Dizdar, Y. Shi, D. I. Schuster, and C. S. Lang. Probing wetting and solidification dynamics of neon thin films with a high-T_c superconducting circuit, 2026. arXiv:2610.24167.

[100] M. A. Castellanos-Beltran, K. D. Irwin, G. C. Hilton, L. R. Vale, and K. W. Lehnert. Amplification and squeezing of quantum noise with a tunable Josephson metamaterial. *Nat. Phys.*, 4:929, 2008. doi:10.1038/nphys1090.

[101] C. Macklin, K. O'Brien, D. Hover, M. E. Schwartz, V. Bolkhovsky, X. Zhang, W. D. Oliver, and I. Siddiqi. A near–quantum-limited Josephson traveling-wave parametric amplifier. *Science*, 350:307, 2015. doi:10.1126/science.aaa8525.

[102] H. T. Friis. Noise figures of radio receivers. *Proc. IRE*, 32:419, 1944. doi:10.1109/JRPROC.1944.232049.

[103] X. Mi, J. V. Cady, D. M. Zajac, P. W. Deelman, and J. R. Petta. Strong coupling of a single electron in silicon to a microwave photon. *Science*, 355:156, 2017. doi:10.1126/science.aal2469.

[104] D. M. Pozar. *Microwave Engineering*. Wiley, Hoboken, 4th edition, 2012.

[105] A. Shearrow, G. Koolstra, S. J. Whiteley, N. Earnest, P. S. Barry, F. J. Heremans, D. D. Awschalom, E. Shirokoff, and D. I. Schuster. Atomic layer deposition of titanium nitride for quantum circuits. *Appl. Phys. Lett.*, 113:212601, 2018. doi:10.1063/1.5053461.

[106] M. Sandberg, M. R. Vissers, J. S. Kline, M. Weides, J. Gao, D. S. Wisbey, and D. P. Pappas. Etch induced microwave losses in titanium nitride superconducting resonators. *Appl. Phys. Lett.*, 100:262605, 2012. doi:10.1063/1.4729623.

[107] N. Mahuli, J. Minguzzi, J. Gao, R. Resnick, S. Diez, C. Raj, G. Marcaud, M. Hunt, L. Swenson, J. Rose, O. Painter, I. Jarrige, et al. Improving the lifetime of aluminum-based superconducting qubits through atomic layer etching and deposition, 2025. arXiv:2506.17474.

[108] A. T. Asfaw, E. I. Kleinbaum, M. D. Henry, E. A. Shaner, and S. A. Lyon. Transport measurements of surface electrons in 200 nm deep helium-filled microchannels above amorphous metallic electrodes. *J. Low Temp. Phys.*, 195:300, 2019. doi:10.1007/s10909-018-02139-6.

[109] N. R. Beysengulov, Ø. S. Schøyen, S. D. Bilek, J. B. Flaten, O. Leinonen, M. Hjorth-Jensen, J. Pollanen, H. E. Kristiansen, Z. J. Stewart, J. D. Weidman, and A. K. Wilson. Coulomb interaction-driven entanglement of electrons on helium. *PRX Quantum*, 5: 030324, 2024. doi:10.1103/PRXQuantum.5.030324.

[110] G. Koolstra, E. O. Glen, N. R. Beysengulov, H. Byeon, K. E. Castoria, M. Sammon, B. Dizdar, C. S. Wang, D. I. Schuster, S. A. Lyon, J. Pollanen, and D. G. Rees. High-impedance resonators for strong coupling to an electron on helium. *Phys. Rev. Appl.*, 23:024001, 2025. doi:10.1103/PhysRevApplied.23.024001.

[111] R. Barends, H. L. Hortensius, T. Zijlstra, J. J. A. Baselmans, S. J. C. Yates, J. R. Gao, and T. M. Klapwijk. Contribution of dielectrics to frequency and noise of NbTiN superconducting resonators. *Appl. Phys. Lett.*, 92:223502, 2008. doi:10.1063/1.2937837.

[112] S. Kim, H. Terai, T. Yamashita, W. Qiu, T. Fuse, F. Yoshihara, S. Ashhab, K. Inomata, and K. Semba. Enhanced coherence of all-nitride superconducting qubits epitaxially grown on silicon substrate. *Commun. Mater.*, 2:98, 2021. doi:10.1038/s43246-021-00204-4.

[113] M. Xu, X. Han, W. Fu, C.-L. Zou, and H. X. Tang. Frequency-tunable high-Q superconducting resonators via wireless control of nonlinear kinetic inductance. *Appl. Phys. Lett.*, 114:192601, 2019. doi:10.1063/1.5098466.

[114] L. Grünhaupt, N. Maleeva, S. T. Skacel, M. Calvo, F. Levy-Bertrand, A. V. Ustinov, H. Rotzinger, A. Monfardini, G. Catelani, and I. M. Pop. Loss mechanisms and quasiparticle dynamics in superconducting microwave resonators made of thin-film granular aluminum. *Phys. Rev. Lett.*, 121:117001, 2018. doi:10.1103/PhysRevLett.121.117001.

[115] J. G. Kroll, F. Borsoi, K. L. van der Enden, W. Uilhoorn, D. de Jong, M. Quintero-Pérez, D. J. van Woerkom, A. Bruno, S. R. Plissard, D. Car, E. P. A. M. Bakkers, M. C. Cassidy, and L. P. Kouwenhoven. Magnetic-field-resilient superconducting coplanar-waveguide resonators for hybrid circuit quantum electrodynamics experiments. *Phys. Rev. Appl.*, 11:064053, 2019. doi:10.1103/PhysRevApplied.11.064053.

[116] B. Sarabi, A. N. Ramanayaka, A. L. Burin, F. C. Wellstood, and K. D. Osborn. Projected dipole moments of individual two-level defects extracted using circuit quantum electrodynamics. *Phys. Rev. Lett.*, 116:167002, 2016. doi:10.1103/PhysRevLett.116.167002.

[117] C. Müller, J. H. Cole, and J. Lisenfeld. Towards understanding two-level-systems in amorphous solids: Insights from quantum circuits. *Rep. Prog. Phys.*, 82:124501, 2019. doi:10.1088/1361-6633/ab3a7e.

[118] M. Kong, B. Partoens, and F. M. Peeters. Transition between ground state and metastable states in classical two-dimensional atoms. *Phys. Rev. E*, 65:046602, 2002. doi:10.1103/PhysRevE.65.046602.

[119] D. I. Schuster, A. Wallraff, A. Blais, L. Frunzio, R.-S. Huang, J. Majer, S. M. Girvin, and R. J. Schoelkopf. ac Stark shift and dephasing of a superconducting qubit strongly coupled to a cavity field. *Phys. Rev. Lett.*, 94:123602, 2005. doi:10.1103/PhysRevLett.94.123602.

[120] G. Zhu, D. G. Ferguson, V. E. Manucharyan, and J. Koch. Circuit QED with fluxonium qubits: Theory of the dispersive regime. *Phys. Rev. B*, 87:024510, 2013. doi:10.1103/PhysRevB.87.024510.

[121] D.-Y. Kim, H. Kwon, D. S. Han, K. Kim, H. K. Kim, C. Lee, G. Kim, J.-Y. M. Lee, D. Kim, E.-A. Kim, and J. Shin. Impact of fabrication history induced disorder on Josephson junction reproducibility and qubit performance. *Sci. Rep.*, 16:18216, 2026. doi:10.1038/s41598-026-46352-w.

[122] V. E. Manucharyan, J. Koch, L. I. Glazman, and M. H. Devoret. Fluxonium: Single Cooper-pair circuit free of charge offsets. *Science*, 326:113, 2009. doi:10.1126/science.1175552.

[123] L. S. Bishop, E. Ginossar, and S. M. Girvin. Response of the strongly driven Jaynes-Cummings oscillator. *Phys. Rev. Lett.*, 105:100505, 2010. doi:10.1103/PhysRevLett.105.100505.

[124] M. Boissonneault, J. M. Gambetta, and A. Blais. Improved superconducting qubit readout by qubit-induced nonlinearities. *Phys. Rev. Lett.*, 105:100504, 2010. doi:10.1103/PhysRevLett.105.100504.

[125] G. Kirchmair, B. Vlastakis, Z. Leghtas, S. E. Nigg, H. Paik, E. Ginossar, M. Mirrahimi, L. Frunzio, S. M. Girvin, and R. J. Schoelkopf. Observation of quantum state collapse and revival due to the single-photon Kerr effect. *Nature*, 495:205, 2013. doi:10.1038/nature11902.

[126] S. E. Nigg, H. Paik, B. Vlastakis, G. Kirchmair, S. Shankar, L. Frunzio, M. H. Devoret, R. J. Schoelkopf, and S. M. Girvin. Black-box superconducting circuit quantization. *Phys. Rev. Lett.*, 108:240502, 2012. doi:10.1103/PhysRevLett.108.240502.

[127] N. E. Frattini, V. V. Sivak, A. Lingenfelter, S. Shankar, and M. H. Devoret. Optimizing the nonlinearity and dissipation of a SNAIL parametric amplifier for dynamic range. *Phys. Rev. Appl.*, 10:054020, 2018. doi:10.1103/PhysRevApplied.10.054020.

[128] P. M. Polunin, Y. Yang, M. I. Dykman, T. W. Kenny, and S. W. Shaw. Characterization of MEMS resonator nonlinearities using the ringdown response. *J. Microelectromech. Syst.*, 25:297, 2016. doi:10.1109/JMEMS.2016.2529296.

[129] M. I. Dykman, editor. *Fluctuating Nonlinear Oscillators: From Nanomechanics to Quantum Superconducting Circuits*. Oxford University Press, Oxford, 2012.

[130] P. Zhao, P. Xu, D. Lan, J. Chu, X. Tan, H. Yu, and Y. Yu. High-contrast ZZ interaction using superconducting qubits with opposite-sign anharmonicity. *Phys. Rev. Lett.*, 125: 200503, 2020. doi:10.1103/PhysRevLett.125.200503.

[131] E. Y. Andrei, editor. *Two-Dimensional Electron Systems on Helium and Other Cryogenic Substrates*. Kluwer Academic, Dordrecht, 1997.

[132] A. B. Fowler, F. F. Fang, W. E. Howard, and P. J. Stiles. Magneto-oscillatory conductance in silicon surfaces. *Phys. Rev. Lett.*, 16:901, 1966. doi:10.1103/PhysRevLett.16.901.

[133] T. Smoleński, P. E. Dolgirev, C. Kuhlenkamp, A. Popert, Y. Shimazaki, P. Back, X. Lu, M. Kroner, K. Watanabe, T. Taniguchi, I. Esterlis, E. Demler, and A. Imamoğlu. Signatures of Wigner crystal of electrons in a monolayer semiconductor. *Nature*, 595: 53, 2021. doi:10.1038/s41586-021-03590-4.

[134] Y.-C. Tsui, M. He, Y. Hu, E. Lake, T. Wang, K. Watanabe, T. Taniguchi, M. P. Zaletel, and A. Yazdani. Direct observation of a magnetic-field-induced Wigner crystal. *Nature*, 628:287, 2024. doi:10.1038/s41586-024-07212-7.

[135] K. Kajita. A new two-dimensional electron system on the surface of solid neon. *Surf. Sci.*, 142:86, 1984.

[136] H. Kamerlingh Onnes. Methods and apparatus used in the cryogenic laboratory. XVI. The neon-cycle. *Proc. K. Ned. Akad. Wet.*, 18:507, 1915.

[137] J. Krim, J. G. Dash, and J. Suzanne. Triple-point wetting of light molecular gases on Au(111) surfaces. *Phys. Rev. Lett.*, 52:640, 1984. doi:10.1103/PhysRevLett.52.640.

[138] C. C. Tsuei and J. R. Kirtley. Pairing symmetry in cuprate superconductors. *Rev. Mod. Phys.*, 72:969, 2000. doi:10.1103/RevModPhys.72.969.

[139] M. K. Wu, J. R. Ashburn, C. J. Torng, P. H. Hor, R. L. Meng, L. Gao, Z. J. Huang, Y. Q. Wang, and C. W. Chu. Superconductivity at 93 K in a new mixed-phase Y-Ba-Cu-O compound system at ambient pressure. *Phys. Rev. Lett.*, 58:908, 1987. doi:10.1103/PhysRevLett.58.908.

[140] A. Ghirri, C. Bonizzoni, D. Gerace, S. Sanna, A. Cassinese, and M. Affronte. $YBa_2Cu_3O_7$ microwave resonators for strong collective coupling with spin ensembles. *Appl. Phys. Lett.*, 106:184101, 2015. doi:10.1063/1.4920930.

[141] M. Arzeo, F. Lombardi, and T. Bauch. Microwave losses in YBCO coplanar waveguide resonators at low power and millikelvin range. *IEEE Trans. Appl. Supercond.*, 25: 6936352, 2015. doi:10.1109/TASC.2014.2364777.

[142] S. Duthaluru, K. Zheng, E. A. Henriksen, and K. W. Murch. Real-time monitoring of growth of neon film for electron-on-neon qubits. *Phys. Rev. Appl.*, 25:044065, 2026. doi:10.1103/wjfs-cgwc.

[143] K. Matkovic, P. Russell, A. Palmer, E. Helgemo, L. Delventhal, K. Zuo, K. Surse, R. Rahman, and M. C. Cassidy. Characterizing neon thin film growth with an NbTiN superconducting resonator array, 2025. arXiv:2510.21029.

[144] K. Zheng, X. Song, and K. W. Murch. Surface morphology assisted trapping of strongly coupled electron-on-neon charge states, 2025. arXiv:2503.01847.

[145] C. Wang, C. Axline, Y. Y. Gao, T. Brecht, Y. Chu, L. Frunzio, M. H. Devoret, and R. J. Schoelkopf. Surface participation and dielectric loss in superconducting qubits. *Appl. Phys. Lett.*, 107:162601, 2015. doi:10.1063/1.4934486.

[146] J. M. Gambetta, C. E. Murray, Y.-K.-K. Fung, D. T. McClure, O. Dial, W. Shanks, J. W. Sleight, and M. Steffen. Investigating surface loss effects in superconducting transmon qubits. *IEEE Trans. Appl. Supercond.*, 27:1700205, 2017. doi:10.1109/TASC.2016.2629670.

[147] Z. K. Minev, Z. Leghtas, S. O. Mundhada, L. Christakis, I. M. Pop, and M. H. Devoret. Energy-participation quantization of Josephson circuits. *npj Quantum Inf.*, 7:131, 2021. doi:10.1038/s41534-021-00461-8.

[148] F. Valenti, A. N. Kanagin, A. Angerer, L. Buimaga-Iarinca, C. Morari, J. Schmiedmayer, and I. M. Pop. Hydrogen crystals reduce dissipation in superconducting resonators. *Phys. Rev. B*, 109:054503, 2024. doi:10.1103/PhysRevB.109.054503.

[149] X. Mi, M. Benito, S. Putz, D. M. Zajac, J. M. Taylor, G. Burkard, and J. R. Petta. A coherent spin–photon interface in silicon. *Nature*, 555:599, 2018. doi:10.1038/nature25769.

[150] N. Samkharadze, G. Zheng, N. Kalhor, D. Brousse, A. Sammak, U. C. Mendes, A. Blais, G. Scappucci, and L. M. K. Vandersypen. Strong spin-photon coupling in silicon. *Science*, 359:1123, 2018. doi:10.1126/science.aar4054.

[151] M. Kristen, J. N. Voss, M. Wildermuth, A. Bilmes, J. Lisenfeld, H. Rotzinger, and A. V. Ustinov. Giant two-level systems in a granular superconductor. *Phys. Rev. Lett.*, 132:217002, 2024. doi:10.1103/PhysRevLett.132.217002.

[152] W. Guo, D. Konstantinov, and D. Jin. Quantum electronics on quantum liquids and solids, 2024. arXiv:2406.15870.

[153] S. Sheludiakov, J. Ahokas, J. Järvinen, L. Lehtonen, S. Vasiliev, Yu. A. Dmitriev, D. M. Lee, and V. V. Khmelenko. Electrons trapped in solid neon–hydrogen mixtures below 1 K. *J. Low Temp. Phys.*, 195:365, 2019. doi:10.1007/s10909-018-02135-w.

[154] Y. Tokura, W. G. van der Wiel, T. Obata, and S. Tarucha. Coherent single electron spin control in a slanting Zeeman field. *Phys. Rev. Lett.*, 96:047202, 2006. doi:10.1103/PhysRevLett.96.047202.

[155] M. Pioro-Ladrière, T. Obata, Y. Tokura, Y.-S. Shin, T. Kubo, K. Yoshida, T. Taniyama, and S. Tarucha. Electrically driven single-electron spin resonance in a slanting Zeeman field. *Nat. Phys.*, 4:776, 2008. doi:10.1038/nphys1053.

[156] C. Ospelkaus, C. E. Langer, J. M. Amini, K. R. Brown, D. Leibfried, and D. J. Wineland. Trapped-ion quantum logic gates based on oscillating magnetic fields. *Phys. Rev. Lett.*, 101:090502, 2008. doi:10.1103/PhysRevLett.101.090502.

[157] X. Hu, Y.-x. Liu, and F. Nori. Strong coupling of a spin qubit to a superconducting stripline cavity. *Phys. Rev. B*, 86:035314, 2012. doi:10.1103/PhysRevB.86.035314.

[158] J. Yoneda, T. Otsuka, T. Takakura, M. Pioro-Ladrière, R. Brunner, H. Lu, T. Nakajima, T. Obata, A. Noiri, C. J. Palmstrøm, A. C. Gossard, and S. Tarucha. Robust micromagnet design for fast electrical manipulations of single spins in quantum dots. *Appl. Phys. Express*, 8:084401, 2015. doi:10.7567/APEX.8.084401.

[159] J. C. Lemyre. Cobalt micro-magnet integration on silicon MOS quantum dots. Sandia National Laboratories, SAND2017-2486C, 2017.

[160] P. Haikka, Y. Kubo, A. Bienfait, P. Bertet, and K. Mølmer. Proposal for detecting a single electron spin in a microwave resonator. *Phys. Rev. A*, 95:022306, 2017. doi:10.1103/PhysRevA.95.022306.

[161] M. Zhang and L. F. Wei. Spin-orbit couplings between distant electrons trapped individually on liquid helium. *Phys. Rev. B*, 86:205408, 2012. doi:10.1103/PhysRevB.86.205408.

[162] A. Sørensen and K. Mølmer. Quantum computation with ions in thermal motion. *Phys. Rev. Lett.*, 82:1971, 1999. doi:10.1103/PhysRevLett.82.1971.

[163] A. Sørensen and K. Mølmer. Entanglement and quantum computation with ions in thermal motion. *Phys. Rev. A*, 62:022311, 2000. doi:10.1103/PhysRevA.62.022311.